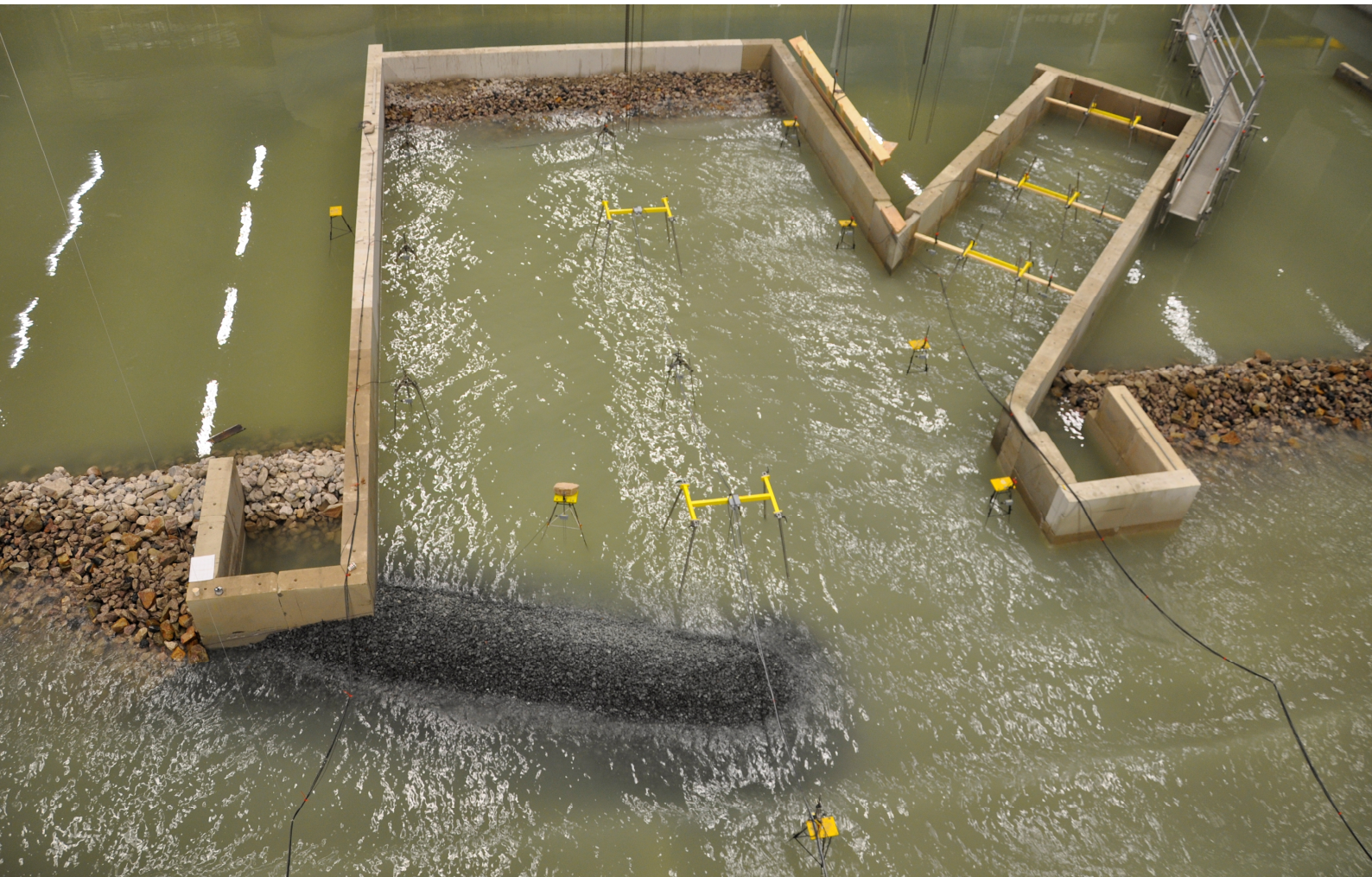


Numerical modelling of wave penetration in ports

MSc Thesis



F.A.J.M. van Mierlo

November 2014

Numerical modelling of wave penetration in ports

By

F.A.J.M. van Mierlo

Master of Science thesis

Delft, November 2014

Graduation Committee:

Prof. ir. T. Vellinga
Ir. P.P.D. van der Ven
Dr. ir. M. Zijlema
Ir. B. Wijdeven
Dr. J. Yuan

Delft University of Technology
Deltares
Delft University of Technology
Delft University of Technology
National University of Singapore

Preface

This thesis was written in partial fulfilment of the double degree Master of Science programme at Delft University of Technology and National University of Singapore. The thesis work has been carried out at Deltares.

I would like to acknowledge all the members of my graduation committee for their supervision and constructive criticism. I am in particular grateful to Ir. Pepijn van der Ven, who has guided me the most extensively, for always making time for me and for the much appreciated feedback. Special thanks also to Dr. Marcel Zijlema for his valuable advice and help with setting up SWASH simulations. The support from Singapore is also much appreciated.

Furthermore, I am grateful to Ir. Arne van der Hout and Dr. Ir. Martijn de Jong from Deltares for their suggestions and the interesting and inspiring discussions. Thanks also to my fellow students at Deltares for the many nice lunches and coffee breaks. Last but not least, I would like to thank my parents for their unconditional support.

Frank van Mierlo

Delft, November 2014

Summary

Wave climates in ports can determine the efficiency of port operations to a large extent, so good predictions of them are important. This thesis therefore focusses on the modelling of wave penetration in ports, using several numerical models as well as a physical model. The goal is to compare numerical wave models for the use of wave penetration in ports and to determine application boundaries.

An overview of existing classes of numerical wave models and their potential for modelling wave penetration in ports is made first. This leads to the conclusion that mild-slope models, Boussinesq-type models and non-hydrostatic models are probably the most appropriate. From each of these model classes an operational model is chosen (i.e. PHAROS, TRITON and SWASH) for further study.

It is demonstrated that these models are all capable of accurately reproducing analytical solutions for linear shoaling and diffraction. These two wave processes are, together with reflection, identified as crucial for wave propagation in harbours.

Differences between these models are pointed out as well. Most notable are the differences in underlying equations, schematisations of boundaries and computational efficiency

To be able to study the performance of operational numerical models for wave penetration in ports, in scenarios that are more realistic than analytical benchmark test cases, measurements from a physical model are used. The physical model represents a typical seaport, is schematised to facilitate numerical modelling, uses three layouts with increasing complexity, and is subjected to a large variety of wave conditions. The physical modelling is carried out at Deltares in the framework of one of their projects and the produced dataset will become freely available.

A selection of the 57 scale model tests are analysed in detail and numerically simulated using PHAROS, TRITON and SWASH. A comparison between the simulation results and the corresponding physical model measurements shows that TRITON and SWASH are capable of modelling the penetration of primary waves in ports. PHAROS simulations are less accurate and appear to overestimate wave heights in areas sheltered from direct wave attack, which is ascribed to its specific use of reflection boundaries. Wave conditions with very large wave height over depth ratios (up to 0.5), where wave breaking is significant, can still be simulated accurately with both PHAROS and SWASH. TRITON could not be used to simulate these wave conditions due to numerical instabilities.

The total amount of low frequency wave energy modelled by TRITON and SWASH corresponds well with measurements from the physical model (for PHAROS this comparison is not made). Specific harbour oscillations are however only reproduced qualitatively by all three numerical models.

Contents

Preface	ii
Summary	iii
1 Introduction	1
1.1 Framework	1
1.2 Motivation of study.....	1
1.3 Goal	1
1.4 Research questions	1
1.5 Approach.....	2
2 Background on wave modelling in ports	4
2.1 Wave processes affecting wave propagation in ports.....	4
2.2 Overview of numerical models for wave propagation in ports	8
2.3 Application boundaries for operational numerical wave models in ports	16
2.4 Conclusions	17
3 Selection of numerical wave models for further study	18
3.1 Introduction	18
3.2 PHAROS	18
3.3 TRITON	26
3.4 SWASH	30
3.5 Conclusions	34
4 Comparison and analytical benchmark tests of selected models.....	35
4.1 Introduction	35
4.2 Model boundaries.....	35
4.3 Shoaling.....	37
4.4 Diffraction	42
4.5 Computational efficiency	48
4.6 Conclusions	49
5 The physical model	50
5.1 Introduction	50
5.2 Aims of the physical modelling	50
5.3 Model design.....	51
5.4 Test wave conditions	57
5.5 Observations during the execution of the physical modelling	60
6 Selection of tests from physical modelling	61

6.1	Introduction	61
6.2	Most suitable wave conditions	61
6.3	Most suitable scale model layouts.....	61
6.4	Selected experiments.....	61
7	Analysis of physical model results for selected tests.....	63
7.1	Primary waves.....	63
7.2	Low frequency waves and harbour oscillations.....	68
8	Comparisons between measurements and numerical simulation	72
8.1	Primary waves.....	72
8.2	Low frequency waves and harbour oscillations.....	81
9	Conclusions and recommendations.....	87
9.1	Conclusions	87
9.2	Recommendations	88
10	References	89
Appendix A	Numerical model set-ups.....	94
Appendix B	Generation of surface elevation time series from wave board motions.....	99
Appendix C	Determination of reflection coefficients	101
Appendix D	List of all wave conditions.....	103
Appendix E	Examples of TRITON input files.....	108
Appendix F	Example of SWASH command file.....	110

1 Introduction

1.1 Framework

This thesis is related to the project “Benchmark tests for Harbour models”, which was initiated by Deltares (Deltares 2014). Table 1.1 lists the parties involved in this project and the numerical models (which will be described later on) they develop.

Table 1.1 Parties and models involved in the project “Benchmark test for Harbour models”

Party	Model
Delft University of Technology	SWASH
Twente University	AB, VBM
Institute for Hydraulic Engineering	XBEACH
Deltares	TRITON, PHAROS, XBEACH

One of the goals of this project is to produce a benchmark test dataset that can be used to validate numerical models for wave penetration in harbours. The dataset is obtained through physical modelling and will become freely available. This thesis contributes to the creation of the dataset, and uses it to determine application boundaries of a selection of the models listed above.

1.2 Motivation of study

Efficient loading and unloading of vessels in ports requires minimum wave agitation at the berths. If wave conditions get really severe it may not even be possible for vessels to safely stay at a berth.

Waves in ports are either generated locally or originate from outside the port and propagate into the port areas. Locally generated waves usually cause less hindrance to port operations than waves that originate from oceans or seas. Especially low frequency waves, which may cause harbour oscillations, are notorious. In order to design a port layout that minimises downtime at berths it is thus important to understand and be able to predict the propagation of waves in ports.

Several classes of numerical wave models are being developed. Each class of wave models has its own strengths, weaknesses and area of application. It is not always sufficiently known which model types are the most suitable for modelling primary waves, low frequency waves and harbour oscillations in ports and under what conditions they can be applied.

1.3 Goal

The goal of this thesis is to compare numerical models for the use of wave propagation in ports. This includes the determination of application limits of the numerical models using scale model tests.

1.4 Research questions

Main question

What are the application boundaries of operational numerical wave models for wave penetration in harbours?

Sub questions

Which numerical models will be studied?

- Which wave processes are relevant for wave penetration in harbours?
- What classes of numerical wave models exist?

What are the differences between these models and how do they influence the results of computations?

- What are the theoretical differences (e.g., in model equations)?
- Are there any differences that follow from the numerical implementations?
- How do the models compare when it comes to computational efficiency?

How to assess model performance and application limits with the aid of physical model tests?

- Where to focus the physical model tests on?
- What port layout and wave conditions will be considered?
- How to compare the results from the physical model tests with those from numerical simulations?
- How to determine application boundaries from these comparisons?

1.5 Approach

The main steps of which this thesis consists are summarised in Figure 1.1. Each step is elaborated in the next sections.

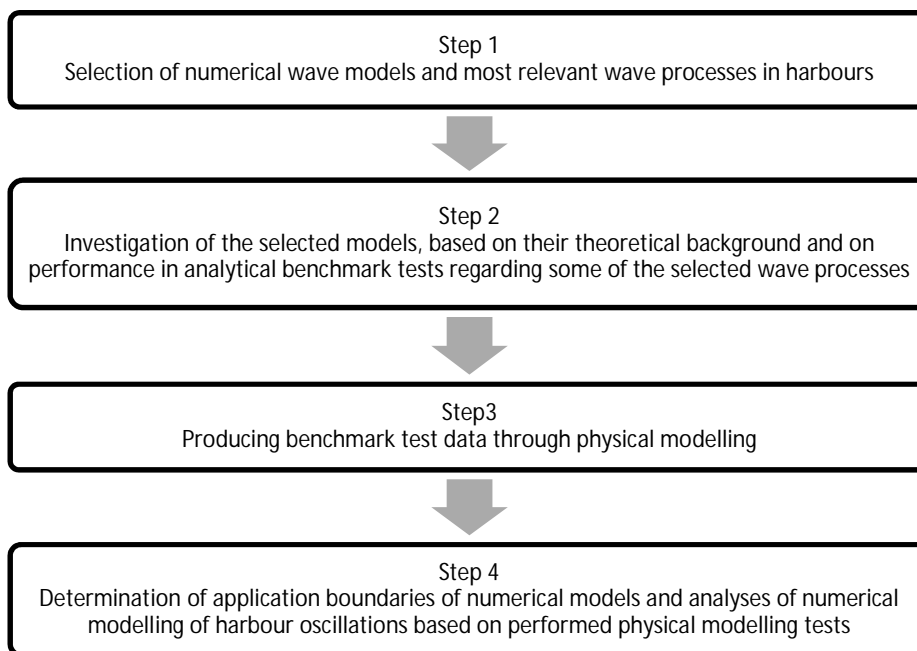


Figure 1.1 – The main steps in this thesis

1.5.1 Step 1: Literature study of wave processes and wave models in harbours

Numerous wave processes affect wave propagation in ports. Some of them can be neglected in certain situations. The first step will be a literature study to investigate which wave process needs to be simulated accurately in which situation.

Next, an overview is made of existing models for wave penetration in harbours. Based on this, three models, PHAROS, TRITON, and SWASH, are selected to study in more detail.

1.5.2 Step 2: Comparison of PHAROS, TRITON and SWASH

The properties of and the differences between PHAROS, TRITON and SWASH are elaborated in this second step. First the governing equations, boundary conditions, numerical techniques, etc. of each model are summarized.

An important difference between the models is how boundary conditions for partial reflection are handled, some considerations will therefore be devoted to this subject. Performance for linear shoaling and diffraction, and the effects of certain model settings hereupon, are investigated by simulating benchmark test cases for which analytical solutions can be found. Benchmark test cases based on analytical solutions are used because they require relatively little effort and can still give useful insight. Lastly, the computational efficiency of the considered models is compared.

1.5.3 Step 3: Scale model tests

The third step consists of defining, performing and analysing scale model tests. The scale model tests are designed to (amongst others):

- Facilitate an assessment of the overall model performance and find application boundaries
- To study harbour oscillations

This choice is driven by the fact that the related processes are very relevant for port operations and cannot be satisfactorily studied from analytical test cases alone, since analytical test cases only concern much idealised situations.

The scale model has three different layouts to represent a typical harbour in three steps of complexity. The layout is schematised to facilitate the numerical modelling later on. The scale model tests use monochromatic, bichromatic and JONSWAP wave conditions. Wave heights, wave periods, and water depths are chosen in such a way that a large variety of wave regimes are tested.

After the experiments are finished, tests are selected to analyse in further detail and to simulate with the numerical models later on. Most of the selected tests were carried out for the most complex layout. These tests are considered to be the most suitable for the purpose of investigating overall model performance. Two tests for other model layouts are also included in the selection, for studying harbour oscillations.

1.5.4 Step 4: Comparison of numerical simulations with scale model tests

The last main step starts with numerically simulating a selected number of tests that were carried out in the scale model. The simulation results are then compared with the measurements from the scale model.

The comparison focuses on:

- Wave heights at the measurement locations
- Wave period at the measurement locations
- Low frequency wave spectra at the measurement locations

The final step is to draw a conclusion on the performance and application boundaries of the different models.

2 Background on wave modelling in ports

2.1 Wave processes affecting wave propagation in ports

This chapter gives a brief explanation of how several wave processes affect the propagation of waves into harbours. It is assumed that the reader is already familiar with these wave processes. For a detailed description of these wave processes the reader is referred to (Holthuijsen 2007).

2.1.1 Shoaling

Shoaling occurs when the wave group velocity decreases in the direction of wave propagation. This happens for example when the water depth decreases. In a stationary situation the energy flux, which is the product of the wave group velocity and the wave energy per horizontal surface area, must be constant along the wave rays. This explains why the wave energy per horizontal surface area (and thus the wave height) increases when the group velocity decreases.

The shoaling of low amplitude waves can be predicted based on linear wave theory, because amplitude dispersion is negligible. For waves with larger amplitudes (relative to the water depth) this is no longer the case. When these waves shoal nonlinear effects result in the generation of more high order harmonic wave components and more complex wave forms.

Shoaling is very relevant for wave propagation in harbours because the water depth inside a harbour is usually a lot less than the water depth offshore. Waves also shoal within a harbour area when the depth is not uniform.

2.1.2 Refraction

Refraction is also caused by varying water depths. Waves bend towards areas with smaller water depths due to the difference in phase velocity along a wave crest.

Waves propagating towards a harbour will experience refraction, unless they enter the harbour exactly perpendicular to the (parallel) bed level contours. For harbours with a non-uniform depth refraction is also of importance within the harbour area.

2.1.3 Diffraction

If the amplitude of waves abruptly decreases along the wave crest, waves will propagate into the region with lower wave amplitudes. This diffraction enables waves to bend around sharp corners. For long waves the diffraction effect is stronger than for short waves. Diffraction therefore results in a lower mean wave period directly behind a breakwater.

Ports often have lots of sharp corners (like the tip of a breakwater or the entrance of a basin) where waves diffract. This phenomenon has a large contribution to the amount of wave energy that propagates into basins or areas shielded by breakwaters.

2.1.4 Reflection

When waves collide with a structure or a beach, part of the incoming wave energy will be reflected. The amount of reflected wave energy is usually quantified by means of a reflection coefficient k_r , defined as:

$$k_r = \frac{H_r}{H_i} \quad (1)$$

with k_r reflection coefficient
 H_r reflected wave height
 H_i incoming wave height

The amount of reflected wave energy depends on the characteristics of the incoming wave and the properties of the surface where the interaction takes place. Regarding the incoming waves, the wave height, wave length, and wave direction are particularly important. With regard to the structure, the slope and roughness are most important.

For waves travelling perpendicular towards a smooth structure, the type of interaction or breaking (e.g. surging, collapsing, plunging or spilling) can be shown to depend on the Iribarren number or surf similarity parameter (Battjes 1974). This dimensionless number is given by:

$$\xi_0 = \frac{\tan \alpha}{\sqrt{(2\pi H_{m0}) / (g T_{m-1,0}^2)}} \approx \frac{\tan \alpha}{\sqrt{H_{m0} / L_0}} \quad (2)$$

with ξ_0 surf similarity parameter or Iribarren number
 α slope angle
 H_{m0} wave height
 $T_{m-1,0}$ wave period
 L_0 deep water wave length
 g acceleration due to gravity

The dimensionless parameter can be viewed as the ratio between the steepness of the slope and the steepness of the wave. Values of 3.3 and higher have been associated with surging or collapsing waves. Since it is related to the type of wave breaking, it can be used to predict the amount of energy dissipation, and thus the reflection coefficient, as well. Generally speaking, k_r increases with ξ .

Zanuttigh and Van der Meer (2006) produced a database containing reflection coefficients obtained from a large number of experiments. A variety of coastal structures, all with straight slopes, are included. Figure 2.1 shows the correlation they found between the reflection coefficient and the surf similarity parameter (defined as in equation (2)).

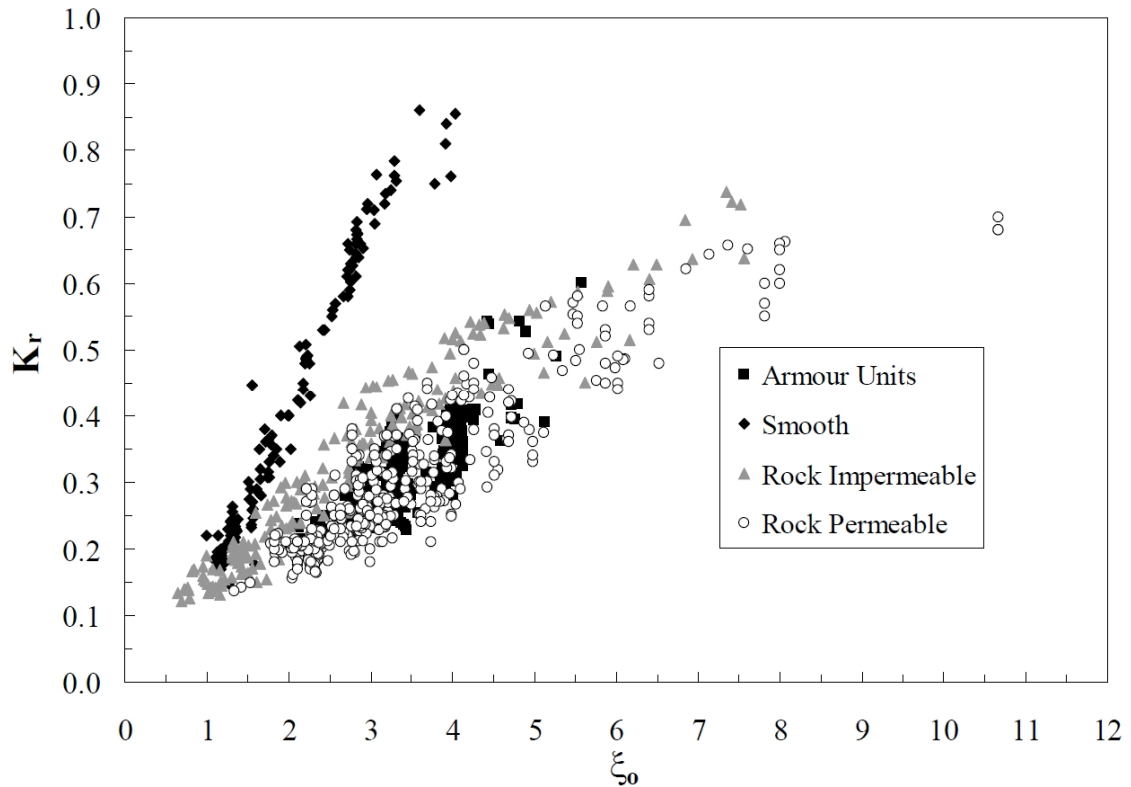


Figure 2.1 - All straight slopes with wave conditions in the order of stability design conditions. Source: (Zanuttigh and Van der Meer 2006)

When waves travel towards a structure under a certain direction, the perceived slope changes. In general, the less perpendicular a wave hits a structure or a beach, the lower the reflection coefficient will be.

Ports typically have lots of vertical (quay) walls that reflect almost all of the incoming wave energy. This can easily result in standing waves, which hinder port operations. To dissipate wave energy that enters a harbour, permeable structures are very effective. To correctly model waves in ports it is essential to properly take reflection into account.

2.1.5 Harbour oscillations

Every harbour possesses certain eigenmodes, determined by its geometry. These eigenmodes can be excited by waves with wave periods corresponding to these eigenmodes. These wave periods are generally in the range of 0.5 to 30 minutes, depending on the dimensions of the basin. The result of this (near) resonance is a standing wave pattern with significantly amplified amplitudes, which can hinder port operations.

The phenomenon of harbour oscillations is similar to that of seiches in closed systems such as lakes. The main difference is that in case of harbour oscillations wave energy radiates out of the harbour, while seiches are principally damped by friction losses. The forcing mechanisms of seiches are of course different as well.

2.1.6 Dispersion

Wave dispersion is the phenomenon that the celerity of waves depends on the wave frequency and/or wave amplitude. It is described by the well-known linear dispersion relationship:

$$\omega^2 = gk \tanh kh \quad (3)$$

Which can be more conveniently formulated for this discussion as:

$$c^2 = \frac{g}{k} \tanh kh \quad (4)$$

with $\omega = \frac{2\pi}{T}$ angular frequency, with T the wave period

$k = \frac{2\pi}{L}$ wave number, with L the wave length

$c = \frac{\omega}{k}$ phase velocity

h water depth

g gravitational acceleration

Frequency dispersion, commonly referred to as wave dispersion, is a linear effect that makes long (i.e. low frequency) waves propagate faster than short (i.e. high frequency) waves. This effect is dominant for waves in deep water, when the water depth is large compared to the wave length and the wave amplitude, and amplitude dispersion is therefore negligible. It is easily seen from the dispersion relationship that if kh (the relative water depth) is large, the depth h disappears from the equation.

Amplitude dispersion is a nonlinear effect that makes high amplitude waves propagate faster than low amplitude waves. This phenomenon occurs for waves in shallow water, when the water depth is small compared to the wave length and relatively small compared to the wave amplitude. The dependence of the vertical structure of the flow (or vertical pressure distribution) on the wave frequency is now negligible, so frequency dispersion does not occur. This is also readily seen from the dispersion relationship. If kh is small, the phase velocity is no longer depending on the wave number k .

Wind generated waves in nearshore regions and harbours can neither be qualified as deep water waves nor as shallow water waves, so they should be considered as waves in intermediate water depths. These waves are therefore subject to both frequency and amplitude dispersion, which affect the group velocity and the transformation of the shape of individual waves.

2.1.7 Nonlinear wave-wave interactions

Quadruplet wave-wave interactions are resonant interactions that transfer energy between four wave components. They are especially important in deep water, where they stabilise the shape of the wave spectrum (Holthuijsen 2007).

Triad wave-wave interactions, (near) resonant interactions between three wave components, occur in nearshore regions. They transfer more energy than quadruplet wave-wave interactions in these shallow areas. Triad wave-wave interactions generate super harmonics in the wave spectrum at frequencies of multiple times the peak frequency, and sub harmonics at very low frequencies (associated with the difference in frequency of the participating wave components).

Nonlinear wave-wave interactions get stronger as waves become more nonlinear, i.e. as wave amplitude and wave steepness increases. The importance of these interactions for waves propagating into ports depends on the wave conditions, bathymetry and port layout.

2.1.8 Low frequency waves

Low frequency waves can be generated by groups of primary, wind generated, short waves. These so called bound low frequency waves travel with the speed of the wave group and have a length that is equal to the length of the wave group. For a bichromatic wave group for instance, the wavenumber of the bound low frequency wave will be equal to the difference in wave number of the two short waves. Bound low frequency waves arise because of a difference in radiation stress under high and low waves in the (for instance bichromatic) wave group.

When the primary waves break the bound long wave is released (becoming a free wave, travelling at its own celerity) and reflects of the coast. The released low frequency waves can be “trapped” near the coast due to refraction. The amount of low frequency wave energy at a certain point along the coast can therefore depend on waves that originated somewhere far away along the coastline.

Low frequency waves can cause oscillations in harbour basins. Basin resonance can occur when the length of the low frequency wave matches with the dimensions of the basin.

2.1.9 Wave breaking

Waves become steeper as they propagate towards the shore (due to shoaling for example) and will eventually break at a certain water depth. The type of wave breaking that occurs can be related to the Iribarren number or surf similarity parameter, see Section 2.1.4. This depth induced wave breaking is the main source of energy dissipation in the surf zone. It is also relevant for harbour areas that contain beaches. Depth-induced wave breaking is a nonlinear process that is relatively difficult to model accurately.

Waves can also break in deeper water if their front becomes too steep, this is called white-capping. White-capping is the main source of energy dissipation for waves in oceanic waters, but can usually be neglected for waves within harbours.

2.2 Overview of numerical models for wave propagation in ports

2.2.1 Introduction

A variety of wave models exist that can be used for modelling wave penetration in harbours. A schematic overview of the main classes of models, their relative performance in modelling wave penetration in ports and their interrelations, is presented in Figure 2.2. Note that within some model classes (especially the Boussinesq-type models) quite a large variation of models exists. All model classes are nonetheless plotted as single points in the graph to make the figure clearer.

The classes of models included in Figure 2.2 are described in the next sections. An extensive elaboration on these classes of models (except for non-hydrostatic and full free-surface Navier-Stokes models) can be found in the work of De Jong en Borsboom (2007) and Dingemans (1994).

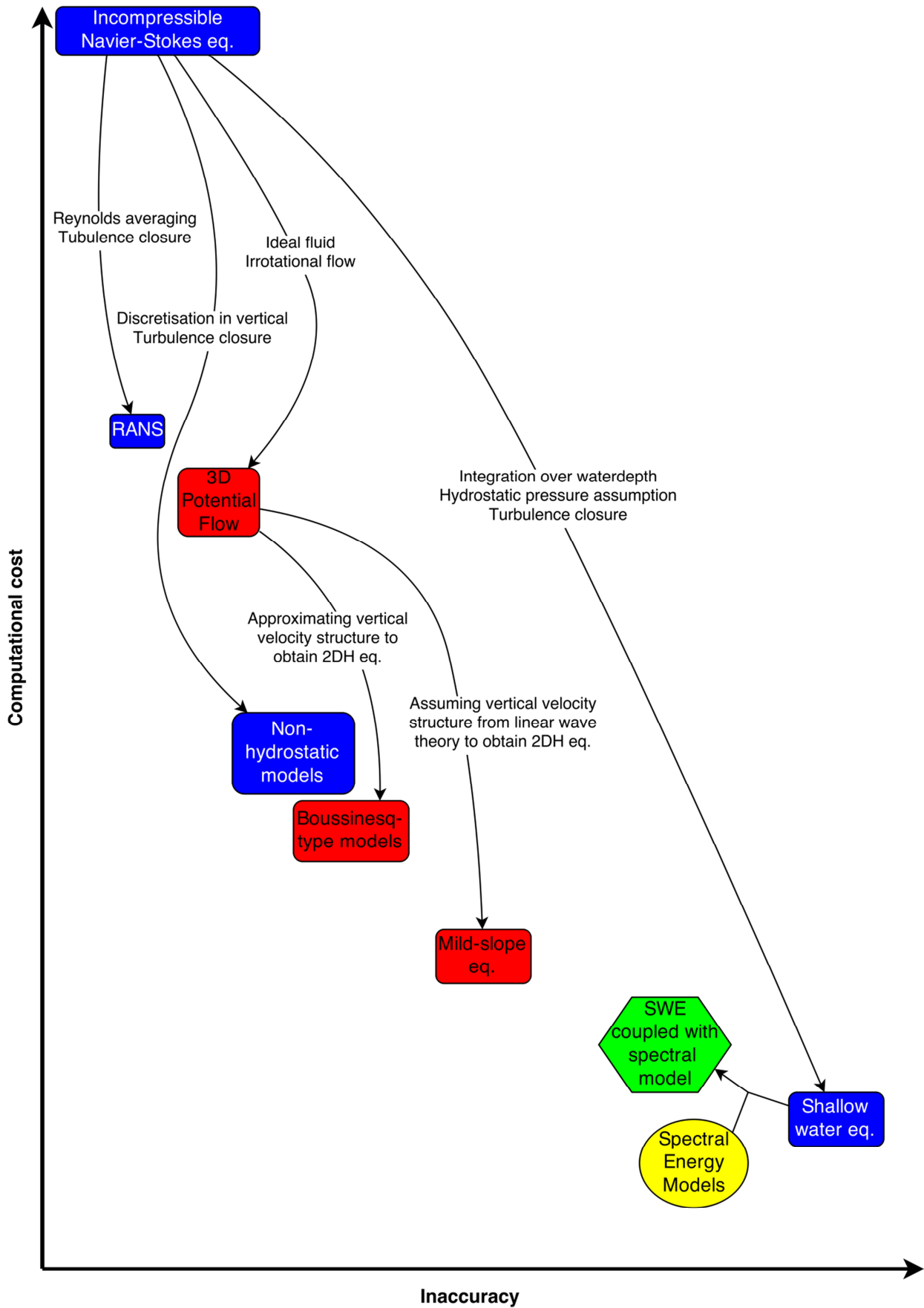


Figure 2.2 - Classes of wave models (red colour indicates models based on potential flow, rectangular shapes indicate phase resolving models, round shape indicates phase averaged models)

2.2.2 Spectral wave models

Spectral wave models are based on wave energy conservation. They solve an energy balance equations that describes the transport of wave energy (in both physical space and within the energy density spectrum) and includes multiple source and sink terms. This equation can account for ambient currents by formulating it in terms of action density (which is equal to the energy density divided by the relative frequency). It then reads:

$$\frac{\partial N}{\partial t} + \frac{\partial c_{g,x} N}{\partial x} + \frac{\partial c_{g,y} N}{\partial y} + \frac{\partial c_{g,\theta} N}{\partial \theta} + \frac{\partial c_{g,\sigma} N}{\partial \sigma} = \frac{S}{\sigma} \quad (5)$$

With $N = E / \sigma$ wave action density
 E wave energy density
 σ relative wave frequency
 x, y horizontal coordinates
 t time
 c_g wave energy propagation velocity
 θ wave direction
 S energy sources and sinks

Spectral models are very computationally efficient and can be applied to model wave propagation over large distances (in the order of hundreds of kilometres).

This class of wave models is able, to a certain extent, account for nonlinear triad and quadruplet wave-wave interactions (various approximations exist) but cannot model the generation of low frequency waves.

Another limitation arises from the fact that spectral models do not resolve the individual waves and do therefore not provide information on the phases of the individual waves. This makes these models (at least theoretically) unsuitable for accurately calculating diffraction around obstacles such as breakwaters. In a study on the reflection and diffraction around breakwaters (Boshek 2009), the spectral model SWAN was unable to replicate the effects of reflection on both sides of a breakwater. For broad directional waves SWAN did however perform remarkably well in this study.

Based on the properties mentioned above, spectral models are here considered unsuitable for simulating the penetration of waves in harbours with complex geometries. They may be used in offshore regions to provide boundary conditions for more advanced nearshore models.

Some examples of models from this class are SWAN (Booij, Ris and Holthuijsen 1999, The SWAN Team (Delft University of Technology) 2007) and WAVEWATCH III (Tolman 2009).

2.2.3 Shallow water models, forced on primary wave group scale

This class of models is based on the coupling of a shallow water model with a spectral model. The spectral model computes the energy of the primary (wind) waves while the shallow water model solves the low frequency waves. The radiation stress induced by the primary waves forms an input for the shallow water models and forces the low frequency waves.

The governing equations in shallow water models are the so called shallow water equations. One method of deriving these (nonlinear) equations is to integrate the Navier-Stokes equations and the continuity equation in the vertical direction, while making certain assumptions.

The key assumption that is made to integrate the equations over depth, thereby eliminating the vertical dimension of the 3D equations, is about the vertical structure of the flow. The assumption is that the vertical acceleration of the fluid can be neglected, or equivalently, that the pressure is hydrostatic. This assumption is valid if the horizontal length scales are much larger than the vertical length scales, so for $kh \ll 1$.

The 2DH shallow water equations, without the inclusion of turbulence stresses and external forces such as bottom friction, Coriolis, wind, etc., read:

$$\begin{aligned}\frac{\partial \zeta}{\partial t} + \frac{\partial h\bar{u}}{\partial x} + \frac{\partial h\bar{v}}{\partial y} &= 0 \\ \frac{\partial \bar{u}}{\partial t} + \bar{u} \frac{\partial \bar{u}}{\partial x} + \bar{v} \frac{\partial \bar{u}}{\partial y} + g \frac{\partial \zeta}{\partial x} &= 0 \\ \frac{\partial \bar{v}}{\partial t} + \bar{u} \frac{\partial \bar{v}}{\partial x} + \bar{v} \frac{\partial \bar{v}}{\partial y} + g \frac{\partial \zeta}{\partial y} &= 0\end{aligned}\tag{6}$$

with x, y horizontal coordinates
 ζ surface elevation, measured upwards from still water level
 d bottom level, measured downwards from still water level
 h water depth, given by $h = \zeta + d$
 \bar{u}, \bar{v} depth averaged flow velocities in x and y directions
 g gravitational acceleration

The above system of (hyperbolic) partial differential equations can be analysed with the method of characteristics. This analysis shows that disturbances in the system propagate with a speed of $c = \sqrt{gh}$, if the mean flow velocity is zero.

This matches exactly with the phase velocity predicted by the linear dispersion relationship, as for the limit $kh \rightarrow 0$ (thus for shallow water), the relation

$$c = \sqrt{\frac{g}{k} \tanh kh}\tag{7}$$

reduces to

$$c = \sqrt{gh}\tag{8}$$

From this expression for the phase velocity it can be seen that frequency dispersion is not included in the shallow water equations, since the phase velocity only depends on the water depth.

The phase velocity does depend on the local water depth and surface elevation, so shallow water waves are subject to amplitude dispersion.

It can be concluded that the shallow water equations cannot be used to model frequency-dispersive wind waves, the hydrostatic pressure assumption would be violated. This class of models is therefore only slightly more useful for modelling wave penetration in harbours than spectral models are. Their main advantage is that they can accurately model the propagation of low frequency waves.

An example of a model from this class (barring non-hydrostatic pressure) is XBEACH (Roelvink, et al. 2010) . Another possibility to obtain a model of this class is for instance to couple SWAN to Delft3D-Flow.

2.2.4 Mild-slope models

This class of models has often been applied to study wave penetration in ports. The models are based on the so called mild-slope equation, which can be derived from potential flow theory. The vertical dimension of the 3D flow equations is eliminated by assuming that the vertical structure of the flow is equal to the vertical structure of flow under Airy waves, and subsequently integrating over depth. Airy waves are propagating harmonic waves with relatively small amplitude that represent a solution to the 3D flow equations with certain linearised boundary conditions.

Because of the linearization in the derivation, the mild-slope equation can be solved in the frequency domain instead of in the time domain (the mild-slope equation is an elliptic partial differential equation).

Even though the mild-slope equation only describes the propagation of harmonic waves, mild-slope models are still able to approximate wave spectra. This is achieved by a superposition of wave components with different frequencies and directions, which is a computationally efficient method to approximate a wave spectrum. Due to the linear nature this class of models cannot be used to model nonlinear waves or nonlinear wave-wave interactions.

Mild-slope models impose no restrictions on the kh -value of waves, which means that short waves can be modelled in deep water without loss of accuracy. Mild-slope models do have limitations when it comes to wave amplitude, wave steepness, and bottom slopes (hence the name mild-slope models). These limitations originate from the assumption that is made about the vertical structure of the flow and are equivalent to the limitations of linear or Airy wave theory.

The mild-slope model PHAROS (Deltares 2013) is elaborated in Section 3.2. Another example of a model from this class is CGWAVE (Demirbilek en Panchang 1998).

2.2.5 Boussinesq-type models

This class of models is based on Boussinesq-type equations which can be, just like the mild-slope equations, derived from potential flow theory. The essence of Boussinesq modelling is again to eliminate the vertical dimension from the 3D potential flow equations (to increase computational efficiency), while taking the effects of the vertical structure of the flow into account.

The key difference with the mild-slope equation lies in the assumptions that are made about the vertical structure of the flow. Instead of imposing the vertical structure of a linear Airy wave, the vertical structure is now approximated, for instance with a perturbation series expansion of the velocity potential at the bottom. Moreover, the free surface boundary conditions that are imposed to derive Boussinesq-type equations are not necessarily linearised.

Boussinesq-type equations can be formulated in terms of surface elevation and depth averaged velocity, the same format in which the standard shallow water equations are usually written. By way of example, the Boussinesq-type model as derived by Peregrine (1967) is shown below, written in this format.

$$\begin{aligned} \frac{\partial \zeta}{\partial t} + \frac{\partial h\bar{u}}{\partial x} + \frac{\partial h\bar{v}}{\partial y} &= 0 \\ \frac{\partial \bar{u}}{\partial t} + \bar{u} \frac{\partial \bar{u}}{\partial x} + \bar{v} \frac{\partial \bar{u}}{\partial y} + g \frac{\partial \zeta}{\partial x} &= \frac{1}{2} d \left(\frac{\partial^3 (\mathbf{d}\bar{u})}{\partial t \partial x^2} + \frac{\partial^3 (\mathbf{d}\bar{u})}{\partial t \partial x \partial y} \right) - \frac{1}{6} d^2 \left(\frac{\partial^3 \bar{u}}{\partial t \partial x^2} - \frac{\partial^3 \bar{u}}{\partial t \partial x \partial y} \right) \\ \frac{\partial \bar{v}}{\partial t} + \bar{u} \frac{\partial \bar{v}}{\partial x} + \bar{v} \frac{\partial \bar{v}}{\partial y} + g \frac{\partial \zeta}{\partial y} &= \frac{1}{2} d \left(\frac{\partial^3 (\mathbf{d}\bar{v})}{\partial t \partial y^2} + \frac{\partial^3 (\mathbf{d}\bar{v})}{\partial t \partial y \partial x} \right) - \frac{1}{6} d^2 \left(\frac{\partial^3 \bar{v}}{\partial t \partial y^2} - \frac{\partial^3 \bar{v}}{\partial t \partial y \partial x} \right) \end{aligned} \quad (9)$$

with x, y horizontal coordinates
 ζ surface elevation, measured upwards from still water level
 d bottom level, measured downwards from still water level
 h water depth, given by $h = \zeta + d$
 \bar{u}, \bar{v} depth averaged flow velocities in x and y directions
 g gravitational acceleration

Notice that the continuity equation is exactly the same as in the shallow water equations, since it is an exact relation. The momentum equations of the Boussinesq models contain extra higher order (3rd order or higher) mixed derivatives that correct the vertical structure of the flow and enable the modelling of frequency dispersion to a certain accuracy.

The frequency dispersion in this class of models can be improved by adding higher order dispersion terms to the momentum equations. This expands the models application boundaries towards deeper water (higher k_h values). The drawback here is that the complexity of the momentum equations and thereby the computational costs to solve them increases.

In deriving Boussinesq-type equations the dimensionless depth k_h (which is related to frequency dispersion) is usually incorporated to the same order of accuracy as the parameter a/h (which is related to amplitude dispersion). By adjusting the accuracy of the approximation in these parameters, Boussinesq-type equations with different dispersion and shoaling characteristics can be obtained. See, for instance, (Madsen and Schäffer 1998) and (Nwogu 1993).

Instead of deriving Boussinesq-type models directly from the 3D flow equations, new models can also be obtained by mathematically transforming other models. With certain transformations equivalent sets of equations (equivalent within the order of approximation, i.e. asymptotically equivalent) with enhanced properties can be obtained.

Some examples of possible transformations, such as replacing the depth averaged velocity with a velocity near the bottom, at the free surface or an arbitrary depth, are given in (Borsboom 1998). Valuable properties like mass and momentum conservation, higher order of accuracy, suitability for numerical implementation etc., can be obtained from such transformations.

The many assumptions and approximation techniques that are possible for the vertical structure of the flow have led to the development of many different Boussinesq-type wave models in the last few decades. An extensive elaboration on different techniques to derive Boussinesq-type equations is given in (Dingemans 1994) and (Kirby 2003).

Modelling wave breaking with Boussinesq-type models is not straightforward because the flow is assumed to be irrotational to enable the derivation of the equations.

One approach is to apply the concept of surface rollers (Schäffer, Madsen and Deigaard 1993), which are considered as a separate volume of water on the wave surface. The momentum flux associated with the surface rollers, which depends on parameters such as the roller thickness, is incorporated in the momentum equation. The initiation of breaking is determined from the slope of the water surface.

Another method to include the energy losses due to rotational friction is to add artificial viscosity terms to the momentum equations. This approach is similar to turbulence modelling. The eddy viscosity can be determined algebraically (possibly based on surface roller parameters) or modelled with a turbulent kinetic energy transport equation (Nwogu 1996).

Boussinesq-type models are relatively computationally expensive but do account for nonlinear wave processes. The equations are in principle only accurate for relatively shallow water. Most models that are used in practice are designed to produce accurate results for kh -values (dimensionless water depth) of up to 3 or 4.

Some examples of Boussinesq-type models are: BOUSS-2D (Nwogu en Demirbilek 2001), FUNWAVE (Kirby, Wei, et al. 1998), VBM (Klopman, Dingemans and Van Groesen 2010) and TRITON (Deltares 2008). The TRITON model is described in Section 3.3.

2.2.6 Non-hydrostatic models

The development of this class of model started approximately 15 years ago (Casulli and Stelling 1998, Stansby and Zhou 1998), and the application rapidly increased in the past decade. The system of equations solved by these models consists of the shallow water equations and a vertical momentum equation. The horizontal momentum equations are extended with a term containing the non-hydrostatic pressure. This term takes into account the vertical structure of the flow in an exact manner and enables the modelling of frequency dispersion to an arbitrary accuracy.

The 3D flow equations are discretised in vertical direction by splitting the water depth in vertical layers. This means that the vertical structure of the flow is now part of the solution – it is not imposed like in mild-slope models or Boussinesq-type models. It also means that no dimensions of the 3D flow equations are eliminated, which attributes to the relatively high computational costs.

The frequency dispersion in this class of models is improved just by increasing the vertical grid resolution. This way the models application boundaries can be extended towards deeper water (higher kh values), albeit at the loss of computational efficiency.

The free surface is considered as a function of the horizontal coordinates. This approach allows the use of a low vertical grid resolution, making computations sufficiently efficient to enable the modelling of waves in areas of several kilometres. The inherent limitation of this approach is that overturning waves cannot be simulated.

This class of models is computationally expensive but accounts for nonlinear wave processes. The maximum kh -value that can be accurately modelled depends on the number of vertical layers. With 2 vertical layers these models can already be accurate up to a kh -value of about 4 (Zijlema, Stelling and Smit 2011).

Examples of this class of models are NHWAVE (Ma, Shi and Kirby 2012) and SWASH (Zijlema, Stelling and Smit 2011), which is described in Section 3.4.

2.2.7 Full free-surface Navier-Stokes models

This class of models is the most computationally expensive of the models described in this chapter. It can accurately model nonlinear wave processes including wave breaking, but it is currently not feasible to apply this class of models in harbour-sized domains for engineering purposes.

The models solve the Reynolds Averaged Navier-Stokes equations, possibly using various turbulence models to close the system of equations. In theory the Navier-Stokes equations could also be solved directly, including all turbulence features, but this is even more (orders of magnitudes) computationally expensive due to the very small spatial and time scales that need to be resolved.

The interfaces between air and fluid can be tracked by assigning a value to each grid cell that indicates whether or not the cell contains fluid. Such an approach enables the modelling of overturning waves. Unfortunately these methods require a high vertical resolution which makes them computationally expensive. An example of such a method is the volume-of-fluid (VOF) method.

Examples of a free-surface Navier-Stokes model are IH2VOF (Losada, et al. 2008) and COMFLOW (Kleefsman, et al. 2005).

2.2.8 Conclusion

Several classes of numerical wave models are treated in this chapter. The flowchart in Figure 2.3 gives an indication of what type of wave model is the most appropriate to model wave penetration in a particular situation. By complex geometry a situation is meant where diffraction is significant, e.g., when breakwaters or quay walls are present.

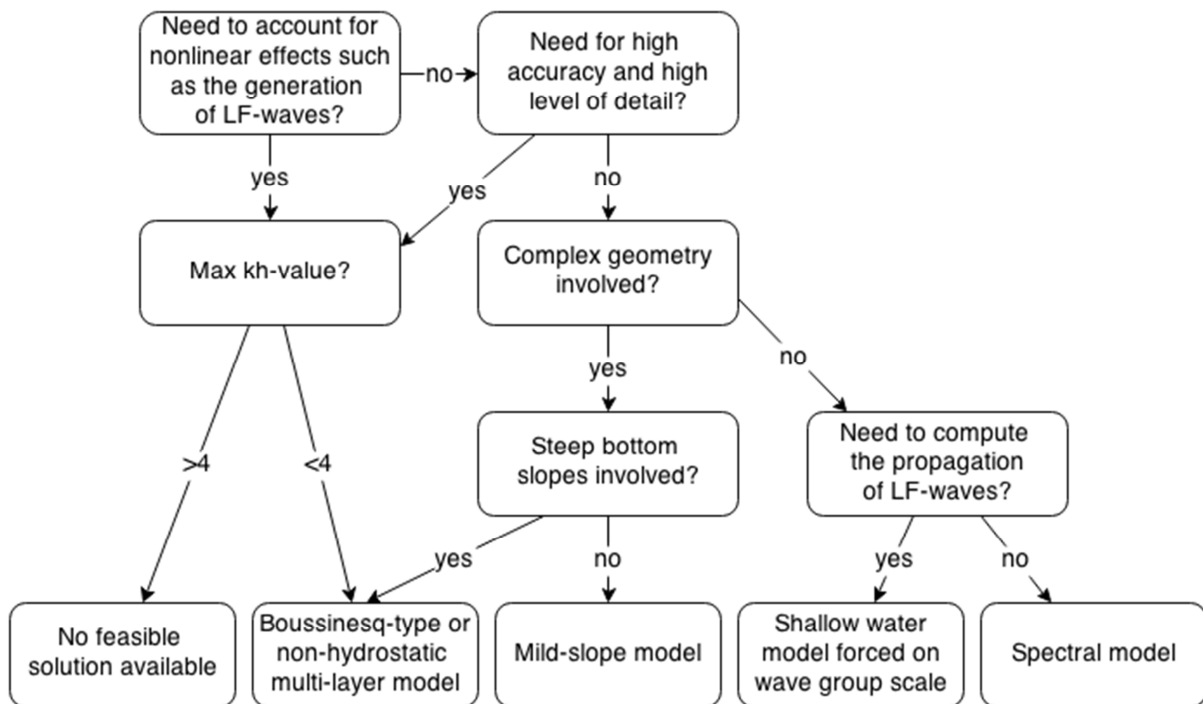


Figure 2.3 – Flowchart for selecting a class of wave models

2.3 Application boundaries for operational numerical wave models in ports

2.3.1 Type of application

A model's application boundaries depend on the type of application for which the model is used. The type of application considered in this study is the modelling of wave penetration in ports, for engineering purposes such as downtime studies.

2.3.2 Formulations and criteria

Application boundaries can be formulated in many ways. In literature application boundaries are for instance often formulated in terms of the maximum dimensionless water depth (kh) for which the phase error is less than 1-3%.

Another possibility is to consider wave conditions in a broader sense. For the application considered here, wave conditions ranging from everyday wave conditions up to wave conditions for which port operations have to be shut down (let's say a once in a year storm) are relevant. Wave processes can also be used to distinguish areas of application. For wave penetration in harbours, the modelling of reflection, diffraction and shoaling is considered crucial.

In particular waves with periods close to the eigen periods of vessels, mooring systems or basins are of importance as they can cause the most hindrance to port operations due to resonance. These eigen periods can range from seconds (the rolling motion of a vessel for instance) to several minutes (for example standing waves in basins).

The required accuracy of wave heights and mean wave periods for the engineering purposes considered here is estimated at around 15%. Requiring higher accuracy is not considered useful, as uncertainties in model input, such as bathymetry or wave conditions, are in practice also contributing to a model's result.

The accuracy of predicted wave heights will in general depend on the complexity of the port layout and the location within the port. When the amount of structures (e.g. breakwaters) that are affecting wave conditions at a certain location increases, the inaccuracy of model predictions will generally increase as well. The wave heights on the other hand will in general also be lower at these locations, so the absolute errors may still be considered sufficiently small.

From a more practical perspective, computational efficiency and ease of use could form application boundaries. Acceptable criteria in this regard depend on the type of study that is carried out and the time available for it. Ideally, a simulation should not take more than a night to finish.

2.4 Conclusions

Reflection, shoaling and diffraction are identified in this chapter as having the most substantial effect on primary wave penetration in ports. Harbour oscillations can be of great importance for port operations as well. An investigation of existing classes of numerical wave models subsequently shows that mild-slope models, Boussinesq-type models and non-hydrostatic models have the most potential when it comes to modelling wave penetration in ports for engineering purposes. The first research sub-question has thus been answered. The kind of application boundaries that are sought in this study are outlined as well.

Now that the most suitable model classes are selected, the next chapter will be on specific operational wave models from these classes. This next chapter will form the basis for the answering of the second research sub-question.

3 Selection of numerical wave models for further study

3.1 Introduction

Based on the investigation of classes of numerical models presented in Section 2.2, the following classes of models are considered to have the most potential when it comes to modelling wave penetration in ports:

- Mild-slope models
- Boussinesq-type models
- Non-hydrostatic models

For each of these model classes, one specific operational model is chosen and elaborated in a separate section. The theoretical differences (e.g. governing equations, numerical techniques, boundary conditions, schematisations) between these models are presented. An overview of previous studies regarding the validation of these models is provided as well.

The following operational wave models are chosen:

- PHAROS, a mild-slope model developed at Deltares
- TRITON, a Boussinesq-type wave model developed at Deltares
- SWASH, a non-hydrostatic wave-flow model developed at Delft University of Technology

3.2 PHAROS

3.2.1 Introduction

PHAROS (which is an acronym for Program for HARbor Oscillations) is a wave model developed by Deltares. The model is intended to be used for studying harbour oscillations and penetration of wind waves, in harbours with complex geometries. The model is relatively computationally efficient and accounts for the following wave processes:

- Shoaling (depth induced and current induced)
- Refraction (depth induced and current induced)
- Diffraction
- Seiching
- Dispersion
- Reflection
- Transmission
- Dissipation by wave breaking and bottom friction

The software package consists of four modules. The core module is the so called “long crested module”, that computes the propagation of monochromatic waves. The “directional spreading module” and the “spectral module” can be used to simulate waves that only have a directional spreading and waves that are defined by a full (2D) wave spectrum respectively. The computations are then based on a superposition of (monochromatic) wave components that are computed with the long crested module. The fourth module is called the “seiching module” and can be used to investigate resonance of harbour basins. For this thesis PHAROS version 9.11 is used.

3.2.2 Modelling background

Equations and assumptions

The underlying equations in PHAROS are based on the elliptic mild-slope equation as derived by Berkhoff (1972, 1976). The starting point of the derivation of this equation is the Laplace equation, which is obtained by writing the continuity equation in terms of velocity potential:

$$\frac{\partial^2 \phi}{\partial x^2} + \frac{\partial^2 \phi}{\partial y^2} + \frac{\partial^2 \phi}{\partial z^2} = 0 \quad (10)$$

combined with the linearised kinematic free surface boundary condition:

$$\frac{\partial \phi}{\partial z} = \frac{\partial \zeta}{\partial t} \quad \text{at } z = 0 \quad (11)$$

the linearised dynamic free surface boundary condition:

$$\frac{\partial \phi}{\partial t} + g\zeta = 0 \quad \text{at } z = 0 \quad (12)$$

and the bottom boundary condition:

$$\frac{\partial \phi}{\partial z} + \frac{\partial \phi}{\partial x} \frac{\partial h}{\partial x} + \frac{\partial \phi}{\partial y} \frac{\partial h}{\partial y} = 0 \quad \text{at } z = -h(x, y) \quad (13)$$

with	x, y	horizontal coordinates
	z	vertical coordinate
	ϕ	three-dimensional velocity potential ($u = \frac{\partial \phi}{\partial x}$, $v = \frac{\partial \phi}{\partial y}$, $w = \frac{\partial \phi}{\partial z}$)
	ζ	surface elevation, measured upwards from still water level
	h	water depth
	g	acceleration due to gravity

This starting point is equivalent to the starting point of the derivation of linear wave theory (for the complete derivation of the linear wave theory reference is made to (Dean and Dalrymple 1984)). The mild-slope equations and linear wave theory therefore share some important assumptions. These assumptions can be summarised as follows:

- The fluid is assumed to be ideal, this implies that the fluid is considered as homogenous, incompressible and inviscid.
- The flow is assumed to be irrotational, so that water particles do not rotate.
- The wave amplitude is assumed to be much smaller than the water depth.
- The wave steepness, expressed as wave amplitude over wave length, is assumed to be small

The first two assumptions are necessary to be able to define the velocity potential function. The last two assumptions have to be made to allow the linearisation of the free surface boundary conditions. Some other, less restrictive, assumptions are that the surface tension and Coriolis effect can be neglected and that the pressure at the free surface is constant and uniform.

Linear wave theory imposes two periodical boundary conditions on both lateral sides of the domain to obtain a well posed two-dimensional (2DV) boundary value problem. A solution to this problem is a progressive harmonic wave, described by:

$$\phi = \frac{H}{2} \frac{g}{\omega} \frac{\cosh k(h+z)}{\cosh kh} \sin(kx - \omega t) \quad (14)$$

or rewritten in terms of surface elevation using the dynamic free surface boundary condition:

$$\zeta(x, t) = \frac{1}{g} \frac{\partial \phi}{\partial t} \Big|_{z=0} = \frac{H}{2} \cos(kx - \omega t) \quad (15)$$

with $\omega^2 = gk \tanh kh$, the linear dispersion relationship

t time
 H wave height
 k wave number

In the mild-slope equation, which is 2DH, the vertical dimension is eliminated. This is done by first considering the velocity potential as the product of two functions:

$$\phi(x, y, z) = Z(h, z) \phi(x, y) \quad (16)$$

The dependence of the velocity potential with the vertical coordinate is now considered to depend primarily on $Z(h, z)$. $Z(h, z)$ is considered to depend only weakly on the horizontal coordinates through $\mathbf{h}(x, y)$.

For $Z(h, z)$ the solution of the linear wave theory for the vertical structure of the flow under a harmonic wave is now taken (compare it to equation (14)):

$$Z(h, z) = \frac{\cosh k(h+z)}{\cosh kh} \quad (17)$$

∇_z can be shown to be proportional to ∇_h , see (Dingemans 1994). The assumption that $Z(h, z)$ depends only weakly on the horizontal coordinates leads to the mild-slope condition that demands that ∇_h is small, usually denoted as:

$$|\nabla h| / kh \ll 1 \quad (18)$$

Assuming that the vertical structure of the wave motion is given by $Z(h, z)$ allows the vertical dimension to be eliminated by integrating the equations over the depth, yielding the mild-slope equation in the form as derived by Berkhoff (1972, 1976):

$$\nabla \cdot (cc_g \nabla \phi) + \omega^2 \frac{c_g}{c} \phi = 0 \quad (19)$$

with $c = \omega / k$

$$c_g = nc$$

$$n = \frac{1}{2} \left(1 + \frac{2kh}{\sinh 2kh} \right)$$

Equation (19) can also be written in terms of surface elevation and wave number:

$$\nabla \cdot (cc_g \nabla \zeta) + k^2 cc_g \zeta = 0 \quad (20)$$

PHAROS is based on this mild-slope equation, (optionally) including effects of ambient currents and energy dissipation. The model equation is expressed as (Deltares 2013):

$$\nabla \cdot (cc_g \nabla \phi) + 2i\omega \vec{U} \cdot \nabla \phi + (k^2 cc_g + \omega^2 - \omega_r^2 + i\omega \nabla \cdot \vec{U}) \phi = -i\omega_r W \phi \quad (21)$$

with i imaginary number

$$\phi \quad \text{complex velocity potential: } \phi = -i \frac{H}{2} \frac{g}{\omega} \frac{\cosh k(h+z)}{\cosh kh} e^{i(kx - \omega t)}$$

\vec{U} current velocity vector

$\omega_r = \omega - \vec{k} \cdot \vec{U}$ with \vec{k} the wave number orientated in the wave direction

w energy source term representing energy dissipation by breaking and bottom friction

For a detailed description of the additional terms in this equation, that add energy dissipation and ambient currents to the equation, one is referred to (Deltares 2013) and (Kostense, et al. 1986).

Boundary conditions

Along open boundaries PHAROS applies a radiation boundary condition in order to let waves freely propagate out of the computational domain. Outgoing waves are described by Hankel functions (Deltares 2013), assuming the water depth outside the computational domain (and thus also along the open boundary) is constant. However, this assumption is often not valid. Xu et al. (1996) show that the violation of this assumption can have a substantial effect on the model results, by comparing it with the results from a model (CGWAVE, (Demirbilek and Panchang 1998)) that uses parabolic approximations of the mild-slope equation as open boundary conditions.

Along closed boundaries partial reflection or combined partial reflection and transmission boundary conditions can be applied in PHAROS. Two partial reflection boundary conditions are available in PHAROS, they are called the reflection-1 and reflection-2 types.

The reflection-1 boundary condition is based on the Sommerfeld condition. This condition states that energy which is radiated from sources must scatter into infinity, and no energy may be radiated from infinity into the field. Mathematically, this condition can be denoted as:

$$\left(\frac{\partial}{\partial |x|} - ik \right) (\phi - \phi_{In}) \rightarrow 0 \quad \text{as } |x| \rightarrow \infty$$

with ϕ_{In} the incoming velocity potential

PHAROS requires the user to specify the reflection coefficient and the estimated angle of wave incidence. The reflection-1 boundary condition in PHAROS is:

$$\left(\frac{\partial}{\partial n} - ik \frac{1-R}{1+R} \cos \alpha_1 \right) \phi = 0 \quad (22)$$

with n the coordinate normal to the boundary pointing outward
 R the reflection coefficient
 α_1 the user specified angle of wave incidence

The actual reflection coefficient depends also on the actual angle of wave incidence, as shown in Figure 3.1 (source: (Deltares 2013)).

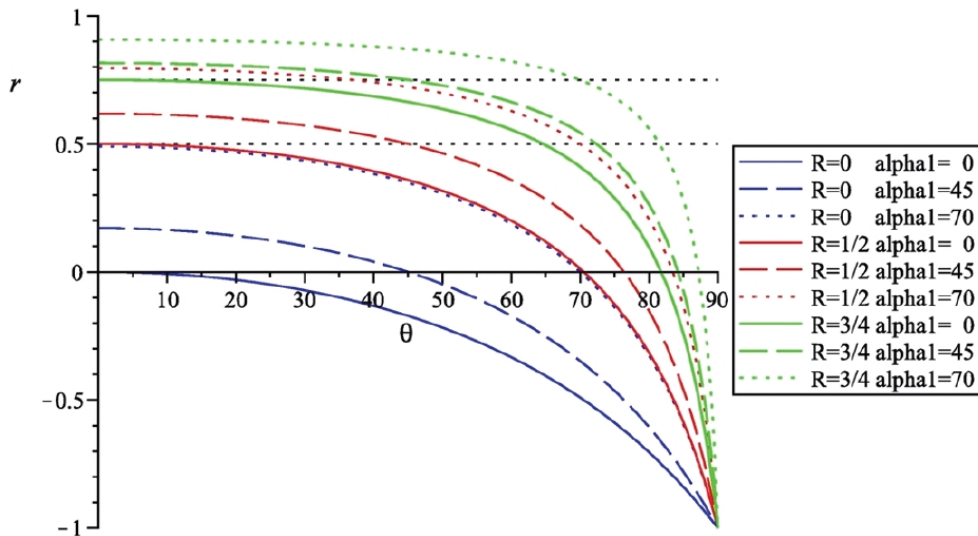


Figure 3.1 – Actual (or resulting) reflection coefficient r of the reflection-1 boundary condition as a function of angle θ with which the waves approach the considered boundary, for several combinations of user-specified reflection coefficient R and estimated wave angle α_1 . Source: (Deltares 2013)

The reflection-2 boundary condition is based on the second-order Higdon boundary condition. It requires the user to specify two incoming wave directions. Theoretically, this boundary condition is better than the reflection-1 boundary condition, because it is much less dependent on the difference between the user specified incoming wave direction α and the actual incoming wave direction θ .

This is illustrated in Figure 3.2 (source: (Deltares 2013)), cf. Figure 3.1.

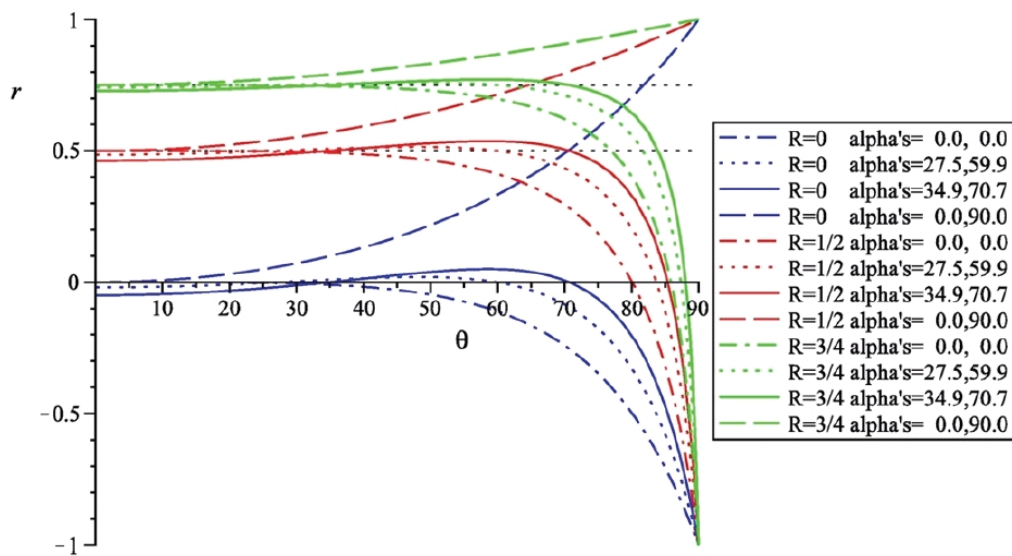


Figure 3.2 - Actual (or resulting) reflection coefficient r of the reflection-2 boundary condition as a function of angle θ with which the waves approach the considered boundary, for several combinations of user-specified reflection coefficient R and estimated wave angles α_1 and α_2 . Source: (Deltares 2013)

Unfortunately the current version of PHAROS has some issues with the implementation of this boundary condition (Deltares 2010). It is therefore advised to use the reflection-1 boundary condition.

Numerical aspects

PHAROS uses a finite element method to numerically solve the elliptic partial differential equation and its boundary conditions. The computational domain is discretised with a triangular grid.

The system of equations that is obtained is solved using either Gaussian elimination (if the system of equations is small) or an iterative method called CGS (conjugate gradient squared) (Sonneveld 1989).

The directional spreading and spectral module

These modules can be used to take the effects of directional and frequency spreading in the applied wave conditions into account. The wave height is then calculated as the sum of a number of monochromatic waves, each with a different frequency and direction. The weight of each wave component in the summation is based on the specified energy density spectrum of the incoming wave.

The more wave components are computed the more accurate the computed wave height fields become. Van Os (2009) describes how taking more wave components into account results in more subtle peaks and troughs in the computed wave field, but seems to increase the average wave height at the same time. The physical correctness of this behaviour is explained in the report as well.

Post-processing and interpretation of results

The interpretation of wave fields computed with PHAROS requires some special attention. This is especially the case if one wants to compare the computed wave field with point values from another source (e.g. measurements). The difficulty here is that the wave fields computed by PHAROS consist of standing waves, and have nodal points where the computed wave height can be very small and

antinodes where the computed wave height can be quite large. The exact location where a point value is extracted from the computed wave height field can therefore have a significant influence.

In (Van Os 2009) it is therefore advised to compare measurements (corresponding to one specific location in the computational domain) and computation results by plotting the measurements in the computed wave field.

Another option that is presented is to make a boxplot of all computed wave heights in a circle around the measurement location. It can then easily be assessed if the measurement lies inside the range of computed values. For the circle a radius of 0.5 to 1 times the local wave length is advised.

To obtain a representative value of the wave height within a certain area Ω , Van Os (2009) gives the following formula:

$$\overline{H}_{\Omega} = \sqrt{\frac{\sum_{i=1}^N H_i^2}{N}} \quad (23)$$

Using this formula guarantees energy conservation within the area Ω , since wave energy per horizontal area is proportional to the square of the wave height.

Figure 3.3 shows the effect of applying formula (23) to every grid point of a computed wave field. Information on the standing wave patterns is lost, but the wave field is therefore easier to interpret and point values can directly be extracted.

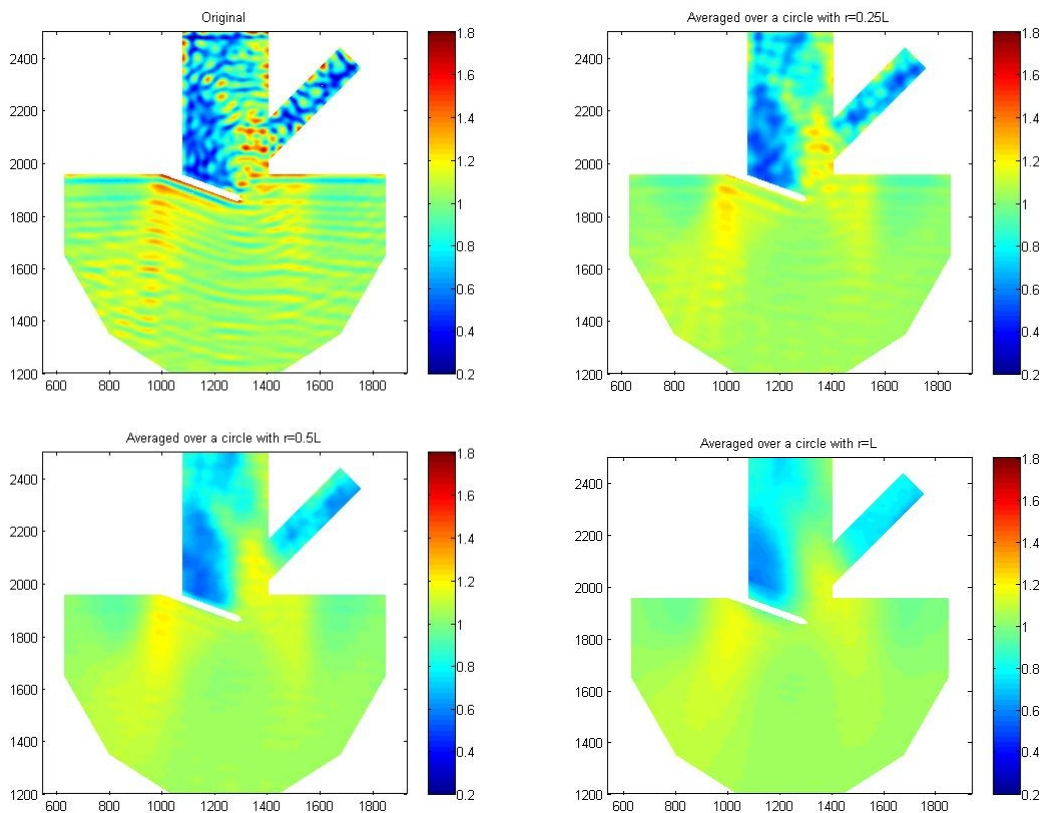


Figure 3.3 – Top left: unprocessed wave heights, Others: averaged wave heights, using different radii

In order to obtain accurate results with PHAROS, correct incoming wave directions must be provided at reflection boundaries. PHAROS therefore includes a wave splitting tool called r-DPRA (Deltares 2013). This tool can be used to distinguish incoming wave components and reflected wave components from a complex wave field.

The tool is based on the r-DPRA (rotating Directional Phase Resolving Analysis) technique developed by De Jong and Borsboom (2012). It analyses wave time series in a number of points around the point of interest. For each frequency the method determines the wave heights, directions, and phases. The depth and wave field should not vary too much in the area where the time series are analysed.

3.2.3 Earlier validation studies and benchmark results

Benchmark results of PHAROS and other mild-slope models

An important limitation of the mild-slope equation is of course the mild slope condition which states that the gradient in bed level should be small. From numerical experiments Booij (1983) concluded that the mild-slope equation gives good results for slopes up to 1:3.

Several benchmark tests are used in literature to assess model performance regarding combined refraction and diffraction. Two well-known benchmark tests are Homma's island and the Berkhoff shoal. Homma's island considers long waves around a circular island, for which Homma (1950) derived an analytical solution using the shallow water assumption ($c = c_g = \sqrt{gh}$). This test case can also be considered as a benchmark for radiation boundary conditions. The Berkhoff shoal considers waves propagating over an elliptic shoal situated on a slope (1:50), for which measurements were carried out in a physical model (Berkhoff, Booij and Radder 1982).

PHAROS and CGWAVE (another mild-slope model) were benchmarked using these test cases. In (WL | Delft Hydraulics 1991) and (Demirbilek and Panchang 1998) it is shown that PHAROS respectively CGWAVE are able to accurately reproduce the Homma's island test case.

In (Demirbilek and Panchang 1998) the Berkhoff shoal is also used for validation, and it is shown that approximately 15 nodes per wavelength are necessary to obtain reasonable results.

Another interesting test case that was considered in (Demirbilek and Panchang 1998) is the resonance in a rectangular harbour. It is shown that analytical results and lab data can be reproduced, and that reflection coefficients and bottom friction have a large influence on the computed amplification factors.

Earlier validations of PHAROS for wave penetration in harbours

Results from PHAROS computations have been compared with measurements obtained from physical models of ports several times.

Van der Hout et al. (2009) used the scale model tests of the port of Almeria to validate PHAROS, TRITON, and SWAN. They concluded the following about the performance of PHAROS: "In the directional spreading run, the wave heights (H_{m0}) were overestimated by 30%-45%. In the spectral run, the computed wave heights were even higher. It was identified that a possible cause for this overestimate is that the weighted summation of the individual wave components might be a conservative approach." (Van der Hout, Wijdeven and Schouten 2009).

Van Os (2009) concluded that the weighted summation of the individual wave components in PHAROS is physically correct and cannot be a source of error. After analysing the Almeria case Van

Os (2009) also concludes that PHAROS shows better results if the models output is presented in a different manner. Instead of comparing point values the method as described in Section 3.2.2 should be used.

Reijmerink (2012) investigated the application boundaries of PHAROS for determining the Hydraulic Boundary Conditions (as specified by the Dutch Water Act) in ports. PHAROS and TRITON simulations were compared for several schematised (academic) port layouts. Scale models tests of ports were also modelled in PHAROS and PHAROS results were compared with measurements. It was concluded that PHAROS can compute significant wave heights accurately enough ($\pm 10\%$) to apply it for determining the Hydraulic Boundary Conditions in ports, regardless of the complexity of the port layout or the amount of directional spreading of the incoming waves.

It was further advised to use 25 wave components for PHAROS computations, and consider wave heights in a circle with a radius of 0.5 times the local wave length when comparing point values.

Conclusion

Based on academic benchmark tests it can be concluded that PHAROS is capable of computing the refraction and diffraction of linear waves up to a slope of 1:3.

From the validation studies of PHAROS for wave penetration in ports it can be concluded that PHAROS can compute significant wave heights accurately enough to be used for most engineering purposes. However, choosing the parameters of the reflective boundary conditions and interpreting the computed wave fields must be done carefully.

In case basin resonance might be relevant, the effect of bottom friction should also be studied with extra care.

3.3 TRITON

3.3.1 Introduction

TRITON is a Boussinesq-type wave model being used and developed at Deltares. The aim of the model is to simulate wave propagation in nearshore regions and harbours. It can account for the following wave processes.

- Shoaling
- Refraction
- Diffraction
- Dispersion
- Nonlinear wave-wave interactions (including surf beat and triads)
- Wave breaking
- Partial reflection
- Wave-induced currents

For this thesis version 1.18.09 of the TRITON software was used, without the implementation of the higher-order extension described in (Wellens 2010). The software is not (yet) commercially available but has been used by Deltares in some of their projects.

3.3.2 Modelling background

Equations and assumptions

The Boussinesq-type equations on which TRITON is based can be derived from the 3D potential flow equation with nonlinear boundary conditions. The vertical dimension is eliminated by approximating the variation in this direction by means of a truncated perturbation series expansion. The complete derivation is given in (Borsboom 1998) and will not be treated here. The final equations (formulation taken from (Borsboom, Groeneweg, et al. 2000)) are presented below:

$$\begin{aligned} \frac{\partial H}{\partial t} + \nabla \cdot \mathbf{q} &= 0 \\ \frac{\partial \mathbf{q}}{\partial t} + \nabla \cdot (\bar{\mathbf{u}}\mathbf{q}) + \nabla P &= p_b \nabla h \end{aligned} \quad (24)$$

with $P = g \frac{\tilde{H}^2}{2}$, $p_b = g \left(\frac{3\tilde{H}}{2} - \frac{H}{2} - \frac{H}{4} \nabla H \cdot \nabla \zeta \right)$

$$\begin{aligned} \tilde{H} - \alpha H^2 \nabla^2 \tilde{H} - \beta H \nabla h \cdot \nabla \tilde{H} &= H - \left(\alpha - \frac{1}{3} \right) H^2 \nabla^2 H - \left(\beta - \frac{1}{2} \right) H \nabla h \cdot \nabla H + \\ -\frac{1}{2} (\nabla h \cdot \nabla h) H - \frac{1}{3} (H \nabla^2 h) H \end{aligned}$$

H	total water depth, given by $H = \zeta + h$
\tilde{H}	auxiliary parameter
ζ	surface elevation, measured upwards from still water level
h	bottom level, measured downwards from still water level
\mathbf{q}	depth integrated velocity vector, $\mathbf{q} = H\bar{\mathbf{u}}$
$\bar{\mathbf{u}}$	depth averaged flow velocity vector
g	gravitational acceleration
t	time
α	dispersion parameter
β	shoaling parameter

Notice that the momentum equation contains terms that are equivalent to the terms found in the standard shallow water equations (6), and is extended with a number of (rather complex) terms to include frequency dispersion. The momentum equation has later been extended with artificial viscosity terms and more recently with even higher order dispersion terms.

The main features of this Boussinesq-type equation are its depth averaged mass and momentum conservation and its independence of vertical reference level (M. Borsboom, N. Doorn, et al. 2000).

The inclusion of higher order terms was carried out to improve the modelling of nonlinear wave processes, in particular the generation of low frequency waves in intermediate water depths (De Bont 2010, Wellens 2010). This higher order extension is not used in this project however.

Artificial eddy viscosity terms were added to the momentum equation to incorporate the effects of wave breaking. In TRITON the eddy viscosity is modelled algebraically (i.e. calculated directly from

the flow variables), using the ideas behind the surface roller concept, see (M. Borsboom, N. Doorn, et al. 2001) and (Groeneweg, et al. 2002).

According to Deltares (2008), TRITON “is designed to be applied for water depths up to 20m, wave periods of 5 to 15 seconds, and wave heights up to 5m”. Furthermore, shoaling should be modelled accurately up to slopes of approximately 1:10. The application range for which the model is designed can be expressed more formally using certain dimensionless parameters as follows:

- $kh < 4$
- $a/h < 0.25$
- $k^2ha < 0.25$

with k wave number
 h water depth
 a wave amplitude

The balance between the accuracy with which frequency dispersion and shoaling are modelled can be adjusted by varying the dispersion parameter α and shoaling parameter β in Equation (24).

Boundary conditions

The following types of boundary conditions can be imposed with TRITON (Deltares 2008):

- ‘Monochromatic’
- ‘Closed’
- ‘Partial’
- ‘Timesignal’
- ‘Spectrum’
- ‘Outflow’

Incoming waves can be specified with the boundary conditions ‘Monochromatic’, ‘Timesignal’ and ‘Spectrum’. For boundaries where waves are reflected or propagate out of the domain the ‘Closed’, ‘Partial’ and ‘Outflow’ boundaries should be used.

The absorbing boundary conditions in TRITON are not based on sponge layers but on a more complex method. This method involves decomposing waves in the vicinity of boundaries. A detailed description of this boundary condition is provided in (Borsboom, Groeneweg, et al. 2001).

Numerical aspects

The governing equations in TRITON are discretized on a rectangular grid and an explicit fourth-order Runge-Kutta type scheme is employed to integrate the equations in time (M. Borsboom, N. Doorn, et al. 2000). The explicitness of the numerical scheme means the time step for integration has to be restricted in order to obtain numerically stable simulations. In TRITON the following time step restriction is applied:

$$Cr = \left(\frac{|u|+c}{\Delta x} + \frac{|v|+c}{\Delta y} \right) \Delta t \leq 2\sqrt{2} = 2.8284 \quad (25)$$

with	c_r	Courant number
	Δt	time step
	$\Delta x, \Delta y$	grid size in x- and y-direction
	u, v	flow velocity in x- and y-direction
	c	celerity
	d	depth
	g	acceleration due to gravity

This CFL condition ensures that the numerical domain of dependence includes the analytical domain of dependence.

Post processing

The output of TRITON consists of surface elevations, depths and flow velocities. Output locations can be specified using transects or points. The Delft3D-QuickPlot module can be used to visualise the results of a computation.

3.3.3 Earlier validation studies and benchmark results

Benchmark results of TRITON

In (Caires 2009) flume measurements were compared to TRITON simulations. The five bottom profiles of the one-dimensional cases were idealizations of the bottom profile in front of the Petten sea defence (which is seen as a characteristic foreshore) and 12 hydraulic boundary conditions were tested. The simulated wave conditions were within the ranges: $0.04 < a/h < 0.14$ and $0.7 < kh < 1.6$ at the location of interest.

Good similarities between measurements and computations were found at this location for these conditions (less than 10% error in wave height, up to 25% error in wave period). Analyses of the results indicated that the largest nonlinear effects lead to the largest errors. The errors were dominated by the underestimation of the low-frequency energy in the spectrum.

Earlier validations of TRITON for wave penetration in harbours

Boeyinga (2010) investigated whether TRITON is suitable for the purpose of workability assessment of floating equipment in port applications. In this study the port of Ashdod was used as a case study and simulation results of TRITON were compared to measurements from a physical model of this port. The simulated waves were weakly nonlinear and can be classified as second order Stokes waves.

After one attempt of tuning reflection coefficients for one wave condition the relative differences in wave heights calculated by TRITON and measured in the physical model were on average between 3-16% for areas outside the port and in the port entrance. Further into the port the relative differences were larger but the maximum wave height here was only 10 cm, so the absolute error was still quite small. Also, some discrepancies were attributed to schematization differences.

Although some discrepancies were found the overall performance of TRITON was considered fairly good. TRITON was therefore considered technically capable for the purpose of modelling primary waves in port applications.

Some practical issues that were encountered with the TRITON model were instabilities of the breaker model, boundary instabilities and excessive computational times. Van der Wel (2011) and

Van der Ven (2012) investigated the use of TRITON as a part of a model chain to compute the dynamics of moored vessels in ports. Their experiences with this model are largely the same.

3.4 SWASH

3.4.1 Introduction

SWASH (which is an acronym for Simulating WAVes till SHore) is a non-hydrostatic wave-flow model developed at Delft University of Technology. The model is developed to predict the transformation of waves which propagate from offshore towards the shore (or into a harbour of course). The model accounts for the following wave processes (this is a selection of the models features listed in (The SWASH Team (Delft University of Technology) 2014)):

- Shoaling
- Refraction
- Diffraction
- Dispersion
- Nonlinear wave-wave interactions (including surf beat and triads)
- Wave breaking
- Wave runup and rundown
- Partial reflection and transmission
- Wave-current interaction
- Wave-induced currents
- Wave damping induced by aquatic vegetation

For this thesis version 2.0 of the SWASH software package was used. The SWASH software is open source and is freely available at the SWASH website.

3.4.2 Modelling background

Equations and assumptions

SWASH is based on the nonlinear shallow water equations including non-hydrostatic pressure. These equations are derived from the Navier-Stokes equations for incompressible flow, which read:

$$\rho \left(\frac{\partial u_i}{\partial t} + \frac{\partial u_i u_j}{\partial x_j} \right) = - \frac{\partial p}{\partial x_i} + \eta \frac{\partial^2 u_i}{\partial x_j^2} + k_i \quad (26)$$

with	t	time
	x	coordinates
	u	velocity components
	p	pressure
	k	other body forces such as gravity
	ρ	density
	η	molecular viscosity

And the continuity equation for incompressible flow with a constant density:

$$\frac{\partial u_j}{\partial x_j} = 0 \quad (27)$$

The Navier-Stokes equations are obtained from the conservation of momentum of the fluid, while the continuity equation follows from the conservation of fluid mass.

In order to describe only the mean flow, without all the small scale turbulence, the Navier-Stokes equations must be time averaged. This is done by first decomposing the velocities and pressures in a mean (indicated with an overbar) and a fluctuating part (indicated with a prime), and yields the so called Reynolds-Averaged Navier-Stokes (RANS) equations:

$$\rho \left(\frac{\partial \bar{u}_i}{\partial t} + \frac{\partial \bar{u}_i \bar{u}_j}{\partial x_j} + \frac{\partial \overline{u_i' u_j'}}{\partial x_j} \right) = - \frac{\partial \bar{p}}{\partial x_i} + \eta \frac{\partial^2 \bar{u}_i}{\partial x_j^2} + \bar{k}_i \quad (28)$$

Notice the extra terms, $\rho \frac{\partial \overline{u_i' u_j'}}{\partial x_j}$, that are now in the equations. These terms are called the

Reynolds or turbulent stresses and take into account the effect of turbulence on the mean flow. The terms can be approximated with various turbulence closure models. In SWASH it is solved using the Boussinesq hypothesis (i.e., the eddy viscosity concept, expressing the viscosity in terms of characteristic length and velocity scales).

The governing equations in SWASH are obtained from integrating the continuity equation and the RANS equations in vertical direction, for each vertical layer. When integrated over the entire water depth, the equations become (Zijlema, Stelling and Smit 2011):

$$\begin{aligned} \frac{\partial \zeta}{\partial t} + \frac{\partial hu}{\partial x} + \frac{\partial hv}{\partial y} &= 0 \\ \frac{\partial u}{\partial t} + u \frac{\partial u}{\partial x} + v \frac{\partial u}{\partial y} + g \frac{\partial \zeta}{\partial x} + \frac{1}{h} \int_{-d}^{\zeta} \frac{\partial q}{\partial x} dz + c_f \frac{u \sqrt{u^2 + v^2}}{h} &= \frac{1}{h} \left(\frac{\partial h \tau_{xx}}{\partial x} + \frac{\partial h \tau_{xy}}{\partial y} \right) \\ \frac{\partial v}{\partial t} + u \frac{\partial v}{\partial x} + v \frac{\partial v}{\partial y} + g \frac{\partial \zeta}{\partial y} + \frac{1}{h} \int_{-d}^{\zeta} \frac{\partial q}{\partial y} dz + c_f \frac{v \sqrt{u^2 + v^2}}{h} &= \frac{1}{h} \left(\frac{\partial h \tau_{yx}}{\partial x} + \frac{\partial h \tau_{yy}}{\partial y} \right) \end{aligned} \quad (29)$$

with	x, y	horizontal coordinates
	z	vertical coordinate, with origin at still water level and pointing upwards
	ζ	surface elevation, measured upwards from still water level
	d	bottom level, measured downwards from still water level
	h	water depth, given by $h = \zeta + d$
	u, v	depth averaged flow velocities in x and y directions
	q	non-hydrostatic pressure (normalised by the density), defined by $p = g(\zeta - z) + q$
	τ_{ij}	horizontal turbulent stresses
	g	gravitational acceleration
	c_f	dimensionless bottom friction coefficient

These equations differ from the standard shallow water equations (6) through the terms containing the non-hydrostatic pressure, which enables the modelling of frequency dispersion. Notice also that the viscous stresses are neglected in the equations (29), since they are orders of magnitude smaller than the turbulent stresses.

The surface elevation, $\zeta(x, y, t)$ in equations (29), is described in SWASH as a function of the horizontal coordinates (and time). A consequence of this approach is that overturning waves cannot be simulated. This is however not considered to be a severe limitation for modelling wave penetration in harbours. Simulation of overturning waves requires many vertical grid cells and is very computationally expensive, while the additional level of detail obtained is generally not considered to be necessary for coastal engineering applications.

In SWASH breaking waves are treated as discontinuities in the flow where mass and momentum conservation still applies. The amount of energy dissipation by turbulence in the broken wave is accounted for through an analogy with hydraulic jumps. For details on this and other wave breaking approximations reference is made to (Smit, Zijlema and Stelling 2013).

Numerical aspects

Grid

The partial differential equations in SWASH are discretised on a staggered grid, which can be either rectangular or curvilinear. In the vertical direction the domain is discretised in a number of terrain following layers. The non-hydrostatic pressure is computed at the faces of the vertical layers, so the pressure at the free surface can be imposed easily and accurately.

Schemes

SWASH is based on an explicit, second order finite difference method to integrate the governing equations. Mass and momentum are conserved locally (i.e. for each element) and globally with this approach. For advection terms in the equations multiple schemes are available within SWASH, details are given in (Zijlema, Stelling and Smit 2011), (Stelling and Duinmeijer 2003), and (Zijlema and Stelling 2008).

The pressure in equations (29) is decomposed in a hydrostatic and dynamic part. The dynamic part is solved implicitly in a several steps, see (Zijlema and Stelling 2005). First an estimation of the velocity field is computed based on an estimation of the dynamic pressure. In the next step a Poisson-type equation is obtained for the dynamic pressure by combining the continuity and momentum equations. This Poisson-type equation is solved iteratively, yielding the corrected dynamic pressure. The final flow field can then be obtained based on the corrected non-hydrostatic pressure.

In SWASH the vertical gradient of the non-hydrostatic pressure is approximated with a method based on the Keller-box scheme (Stelling and Zijlema 2003). This scheme enables accurate frequency dispersion with only two (for $kh < 3$) or three (for $kh < 16$) vertical layers.

CFL condition

SWASH is based on an explicit scheme and therefore requires certain restrictions on the time step to obtain numerical stability. The CFL condition (which ensures that the numerical domain of dependence includes the analytical domain of dependence) for 2D problems in SWASH is given by (The SWASH Team (Delft University of Technology) 2014):

$$Cr = \Delta t \left(\sqrt{gd} + \sqrt{u^2 + v^2} \right) \sqrt{\frac{1}{\Delta x^2} + \frac{1}{\Delta y^2}} \leq 1 \quad (30)$$

with c_r Courant number
 Δt time step
 $\Delta x, \Delta y$ grid size in x- and y-direction
 u, v velocity components in x- and y-direction
 d depth

The time step that is used for the time integration is controlled by a user defined range of Courant numbers. The default range of Courant numbers is 0.4 till 0.8, but for wave interaction with complex structures (for instance breakwaters and quay walls) a maximum Courant number of 0.5 is advised.

Parallelization

Computational times of SWASH simulations can be reduced by using more cores or processors simultaneously. The SWASH code is parallelized by decomposing the computational domain and using Message Passing Interface (MPI). The parallel performance was tested in (Zijlema, Stelling and Smit 2011), where super linear scaling was obtained up to 12 cores for the cases considered.

Boundary conditions

Land boundaries in SWASH do not need to be specified explicitly but result from the bathymetry in combination with the current water surface. Structures (such as breakwaters but also quay walls) can be defined on top of the bottom profile. The porosity, stone size and height of a structure can be defined. These properties control (together with some physical parameters) the amount of wave reflection, transmission and dissipation that occurs. For more information on the modelling of porous structures with SWASH reference is made to (Mellink 2012).

At the open boundaries incoming waves can be specified by means of wave spectra, time series or wave height and period (in case of monochromatic waves). To minimize reflection on such an open boundary a radiation condition can be imposed.

Sponge layers can be applied to create boundaries where waves propagate out of the computational domain with minimal (artificial) reflection (Stelling and Zijlema 2003). Sponge layers absorb the wave energy and need a width of about 3 to 5 wavelengths to be effective (The SWASH Team (Delft University of Technology) 2014).

Post processing

SWASH offers a large list of output quantities and various options to define output locations. Visualisation of the results and spectral analysis of time series, however, have to be done with other software.

3.4.3 Earlier validation studies and benchmark results

Benchmark results of SWASH

A large number of benchmark test cases have been carried out with SWASH, and the results have been published. A list of examples of test cases can be found on the SWASH website (swash.sourceforge.net).

The Berkhoff shoal test case (Berkhoff, Booij and Radder 1982) was (amongst other test cases) considered in (Zijlema and Stelling 2008). The results from SWASH were compared to the original measurements and to the results from a Boussinesq-type wave model (Funwave 2.0). It was concluded that both models are able to predict the diffraction and refraction of waves and that the computational efficiency of both models is comparable.

In (Zijlema, Stelling and Smit 2011) the results of eleven more test cases are presented. It was concluded that SWASH is capable of simulating “complex nearshore wave processes, including wave breaking, nonlinear interaction, wave runup and wave-induced circulation”.

3.5 Conclusions

The underlying equations, schematisations and numerical implementations in PHAROS, TRITON and SWASH are summarised. This partly answers the second research sub-question. The most fundamental difference in model equations is that PHAROS is linear while TRITON and SWASH are nonlinear. Essential differences in schematisations and implementations are found primarily in boundary conditions. The consequences of these differences for modelling wave penetration in ports are further analysed in the next chapter.

A review of literature on the performance of the considered models indicates they should all be able to accurately simulate wave processes that are relevant for primary wave penetration in ports. To affirm this conclusion and gain insight in the sensitivity towards certain modelling parameters, additional benchmark tests are carried out with PHAROS, TRITON and SWASH in the next chapter.

4 Comparison and analytical benchmark tests of selected models

4.1 Introduction

In the previous chapter PHAROS, TRITON and SWASH are described. It showed numerous differences in model equations, numerical implementations, and schematisations exist. This chapter focuses on the differences that are considered most relevant for modelling wave penetration in ports. Emphasis is therefore on the wave processes reflection, shoaling, and diffraction, as these are regarded as dominant for waves propagating in harbours.

First, the differences with regards to the schematisation of model boundaries are discussed. The influence of the different model equations and numerical implementations on the modelling of shoaling and diffraction are investigated next, based on calculations with the models. The influence of model settings is investigated as well to gain more insight and to support the choice of model settings for subsequent simulations. Lastly, the model's computational efficiencies are compared.

4.2 Model boundaries

4.2.1 Modelling concepts

With SWASH, (sloping) boundaries can be modelled as porous structures. At the location of a porous structure water levels are always computed, even if the height of the porous structure exceeds the water depth. The height, porosity, and stone diameter of porous structures need to be specified throughout the computational domain.

PHAROS and TRITON use a different approach when it comes to modelling boundaries compared to SWASH. In PHAROS and TRITON, a boundary marks the end of the computational domain. A reflection coefficient can be specified at such a boundary. Reflection coefficients in PHAROS are defined as the ratio between incoming and reflected wave height, while in TRITON they are defined as the ratio between incoming and reflected instantaneous surface elevation. These reflection coefficients can be estimated based on empirical relations, see Section 2.1.4 for an example.

A fundamental difference between these approaches is that with PHAROS and TRITON reflection coefficients must be imposed, while the amount of reflection of a porous structure in SWASH depends on the properties of the structure and the incident waves and is not predetermined.

The approach used by PHAROS and TRITON does not allow for a very realistic simulation of reflection on slopes, since in reality reflection coefficients will depend on the properties of the incident waves, and this dependence is not correctly accounted for when only a single reflection coefficient is specified at a boundary. When only linear monochromatic waves are considered this approach is fine since the reflection coefficient can then be chosen such that it includes the effects of the wave height, wavelength and the direction of the monochromatic wave.

4.2.2 Schematisations of slopes

PHAROS and TRITON require a minimal water depth to perform stable computations. This means a sloped boundary (e.g. a beach or a breakwater) will have to be schematised somehow. Figure 4.1 shows several possible schematisations.

Test simulations with PHAROS have shown that including a bathymetry in the schematisation, as in option B, C, D and E in Figure 4.1, will result in a larger reflected wave height. So apparently the

shoaling effect is stronger than the deshoaling effect. This should be taken into consideration when choosing a reflection coefficient.

When option B is chosen, which entails keeping the original bathymetry and placing the boundary at the minimal depth required by the model, the model's boundary will end up seaward of the original waterline. It can be expected that this will affect the model's eigenperiods. This schematisation is therefore not advisable, particularly when harbour oscillations are studied.

Which schematisation is most suitable depends on the model that is used and on whether the considered boundary is straight, convex, or concave.

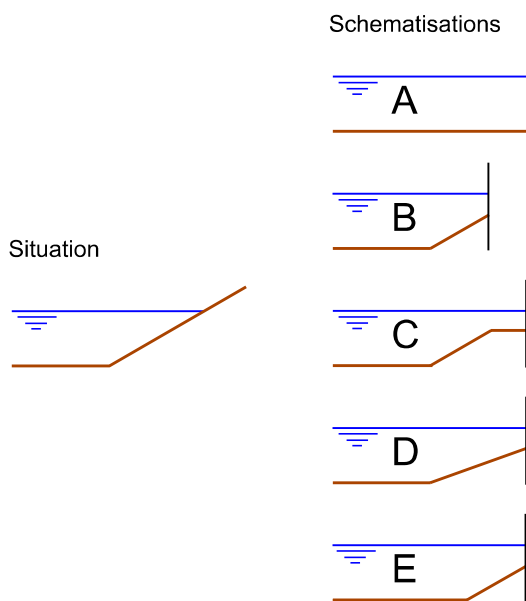


Figure 4.1 - Different ways of schematising a slope in PHAROS or TRITON, the black lines indicate the location of boundaries

Convex boundaries

When a boundary is straight or convex, and a linear model such as PHAROS is applied, the differences between schematisations A, C, D, or E are expected to be negligible. If any differences would be observed they could easily be compensated by tuning the reflection coefficient.

When a nonlinear model such as TRITON is applied, higher harmonics could be generated at the slope. It is therefore considered best to include the bathymetry as much as possible, by using schematisation C, D or E.

Concave boundaries

When a boundary is concave, e.g. the tip of a breakwater, refraction becomes important. It is then necessary to include the bathymetry as much as possible in order to get the direction of the simulated waves, and thereby the amount of wave energy in the shadow zone of the obstacle, right. The effect of incorporating a breakwater in the model's bathymetry is for instance demonstrated in (Boeyinga 2010).

Schematisations C and D are expected to yield the best results, for both PHAROS and TRITON, as the bathymetry in these cases is closest to the actual bathymetry.

4.3 Shoaling

4.3.1 Introduction

Shoaling is a wave process that can have a relatively large effect on wave propagation into harbours, which makes it an interesting topic to consider in this thesis. Unfortunately, it is not possible to study shoaling in the physical model tests where this thesis focuses on (since these physical models lack a bathymetry). Therefore a benchmark test case is introduced in this section, for which an analytical solution exists. This benchmark test case will be used to investigate linear shoaling performance and the influence of certain model settings hereupon.

Insight in the model's wave dispersion is obtained at the same time, since the process of linear shoaling is driven by wave dispersion. This insight will aid the choice of model settings for simulations described in the next chapters.

4.3.2 Methodology

Bathymetry

The bathymetries of the benchmark test cases considered in this chapter are very schematic and consist of an underwater slope connected to flat areas on both sides, see Figure 4.2. The underwater slope serves as a transition between the area of intermediate water depth where the waves enter the domain and the shallow water area where the waves leave the domain.

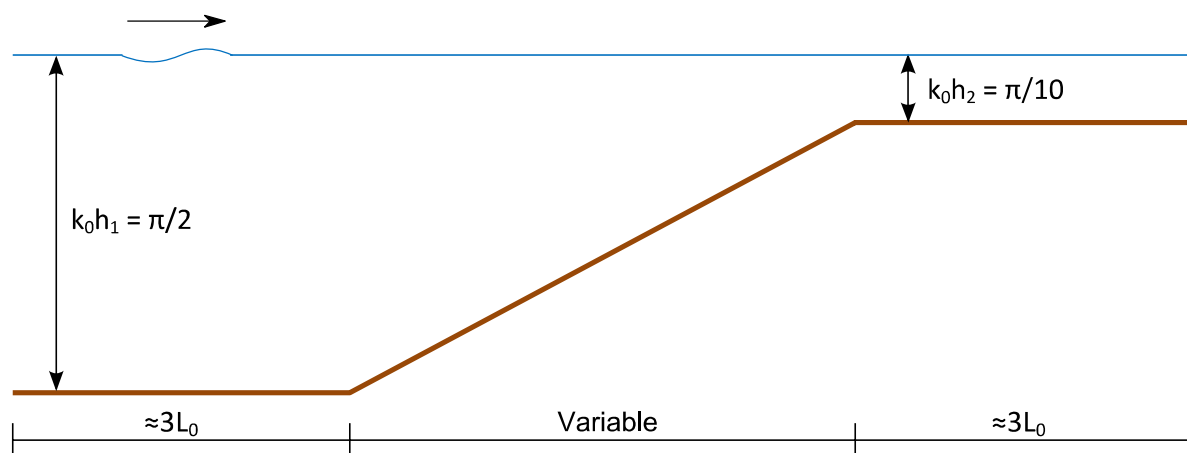


Figure 4.2 – Bathymetry for shoaling test case, several slopes were considered

The following four steepnesses are considered for the underwater slope in the linear shoaling case: 1:8, 1:15, 1:30 and 1:60. This enables a sensitivity analysis of the results regarding the steepness of the slope and gives insight in the accuracy of the applied post processing methods.

Boundary conditions

Monochromatic waves with small amplitude ($a/h < 0.01$) and low steepness ($H/L_0 < 0.001$) are imposed at the incident boundary of the model, left side of Figure 4.2, to study linear shoaling. At the right boundary in Figure 4.2 the waves propagate out of the domain with minimal (artificial) reflection.

Analytical solution for linear shoaling

An analytical solution for linear shoaling can be obtained from linear wave theory, under the assumption that the total flux of wave energy is constant in the entire domain. This assumption is valid if waves do not reflect against the underwater slope, which is approximately true when the underwater slope is not too steep. The shoaling coefficient can in that case be derived as follows:

$$\begin{aligned}
 P &= E_1 C_{g,1} = E_2 C_{g,2} \\
 \frac{1}{8} \rho g H_1^2 C_{g,1} &= \frac{1}{8} \rho g H_2^2 C_{g,2} \\
 K_s = H_2 / H_1 &= \sqrt{C_{g,1} / C_{g,2}} = \sqrt{\frac{c_1 n_1}{c_2 n_2}} = \sqrt{\frac{k_2}{k_1} \frac{1 + 2k_1 h_1 / \sinh 2k_1 h_1}{1 + 2k_2 h_2 / \sinh 2k_2 h_2}}
 \end{aligned} \tag{31}$$

- with
- K_s shoaling coefficient
 - H_1 wave height in the area of intermediate water depth
 - H_2 wave height in the shallow water area
 - E energy density
 - C_g wave group velocity
 - c wave celerity
 - P energy flux
 - k wave number
 - h water depth
 - ρ density
 - g acceleration due to gravity

The index 1 indicates wave properties in the area of intermediate water depth while index 2 is used for wave properties in the shallow water area.

Using the well-known linear dispersion relationship, a wave number can (iteratively) be calculated from a chosen wave period and water depth. The shoaling coefficient is then readily obtained from equation (31), see Figure 4.3 for the results.

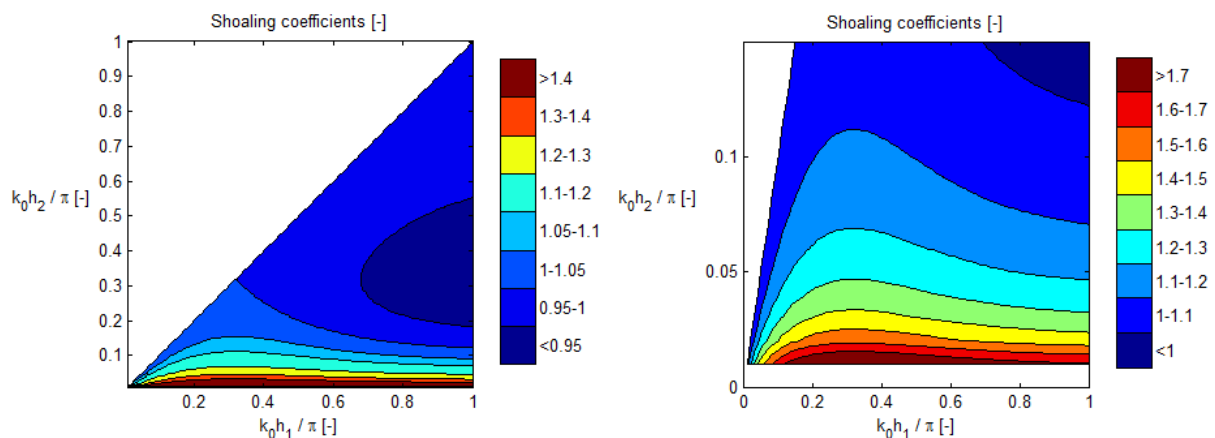


Figure 4.3 – Linear shoaling coefficients, the right graph contains a close-up off the area of interest

The chosen wave period and water depths are linked through the bathymetry in Figure 4.2, which is provided in terms of dimensionless parameters. If for instance a wave period of 10 seconds would be chosen, the intermediate water depth will be 39.033 m and the shallow water depth 7.807 m. The shoaling coefficient for the bathymetry in Figure 4.2 is $K_s = 1.0971$ for all considered cases.

Calculation of wave height of the shoaled waves

In case of PHAROS, wave heights in the entire 2DH domain are directly obtained. The wave heights in the shallow water area are averaged to obtain a single representative value of the wave height after shoaling. This averaging is done in an energy conserving manner (by computing the root mean square value as in equation (23)) over a square area with sides equal to twice the local wavelength.

A possible source of error is that the size of each (triangular) grid cell is not taken into account when calculating the average. The error this procedure produces is small since a couple thousands of grid cells are averaged and the grid cells are quite regular. This was verified by computing the incoming wave height with the same procedure, yielding values that are at most 0.1% off.

For the 1D or 2DV simulations with TRITON and SWASH, wave heights in the shallow area are obtained as follows:

1. Time series of water level elevations are obtained for each computational grid cell.
2. The first part of each time series is discarded to be sure model spin-up will not affect the results. The duration of this part is equal to or larger than twice the duration it takes a wave to propagate from one side of the computational domain to the other side.
3. From the remaining (approximately 100) waves in each time series a mean wave height is calculated with the aid of time domain analysis.
4. Over a length of one local wavelength (according to the linear dispersion relationship), the wave heights calculated in step 3 are averaged in the shallow water area. This spatial averaging is again done with equation (23), to make sure wave energy is conserved.

The shoaling coefficient is subsequently obtained by dividing the calculated wave height of the shoaled waves by the wave height of the imposed waves. The wave heights of the imposed waves are calculated from time series obtained in the deep water area. This is done in the exact same fashion as for the shoaled waves in shallow water, as described above.

PHAROS settings

The PHAROS 2DH simulations use the following settings:

- Grid resolution: 20 nodes per wavelength, for the shortest primary wave
- Width of computational domain: $\approx 3L_0$
- Lateral boundary conditions: 0% reflection (radiation condition)
- Boundary condition at the outgoing boundary of the model (right side in Figure 4.2): 0% reflection (radiation condition)
- No bottom friction

TRITON settings

The TRITON 2DH simulations use the following settings:

- Grid resolution: 40 grid cells per wavelength, for the shortest primary wave

- Width of computational domain: 2 grid cells
- Time steps per wave period: 100
- Lateral boundary conditions: closed, i.e. 100% reflection
- Boundary condition at the outgoing boundary of the model (right side in Figure 4.2): outflow (radiation condition)
- Dispersion parameter: $\alpha = 0.385$ (TRITON's default)
- Shoaling parameter: $\beta = 0.36$ (TRITON's default)
- No bottom friction

Boussinesq-type equations can be mathematically modified to obtain new sets of equations which are asymptotically equivalent but contain extra free parameters. The parameters α and β in TRITON are examples of such free parameters. The value of these parameters can be optimized for certain purposes, e.g. improving the modelling of linear shoaling. To investigate the influence and sensitivity of these parameters, additional TRITON runs are carried out that differ in the following:

- $\alpha = 0.4$ and $\beta = 0.34$ are used as dispersion and shoaling parameters. This should improve the approximation of linear shoaling for this specific case (Borsboom 1998).

SWASH settings

The SWASH 2DV simulations use the following settings:

- Grid resolution: 40 grid cells per wavelength, for the shortest primary wave
- Time steps per wave period: 200 (maximum Courant number of 0.5)
- Boundary condition at the outgoing boundary of the model (right side in Figure 4.2): sponge layer of approximately $5L_0$
- No bottom friction

To investigate the influence and sensitivity of certain numerical parameters, additional SWASH runs are carried out that differ in the following:

- The amount of vertical layers is varied. Runs are carried out with 1, 2, 3, 4, 5, 10 and 25 vertical layers.
- The numerical discretization of the vertical pressure gradient was set to central differencing (denoted "cd" in Figure 4.4) instead of the default Keller-box scheme.

4.3.3 Results

An overview of the resulting shoaling coefficients is presented in Figure 4.4. As expected, the shoaling coefficients show no correlation with the steepness of the underwater slope. The sensitivity towards the slope is small as well, indicating the method used to obtain shoaling coefficients is accurate.

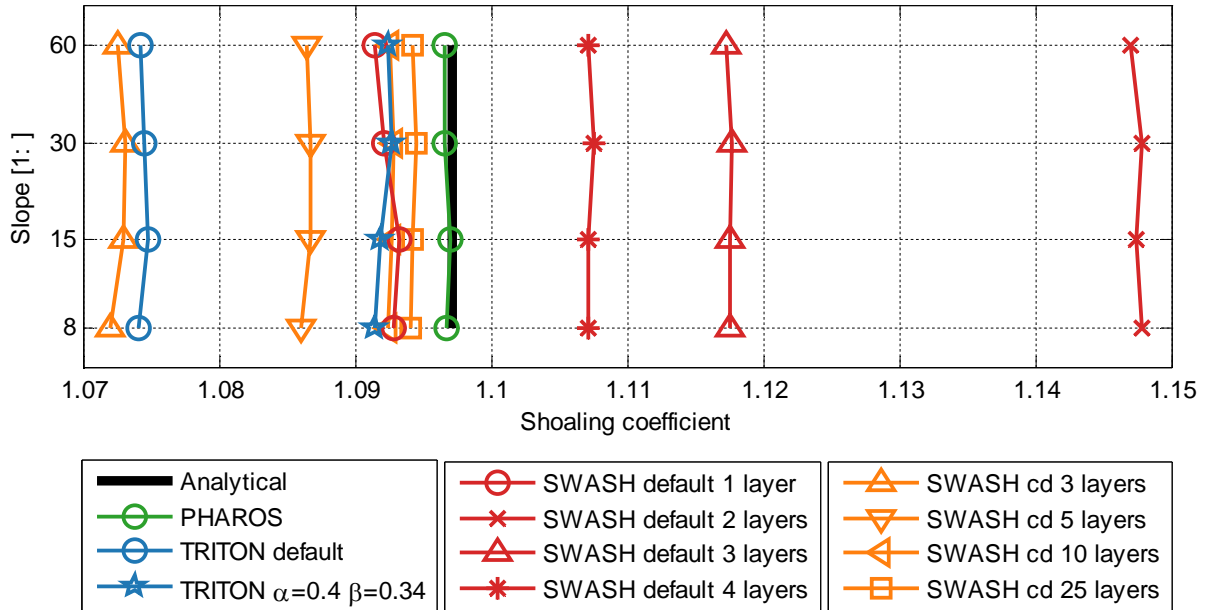


Figure 4.4 - Results from benchmark test case

PHAROS

The results presented in Figure 4.4 show that the linear shoaling performance of PHAROS is practically perfect. This could be expected since PHAROS is a linear model, based on the same assumptions about the vertical structure of the flow and thus the same dispersion equation as in linear wave theory.

The small deviations from the analytical shoaling coefficient might be due to the fact that the size of the grid cells was not taken into account during averaging of the wave height, as explained before.

TRITON

Using the default settings, TRITON underestimates the shoaled wave heights with approximately 2%. Figure 4.4 also shows how performance for this specific case can be improved by adjusting the dispersion parameter α and the shoaling parameter β .

Note however that optimizing the values of α and β for linear shoaling results in less optimal performance for nonlinear wave interactions, and therefore limits the model's application range. TRITON is designed to enable the modelling of nonlinear wave interactions as well, which is why the model's default values of α and β differ from those that are optimal for linear shoaling (Borsboom 1998).

SWASH

Using the default settings (which includes applying a combination of the Keller-box and implicit Euler scheme for the non-hydrostatic pressure gradient), SWASH results turn out to depend slightly on the number of vertical layers that is applied, see the red lines in Figure 4.4. When more than one layer is applied, the shoaling coefficient is overestimated with about 5% or less. The amount of overestimation decreases for increasing number of layers.

For simulations with up to 3 layers, an approximate dispersion relationship is employed. This approximate relation is different for simulations with a different number of layers, see (The SWASH

Team (Delft University of Technology) 2014). The accuracy of these approximate dispersion relations has been verified, and shoaling coefficients have been calculated using these approximate linear dispersion relations instead of the exact linear dispersion relation. The analytical shoaling coefficients based on the approximate dispersion relation are $K_s = 1.125$ in case of one layer and $K_s = 1.104$ in case of two layers. Clearly, the observed little overestimation of shoaling coefficients cannot entirely be attributed to the application of approximate dispersion relations.

When central differencing is applied to the non-hydrostatic pressure gradient instead of the default Keller-box scheme, results change for the test case considered here. The dependence of the accuracy of the computed shoaling coefficients on the amount of vertical layers is still similar, but this time the shoaling coefficients are slightly underestimated (see the orange lines in Figure 4.4). Note that when central differencing is applied, no approximate dispersion relations are employed.

A nonzero horizontal mean flow (for instance an artificial circulation) could theoretically explain the found shoaling coefficients. However, the time and layer averaged horizontal velocities in the computational domain are investigated and appear to be negligible (as expected).

4.3.4 Conclusion

All considered models have good performance for linear shoaling in this benchmark test. The linear wave model PHAROS performs exactly as expected from linear wave theory. The results from the nonlinear models TRITON and SWASH depend slightly on the applied settings but were always found to be within 5% of the analytical solution. This is not surprising considering these models are designed to simulate nonlinear waves and are therefore not optimised to compute linear shoaling as accurate as possible.

4.4 Diffraction

4.4.1 Introduction

Diffraction is a wave process that plays a part in the wave propagation in almost every port. It is especially relevant for ports sheltered by breakwaters. In this section the ability of PHAROS, TRITON and SWASH to reproduce this wave process is analysed by comparing the results from numerical simulations to an analytical solution.

4.4.2 Methodology

Layout

The layout considered in this section is that of the classic semi-infinite breakwater problem, see Figure 4.5 for a definition sketch. The water depth is uniform throughout the domain.

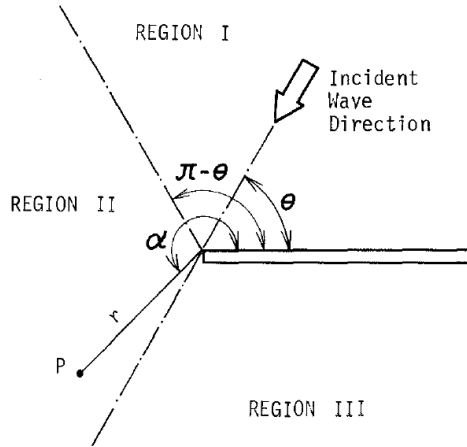


Figure 4.5 - Definition sketch for diffraction around a semi-infinite breakwater (Goda, Takayama and Suzuki 1978)

The numerical simulations are carried out for an intermediate water depth ($kh \approx 1.2$). The model domains have a width of 20 wavelengths and a length of 25 wavelengths. The breakwater is fully reflective, 10 wavelengths long, and is located at a distance of 5 wavelengths from the boundary with incident waves.

Boundary conditions

Monochromatic waves with a small amplitude, low steepness, and a direction of $\theta=270$ degrees (with θ defined as in Figure 4.5) are imposed at the southern boundary (bottom of Figure 4.5). The boundary at the opposite side of the breakwater, the left side of Figure 4.5, is modelled as closed to prevent energy loss through this boundary. At all other boundaries, i.e. the top side and right side of Figure 4.5, the waves propagate out of the domain freely.

The breakwater itself is modelled as a thin vertical wall, reflecting all incoming wave energy.

Analytical solution

An analytical solution to this diffraction problem is elaborated in (Sommerfeld 1896). The solution as formulated by Goda et al. (1978) is provided below.

$$\begin{aligned}
 F_d(r, \alpha, f, \theta) &= F_{id}(r, \alpha, f, \theta) + F_{rd}(r, \alpha, f, \theta) \\
 F_{id} &= \frac{1}{\sqrt{2}} \exp \left[i \left\{ kr \cos(\alpha - \theta) + \frac{\pi}{4} \right\} \right] \times \left[\left\{ C(\gamma_1) + \frac{1}{2} \right\} - i \left\{ S(\gamma_1) + \frac{1}{2} \right\} \right] \\
 F_{rd} &= \frac{1}{\sqrt{2}} \exp \left[i \left\{ kr \cos(\alpha + \theta) + \frac{\pi}{4} \right\} \right] \times \left[\left\{ C(\gamma_2) + \frac{1}{2} \right\} - i \left\{ S(\gamma_2) + \frac{1}{2} \right\} \right]
 \end{aligned} \tag{32}$$

where,

$$\begin{aligned}
\gamma_1 &= \sqrt{\frac{4kr}{\pi}} \cos \frac{\alpha - \theta}{2} \\
\gamma_2 &= \sqrt{\frac{4kr}{\pi}} \cos \frac{\alpha + \theta}{2} \\
C(\gamma) &= \int_0^\gamma \cos\left(\frac{\pi}{2} \chi^2 d\chi\right) \\
S(\gamma) &= \int_0^\gamma \sin\left(\frac{\pi}{2} \chi^2 d\chi\right)
\end{aligned}
\tag{33}$$

with F the dimensionless complex wave amplitude
 r the distance from the tip of the breakwater
 α the angle from the tip of the breakwater, as defined in Figure 4.5
 f the frequency of the incident wave
 θ the direction of the incident wave, as defined in Figure 4.5
 k the wavenumber of the incident wave

The subscript id indicates incident waves and associated scattered waves while subscript rd is used to indicate waves that are reflected from the breakwater and their associated scattered waves. Figure 4.6 contains a plot of this analytical solution.

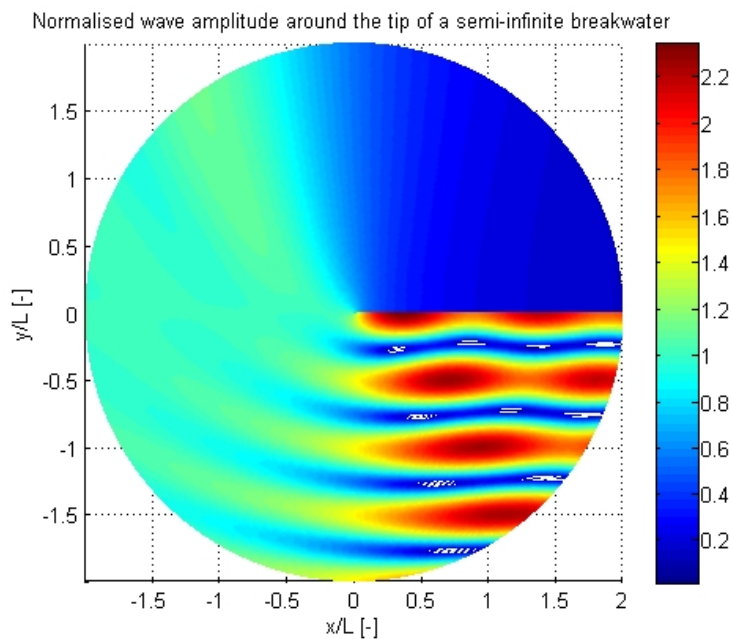


Figure 4.6 - Sommerfeld solution for wave diffraction around a semi-infinite fully reflective breakwater, for $\theta=270^\circ$

The analytical solution is scaled such that the wavelengths in the analytical solution match the wavelengths in the numerical simulations. Since the water depth in the numerical simulations is intermediate instead of infinite, these wavelengths are computed from the linear dispersion relationship.

Calculation of normalised wave heights

The diffracted wave heights are normalised with incoming wave heights. The incoming wave heights are taken equal to those specified on the model's incoming boundary.

For TRITON simulations, the diffracted wave heights are obtained through a time domain analysis of computed water surface elevations, for all grid cells in the model's domain. For SWASH simulations, the wave heights computed by the model itself are used, again for each grid cell in the model's domain. These wave heights are computed based on the variance of the water surface elevation. With PHAROS, wave heights are of course directly available from the model's output as well.

PHAROS settings

The PHAROS simulations use the following settings:

- Grid resolution: 20 nodes per wavelength
- Boundary condition at the left side of Figure 4.5: 0% reflection (radiation condition)
- Boundary condition at the right and top side of Figure 4.5: reflection-2 boundary condition with 0% reflection (second order Higdon boundary condition). The boundaries are divided in segments with a length of 5 wavelengths, and an angle of wave incidence is specified for each segment separately.
- Boundary conditions for breakwater: 100% reflection
- No bottom friction

TRITON settings

The TRITON simulations use the following settings:

- Grid resolution: 25 nodes per wavelength
- Boundary condition at the left side of Figure 4.5: closed
- Boundary condition at the right and top side of Figure 4.5: 0% reflection (radiation condition)
- Boundary conditions for breakwater: closed
- No bottom friction

SWASH settings

The SWASH simulations use the following settings:

- Grid resolution: 25 nodes per wavelength
- Number of vertical layers: 2
- Boundary condition at the left side of Figure 4.5: closed
- Boundary condition at the right and top side of Figure 4.5: sponge layers with a width of 5 wavelengths.
- Breakwater modelled as porous structure with a height of 4 times the water depth, a porosity of 0.1% and a stone size of 0.1 mm.
- No bottom friction

4.4.3 Results

The simulation results are shown in Figure 4.7, together with the analytical solution described in the previous section. Qualitatively, the model results look very similar to the analytical solution. It can be noticed however that the analytical solution is the smoothest. The results from the numerical

simulations contain some extra wiggles, probably caused by spurious reflections on the model boundaries.

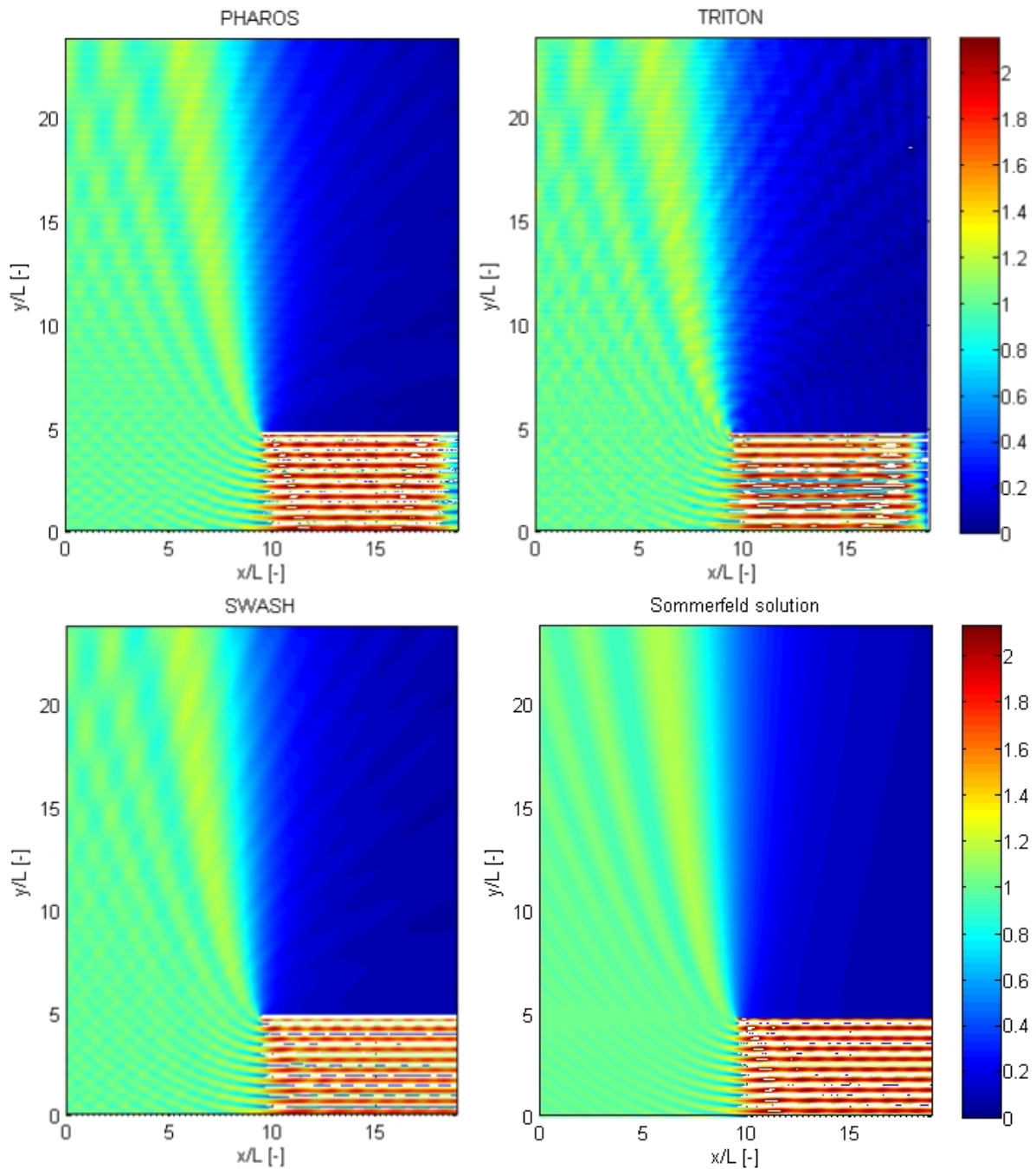


Figure 4.7 – Simulation results for the semi-infinite breakwater case

To enable a more quantitative comparison, transects are plotted in Figure 4.8. From these graphs it becomes clear that while the wave heights outside the shadow zone are not always very accurate, the wave heights in the shadow zone of the breakwater correspond quite well.

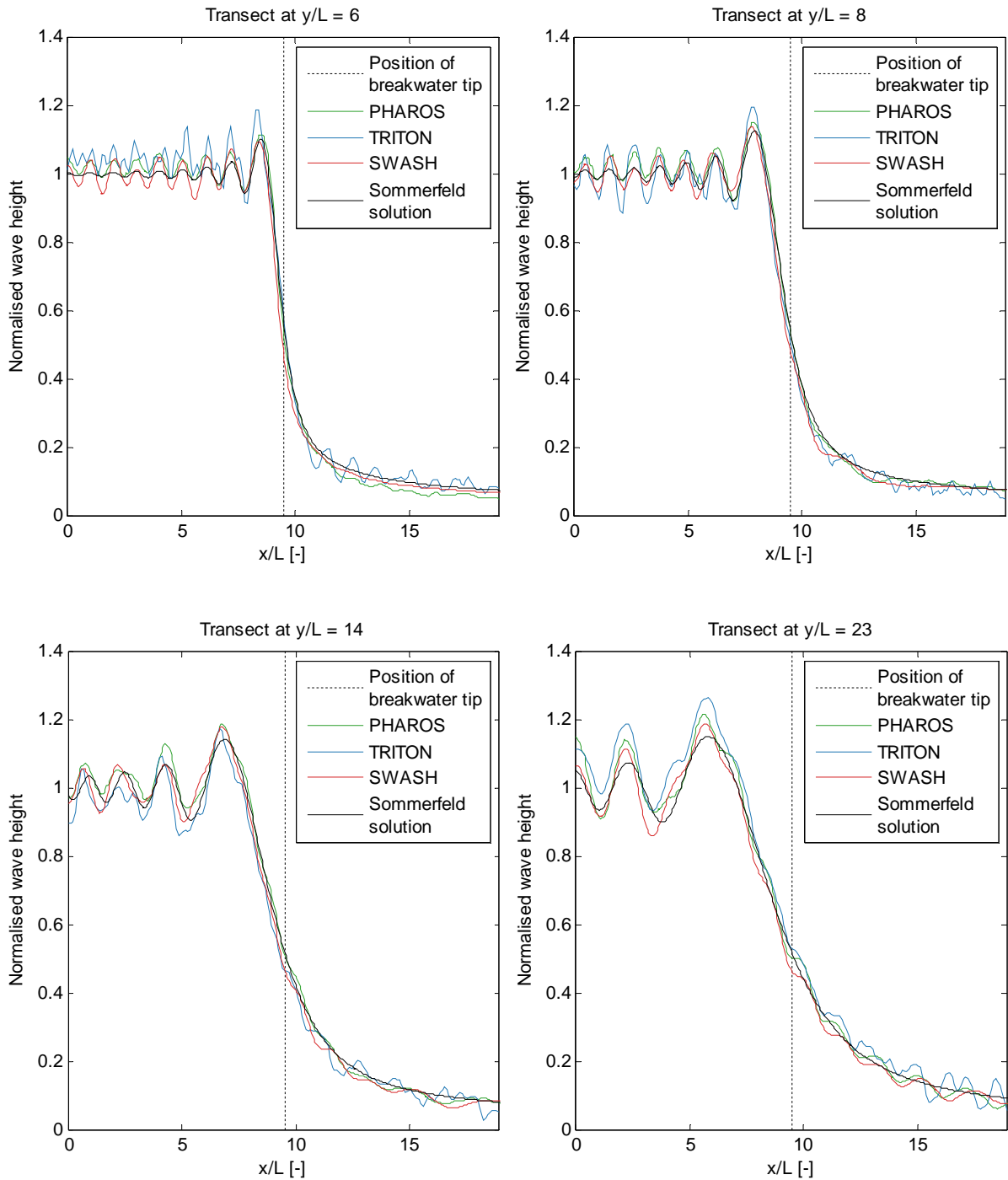


Figure 4.8 – Transects

4.4.4 Conclusion

The three considered models PHAROS, TRITON, and SWASH are all to be able to reproduce the diffraction pattern around a semi-infinite breakwater. Some slight deviations from the analytical solution were found but these could also be caused by imperfect radiation boundaries or other schematisation differences.

4.5 Computational efficiency

The performance of PHAROS, TRITON and SWASH in terms of computational efficiency varies significantly. To illustrate this, some statistics of the simulation of experiment T014 (which is described in later chapters) are included in Table 4.1. This shows that PHAROS is an order of magnitude faster than TRITON and SWASH when wave spectra are simulated. Since PHAROS computations are carried out in the frequency domain, it is another order of magnitude faster when monochromatic waves are simulated.

Table 4.1 - Computational efficiency, based on simulations of test T014

	PHAROS	TRITON	SWASH
Resolution of computational grid	7.2 cm	7 cm	7 cm
Total amount of computational cells	129,368	142,625	252,382
Number of vertical layers	1	1	2
Simulation time [s]	-	1791	1791
Time step [s]	-	0.035	0.01
Total number of time steps	-	51,171	179,100
Computed wave components	22	-	-
CPU threads	1	1	8
Total computational time [hours]	0.6*	179.3*	25.4*
Total computational cost [CPU threads * computational hours]	0.6*	179.3*	203.2*
Total computational cost (in CPU threads * computational seconds) per time step per grid cell	-	$8.8 \cdot 10^{-5}$	$1.6 \cdot 10^{-5}$
Total computational cost (in CPU threads * computational seconds) per time step per grid cell per layer	-	$8.8 \cdot 10^{-5}$	$8.1 \cdot 10^{-6}$
Total computational cost (in CPU threads * computational seconds) per grid cell	0.017	4.5	2.9
Total computational cost (in CPU threads * computational seconds) per grid cell per wave component	$7.6 \cdot 10^{-4}$	-	-

* Simulations with TRITON and SWASH are carried out on an Intel i7-2600 @ 3.4GHz. PHAROS simulations are carried out on an Intel Xeon E5-2670 0 @ 2.6GHz. All computations are performed on 64-bit Windows machines.

The computational cost per time step per grid cell is lower for SWASH than for TRITON, for the simulation considered in Table 4.1. The SWASH simulation contains more computational grid cells even though the grid resolution is the same because the entire wave basin was simulated with SWASH (including the area behind the port, which was not modelled with PHAROS and TRITON).

More aspects should however be considered when computational efficiency is discussed.

First of all the time step restrictions for SWASH and TRITON are different because these models use different time integration schemes. Maximum Courant numbers in TRITON can be about 3 times larger than the maximum Courant numbers in SWASH (due to the 4 stage Runge-Kutta scheme that is applied in TRITON, which actually solves a system of equations four times per time step).

Time steps are however not only limited by stability criteria, but by accuracy criteria as well. A

minimum of 20 time steps per wave period is advised for accuracy reasons. This can be restrictive for the high frequency part of the spectrum.

Another difference is that SWASH, contrary to TRITON, can be run on multiple computational cores simultaneously. This greatly reduces the computational time of a simulation. The computational efficiency of SWASH is depending on the number of cores as well. The SWASH simulation considered in Table 4.1 was run on 8 threads in parallel on a quad core CPU (using hyper-threading technology).

4.6 Conclusions

It has been shown that PHAROS, TRITON and SWASH are capable of accurately modelling linear shoaling and diffraction. Based on Chapter 2, good performance in modelling these wave processes is considered indispensable for modelling wave penetration in ports.

From a discussion on the schematisations of slopes it can be concluded that these are most realistically represented in SWASH. The actual accuracy with which the interaction of waves with slopes is modelled has not been assessed as this would require physical model data.

From a comparison on computational efficiency it can be concluded that PHAROS is at least an order of magnitude faster than TRITON and SWASH. SWASH is more efficient than TRITON and especially the parallelisation of its code is considered a large benefit for practical usability. These conclusions on computational efficiency will be incorporated in the evaluation of application boundaries.

The main differences between PHAROS, TRITON and SWASH, which are of importance for wave modelling in ports, are treated. The second research sub question is thereby answered.

Further analyses of the performance of numerical wave models for wave penetration in harbours in this report are made with the use of a physical model. Because this physical model has a flat bottom, shoaling will not be revisited and the results from the shoaling analysis in this chapter are guiding. Diffraction and reflection are difficult to separate in a real port, since the two processes always act simultaneously. The model accuracies for pure diffraction, as analysed in this chapter, therefore aid the analyses of the simulations of the physical model.

5 The physical model

5.1 Introduction

Numerical wave models have been validated numerous times, but usually not specifically for wave penetration in harbours or not with dedicated systematic scale model tests to determine application boundaries.

Academic test cases, which focus on a certain wave process, are typically used in literature to benchmark the performance of wave models. The solutions to these test cases are either analytical or obtained from physical modelling. The benchmark tests for shoaling and diffraction in the previous chapter are examples of test cases for which analytical solutions exist. More test cases that are relevant for wave penetration in harbours can be found in (Demirbilek, Zundel and Panchang 2010). For wave penetration in harbours multiple wave processes are generally important, and there is a desire to have dedicated test cases for that.

Validation of operational wave models for wave penetration in harbours is usually done with the aid of already available measurements. These measurements are obtained in real harbours, or from scale models of (existing) harbours.

These measurements were usually carried out in the context of a certain port design projects, for instance to test a new breakwater design. These measurements are generally not very suitable to determine application boundaries of numerical models from as they were not intended to be used for that purpose. The collected data can for instance be too inaccurate or not publicly available.

The project "Benchmark tests for Harbour models" (Deltares 2014) has the goal to produce a benchmark test dataset that can be used to validate numerical models for wave penetration in harbours. Within the framework of this project, systematic physical model tests have been carried out at Deltares' facilities in Delft.

This chapter describes the design and execution of the physical model tests. The focus is on the aspects that are relevant for the experiments that are numerically simulated in this thesis, but other conducted experiments and considerations are presented here as well. A list of all 57 wave conditions can be found in Appendix D.

5.2 Aims of the physical modelling

The goal of the physical modelling is to produce a benchmark test dataset which can be used to study the performance of operational numerical models for wave propagation in ports. Being able to study the different processes that influence wave propagation in ports separately would provide the best insight, this ability is therefore pursued as well.

Studying all relevant wave processes individually from scale models would require many different setups, and is therefore not practical. Besides that, the performance for various relevant wave processes can also be investigated using specific benchmarks for which analytical solutions exist, as was done in Chapter 4. Moreover, real waves propagating into harbours are always subject to several wave processes simultaneously. Some experiments will therefore focus on realistic scenarios, i.e. including many wave processes. Since it is impossible to find analytical solutions for such problems, physical modelling is necessary.

Studying harbour oscillations from analytical solutions only, is regarded as insufficient as well. Analytical solutions are only available for rather academic cases and harbour oscillations are very important to port operations. The physical model is therefore designed to provide good benchmark data for this process as well.

An overview of relevant wave processes and their presence in the most realistic experiments is given in Table 5.1. It is also indicated which wave processes can be reasonably studied individually from analytical benchmark cases and which can be individually studied from the scale model.

Table 5.1 - Wave processes present in physical model

Wave process	Relevant in harbour domains?	Present in scale model?	Can be individually studied from the scale model?	Analytical solution available for this specific wave process?
Shoaling	Yes	No	No	Yes, for linear case
Diffraction	Yes	Yes	No	Yes, for linear case
Refraction	Yes	Yes	No	Yes, for linear case
Reflection	Yes	Yes	No	No
Harbour oscillations	Yes	Yes	Yes	Yes, for academic geometries
Nonlinear interactions	Slightly	Yes	No	No
Breaking	Slightly	Yes	No	No
Transmission	Yes	Probably	No	No
Overtopping	Yes	No	No	No

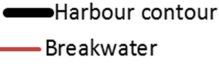
5.3 Model design

5.3.1 Layouts

The model represents a rather schematised, fictitious, port. The geometry of this port is considered to be representative for typical seaports. The schematisations facilitate the reconstruction of the physical model in numerical models.

The modelled port consists of a main basin, a closable side basin and an optional breakwater. This gives the option of having effectively three different port layouts, as is illustrated in Table 5.2. The complexity of the scale model can thus be increased in steps. The amount of relevant physical processes is consequently increased stepwise as well, as is summarised in Table 5.2.

Table 5.2 – The three layouts of the physical model and the relevant physics for each of them

(Landward side)  (Seaward side)	Layout 1	Layout 2	Layout 3
Governing wave processes	Reflection Harbour oscillations	Reflection Diffraction Harbour oscillations	Reflection Diffraction Refraction Transmission Harbour oscillations
Eigenmodes	Trivial	Less trivial	Many, increased complexity

The first layout is the most simple one in this context and can serve for calibration (of reflection coefficients for instance) purposes. In the second layout diffraction is more prominent and less trivial eigenmodes are introduced. The third layout is the most complete, featuring a realistic breakwater. This introduces additional wave processes such as refraction and transmission. The eigenmodes for this layout will be even more complex, and the harbour oscillations are likely more pronounced since the breakwater limits the amount of energy that is radiated out of the port.

The side basin is connected to the main basin under an angle of 45 degrees, deliberately resulting in “diagonal” quay walls. Only having straight and perpendicular boundaries would oversimplify a benchmark for operational numerical models. No bathymetry (e.g. foreshore) is included because this would be too costly.

5.3.2 Measurement locations

Wave heights are measured at the 27 locations displayed in Figure 5.1. At five of these locations, denoted with squares in Figure 5.1, x and y velocities are measured as well.

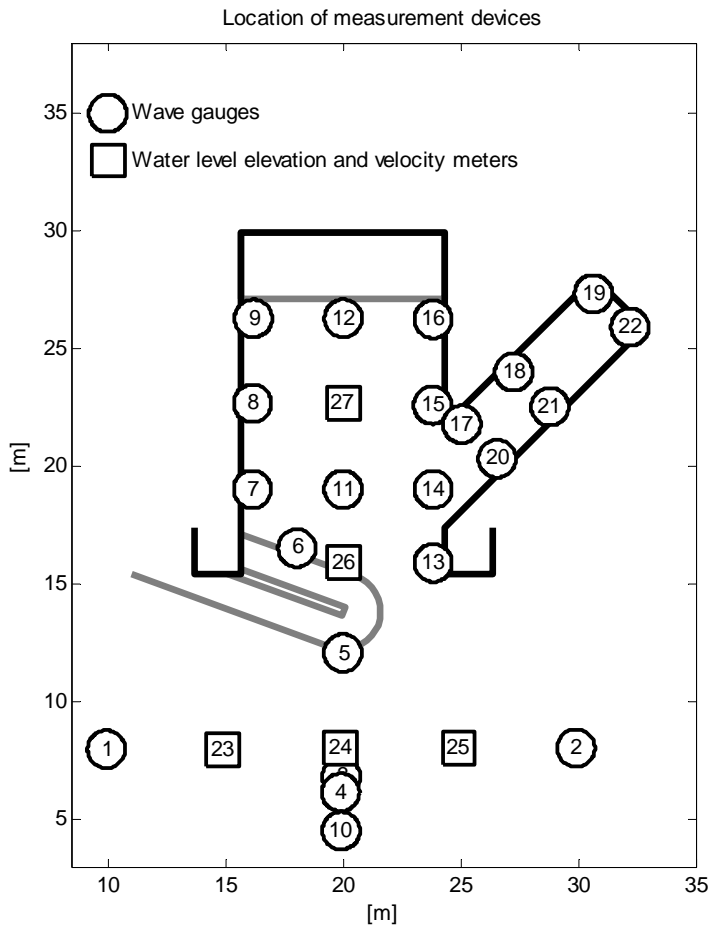


Figure 5.1 - Measurement setup (wave gauge 3 is located between 4 and 24)

Most of the wave height meters are placed near the quay walls. Wave heights at these locations are obviously interesting for port operations since vessels are being (un)loaded there. These locations are also very suitable for measuring harbour oscillations, as these standing waves will always have anti-nodes near closed boundaries.

In front of the harbour an array of measurement devices is placed to measure the incoming waves. The incoming waves can be computed from the combination of water level and velocity measurements using wave splitting techniques.

Measurement devices are also placed in the middle of the harbour basin and around the breakwater. This gives a more complete image of the wave field in the harbour.

5.3.3 Model scale and position of the model in the wave basin

Measurement accuracy

To enable accurate wave height and direction measurements, wave heights should be around 5 cm or more. In case the incoming wave climates are described by spectra, the spectral wave height should be at least 10 cm to ensure a good quality wave spectrum.

These requirements put a constraint on the scale that can be used. This constrain is the most restrictive for linear waves, which must have relatively low wave heights to avoid nonlinear effects.

Oblique waves

When waves are generated by the wave board with a direction non-perpendicular to the waveboard, there will not be a clear line separating the areas with and without the generated waves. Diffraction effects will cause some wave energy “leakage” in a direction perpendicular to the wave propagation direction, towards the area where no waves were generated.

Due to this wave energy “leakage”, the range of possible wave directions towards the port entrance does not simply follow from the locations of the port entrance and the tips of the wave board, but is somewhat narrower. A rule of thumb states that the wave energy “leakage” effect is sufficiently accounted for when a margin of 15 degrees is taken. This rule has been applied and is illustrated in Figure 5.2. The solid diagonal line indicates the maximum wave angle that can be realised without using the basins side walls to reflect the incoming waves. This maximum wave angle (nautical definition) is plus or minus 27.5 degrees. The dashed diagonal lines differ by 15 degrees. Note that the drawn wave ray does not originate from the tip of the wave board but at some distance from it. This is due to the fact that outermost pistons in the wave board are not fully used.

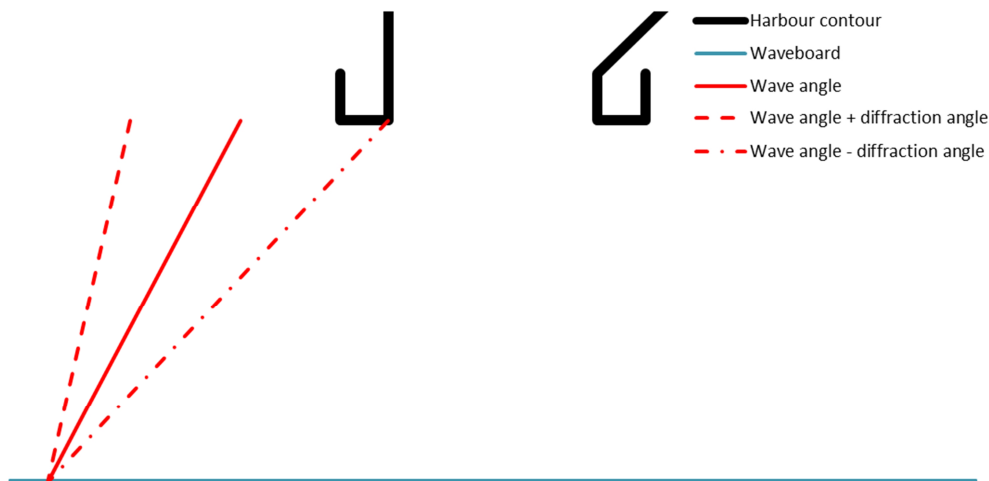


Figure 5.2 - Wave directions

In case of wave fields with a directional distribution, part of the wave energy may not reach the harbour entrance. Consider for instance a wave field with a mean direction perpendicular to the wave board and a $\cos^m(\theta)$ distribution with $m=15$ (which has a one-sided directional width of 14.2 degrees). Figure 5.3 shows how 95% of the energy in this wave field (the amount between the dashed lines) is able to penetrate into the port, which is considered sufficient to have a good representation of wave energy inside the port.

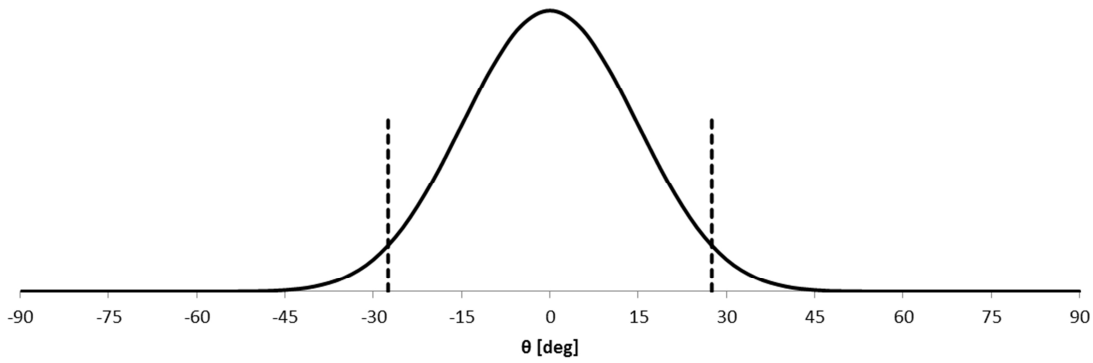


Figure 5.3 - Normalised $\cos^{15}(\theta)$ directional distribution

Note that these issues related to oblique waves exist in numerical models as well, so there are no dissimilarities with the physical model. These issues do therefore not hinder accurate numerical simulation of the physical model tests. Not addressing these issues would however result in a less realistic scale model.

Trade-offs regarding model scale and position

The model's scale and position within the wave basin have been chosen based on several considerations, of which some have already been presented in this chapter. A summary is given in Table 5.3.

Table 5.3 – Pros and cons of model scale and location

Option	Advantages	Disadvantages
Positioning the model close to the wave board	<ul style="list-style-type: none"> - Waves can enter the port under large obliqueness - Smaller model domain reduces computational cost of numerical simulations 	<ul style="list-style-type: none"> - Waves might not be fully developed or in equilibrium yet when they arrive at the port - Less space to install an array of measurement devices in front the port
Constructing a large physical model (i.e. large scale)	<ul style="list-style-type: none"> - Accurate measurements are possible (since waves scale together with the port) - The minimal required water depth in the basin is less limiting (so shallower water conditions are possible) - Waves with short periods can be generated more accurately 	<ul style="list-style-type: none"> - More construction material is needed. This is especially of importance to the breakwater, whose volume increases with the third power of scale. - Less space is available in front of the port (expressed in number of wavelengths) and/or the maximum wave angle is decreased.

Table 5.3 shows that some trade-offs are necessary. A scale of 1:45 and a distance from the wave board of 15 meters is considered optimal and has been adopted.

5.3.4 Model dimensions

Figure 5.4 shows a top view of the wave basin including the entire model. The useable part of the wave basin is approximately 40 x 40 meter, and is the area exactly in front of the wave board.

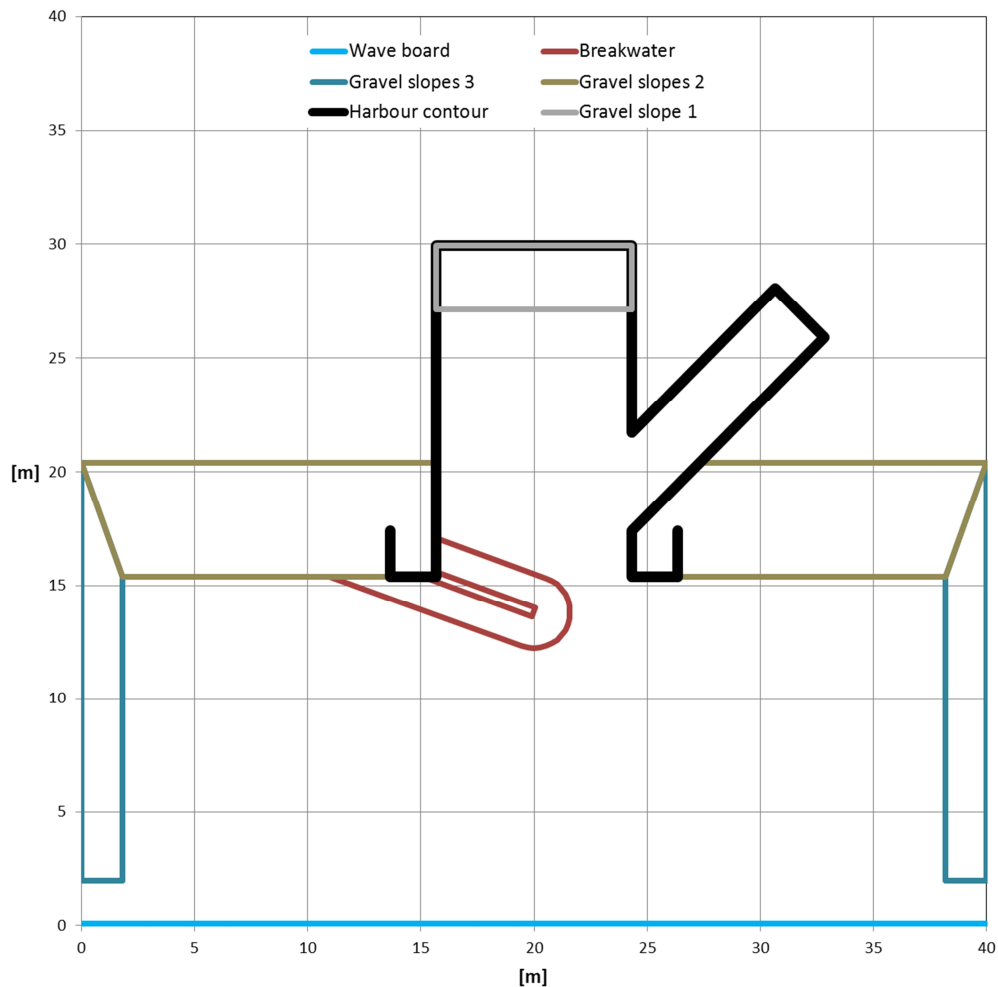


Figure 5.4 - Top view of the scale model

The properties of the objects in Figure 5.4 are summarised in Table 5.4.

Table 5.4 - Properties of objects in the scale model

	Material	Length [m]	Width [m]	Height [m]	Stone size [mm]	Slope
Quay wall	Concrete blocks	1	0.3	1.3	-	Vertical
Breakwater	Gravel	4.6 (crest)	3.2	0.7	22-40	1:2
Gravel slope 1	Gravel	-	2.8	0.7	150	1:4
Gravel slopes 2	Gravel	-	5	0.7	150	Front 1:4 Back 1:3
Gravel slopes 3	Gravel	-	1.8	0.9	150	1:2

The gravel slopes are placed to dissipate wave energy, since there would otherwise be very little damping in the basin.

Figure 5.5 shows the model during construction. Note that gravel slope 1 has not been placed yet and the right part of gravel slope 2 must still be closed in this picture.



Figure 5.5 - The scale model during construction

5.4 Test wave conditions

5.4.1 Types of wave conditions

The following types of wave conditions have been simulated in the wave basin:

- Monochromatic waves
- Bichromatic waves
- Long-crested JONSWAP
- Short-crested JONSWAP
- Colliding waves

Simulating monochromatic waves makes it possible to study certain wave components separately, since no wave-wave interactions take place. The bichromatic wave conditions include bound long waves, whose frequency is equal to the frequency difference of the two primary waves. The purpose of this wave condition is to investigate the ability of the numerical models to reproduce this nonlinear process.

The JONSWAP and colliding wave conditions are chosen to represent a realistic sea state. The colliding wave conditions consist of swell and sea with different mean directions.

5.4.2 Range of wave conditions

Being able to determine application boundaries for numerical models requires the simulation of a range of wave conditions. Such a range of wave conditions can be obtained by varying the wave height, wave period and water depth. Froude scaling is applied to scale the waves in the wave basin to prototype scale. This ensures gravity forces, which drive surface waves, are scaled correctly.

Wave breaking limits

Wave steepness is theoretically limited by the well-known Miche-criterion:

$$\frac{H_{\max}}{L} = 0.142 \tanh(kh) \quad (34)$$

This criterion is marked by the solid red line in Figure 5.6. When waves are irregular, the highest or steepest waves will break first, affecting the wave height exceedance curve. Based on flume tests, Klein Breteler (2010) concludes that

$$\frac{H_{m0}}{h} = 0.32 \quad (35)$$

is the limit for which the wave height exceedance curve is still acceptable. This limit is denoted by the striped red line in Figure 5.6.

Limits of the wave basin

The physical model has been constructed in the Delta Basin of Deltares, located in Delft. Some key specifications of this wave basin and, more importantly, the used wave board, are summarised in Table 5.5.

Table 5.5 - Specifications of the Delta Basin

Total size of the basin	50 x 50 [m]
Maximum water depth	1 [m]
Length of wave board	40 [m]
Number of segments	100 [-]
Available stroke	1.2 [m]
Wave generator power	100 [kW]

The available stroke is a limiting factor for the maximum wave height that can be generated. This is especially the case for long waves. The formula for the stroke limit is given by (Wenneker 2012), his source: (Biesel 1951)):

$$\frac{H}{S} = \frac{2 \sinh^2(kh)}{\sinh(kh) \cosh(kh) + kh} \quad (36)$$

With H wave height
 S stroke
 k wave number
 h water depth

The blue line in Figure 5.6 shows the stroke limit for an available stroke of 1.2 meter and a water depth of 0.44 meter. It can be seen that this limit is hardly restrictive for short waves in the Delta basin.

Other limits on the wave regimes that can be tested arise due to the minimal wave height and wave period that are required. A minimal wave height of 5 cm is considered sufficient to enable accurate measurements, the limit this causes is denoted by a black dash dot line in Figure 5.6. Only wave periods of 0.5 seconds or longer are considered, to avoid the generation of spurious waves due to the width of the wave board segments (applies only to oblique waves). The resulting limit is denoted by the black dashed line in Figure 5.6.

Test wave regimes

The wave conditions of all 57 tests that are carried out in the wave basin are plotted in Figure 5.6, together with the limits described in the previous sections. Keep in mind that only incoming wave conditions are considered in the figure, at certain locations in the scale model the waves will of course be larger or smaller. For wave spectra, only the significant wave height and peak period are plotted. Note that some wave conditions fall outside the area of wave conditions that are considered suitable to study in the Delta Basin. This is due to the low wave heights of these

conditions. It turns out however that these wave heights are large enough to enable accurate measurements. The wave conditions are presented in terms of H / gT^2 and h / gT^2 (following Dean (1970)), since T^2 is proportional to wavelength.

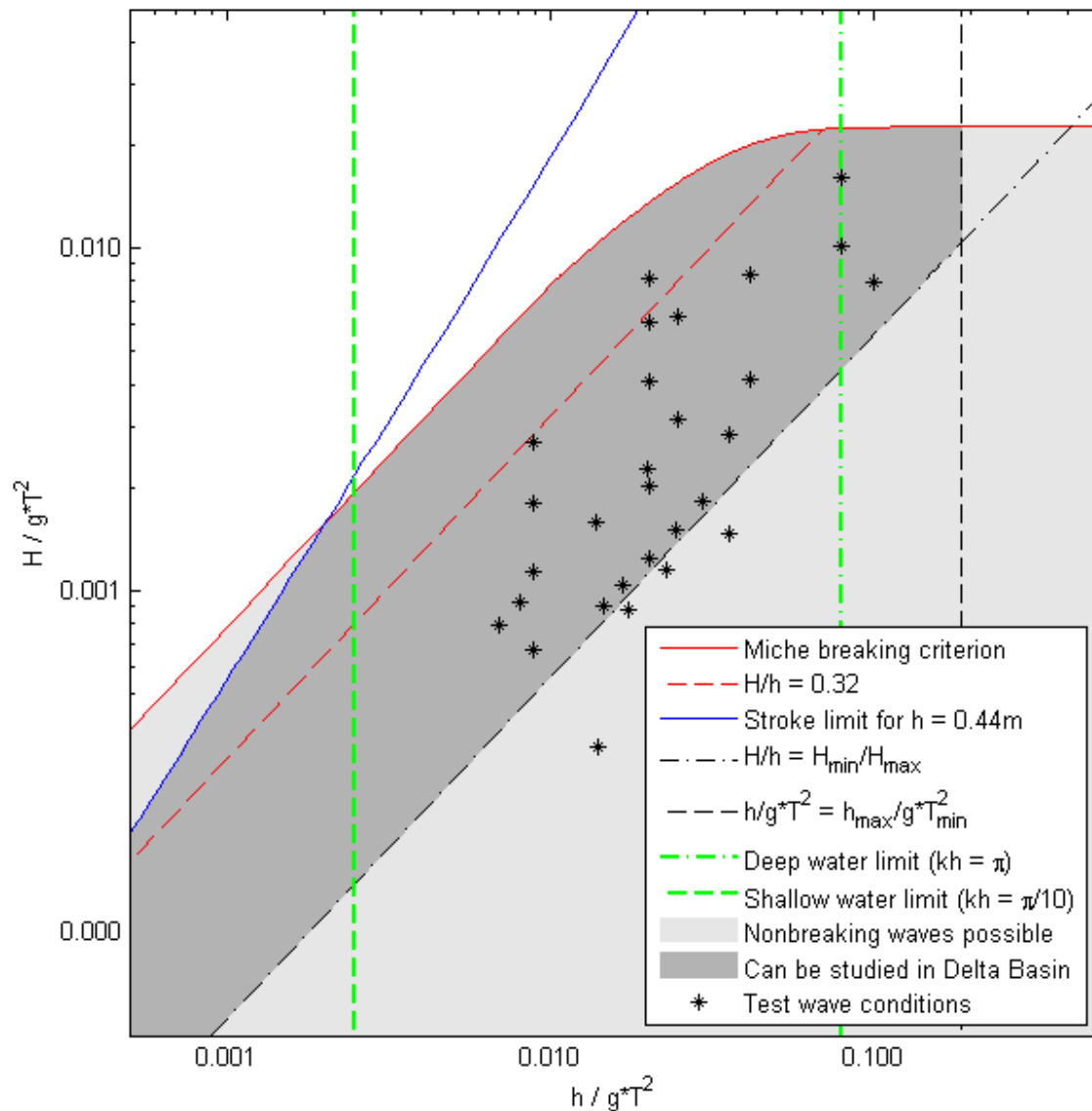


Figure 5.6 - Test wave conditions (adapted from (Dean 1970)). A list of all wave conditions is included in Appendix D, dimensionless numbers characterising certain wave conditions can be found in Table 6.1.

5.4.3 Wave board steering

The test wave conditions comprise relatively high waves in relatively shallow water. The waves are thus subject to nonlinear effects, resulting in for instance bound low frequency waves and higher harmonics (which both travel with the same speed as their corresponding primary wave).

To accurately generate these wave conditions, second order wave board steering is required. When first order wave board steering would be applied, nonlinear effects are not taken into account. This leads to the occurrence of additional spurious wave components, such as free low frequency waves

(which travel faster than the bound low frequency waves). All long crested wave conditions are therefore generated using second order wave board steering, as described in (Van Dongeren, et al. 2001).

5.5 Observations during the execution of the physical modelling

The breakwater was damaged by waves during the execution of the tests. Most damage occurred during one particular experiment, namely T081. A lot of wave breaking was observed during this experiment as well. The shape of the breakwater has been measured after the experiments were finished, to be able to take this shape into account in numerical simulations (see Appendix A).

6 Selection of tests from physical modelling

6.1 Introduction

A total of 57 tests, listed in Appendix D, were conducted in the wave basin. A selection of these tests will be further analysed and simulated with the numerical models. Tests will be selected based on their appropriateness for studying overall model performance and basin oscillations.

6.2 Most suitable wave conditions

To assess the overall performance of operational models, realistic wave conditions are preferred. Therefore the Jonswap and colliding (consisting of two irregular wave fields with different mean directions) wave conditions are considered to be the most suitable. For the colliding wave conditions it is however much more difficult to compute time series of water surface elevation from the wave board motions, since these waves are not unidirectional and perpendicular to the wave board. Another reason to use the long-crested Jonswap tests is that a range of significant wave heights and peak periods are tested, which enables the determination of application boundaries. The tested Jonswap wave conditions contain a large range of wavelengths, which makes them also well suited for studying harbour oscillations.

The disadvantage of monochromatic and bichromatic waves is that they lead to pronounced standing wave patterns in the scale model. The location of the nodes and anti-nodes depends on the geometry of the scale model. If this geometry is slightly different in a numerical model, which is inevitable, the wave pattern will be somewhat different as well. Resulting wave heights will thus be different and the comparison with physical model tests will be unclear. Another disadvantage is that harbour oscillations are not likely to be triggered when only one or two primary wave components are imposed.

When wave spectra are simulated, the resulting wave height fields are much smoother (standing wave patterns are less pronounced). The downsides are that longer simulation times are necessary compared to monochromatic waves to get a statistically sound realisation of the spectrum and that wave components cannot be studied individually.

6.3 Most suitable scale model layouts

Just as with the wave conditions, realistic port layouts are considered beneficial for studying overall model performance. Since harbour oscillations depend primarily on the geometry of the harbour, it is interesting to study this phenomenon in different scale model layouts.

6.4 Selected experiments

Based on the considerations discussed in the section 6.2, only long-crested Jonswap wave conditions are selected. Six tests are selected with layout 3 (the most complex layout), from which the overall performance of numerical models will be analysed. These six tests differ in significant wave height and peak wave period.

In addition to this two more tests are selected, one for layout 1 and one for layout 2, for the analysis of harbour oscillations. The test with layout 2 uses the exact same wave conditions as one of the selected tests with layout 3. The test with layout 1 uses lower waves, but was selected nonetheless because it was the only test with layout 1 that uses a Jonswap spectrum.

The direction of the generated waves is always perpendicular to the wave board. An overview of the wave conditions corresponding to each selected test is presented in Table 6.1. The dimensional values in Table 6.1 can be scaled to prototype dimensions using Froude scaling and a scale of about 1:45 (multiply wave periods with a factor $\sqrt{45}$).

Table 6.1 - Selected tests, conditions in model scale (1:45)

Test	Layout	Hs [m]	Tp [s]	h [m]	kh [-]	H/L [-]	a/h [-]	Ursell number [-]
T014	1	0.032	1.49	0.44	1.0	0.01	0.04	2.7
T035	2	0.106	1.49	0.44	1.0	0.04	0.12	9.0
T076	3	0.052	1.49	0.44	1.0	0.02	0.06	4.4
T079	3	0.106	1.49	0.44	1.0	0.04	0.12	9.0
T080	3	0.159	1.49	0.44	1.0	0.06	0.18	13.4
T081	3	0.214	1.49	0.44	1.0	0.08	0.24	18.1
T084	3	0.106	1.04	0.44	1.7	0.07	0.12	3.1
T085	3	0.101	2.24	0.44	0.6	0.02	0.11	22.7

The Ursell number, included in Table 6.1, is defined as: $U = \frac{HL^2}{h^3}$.

7 Analysis of physical model results for selected tests

In this chapter results from the scale model tests are presented and discussed. Primary waves and low frequency harbour oscillations are treated separately. In addition to this, reflection coefficients of objects in the scale model are determined.

7.1 Primary waves

In this section, primary waves in the scale model are analysed. All wave energy corresponding to a frequency of 0.2 Hz (which would be 0.03 Hz on prototype scale) or lower is therefore discarded. This enables a clearer comparison between the results from the scale model and the numerical models in the subsequent chapters (especially for PHAROS results that do not contain low frequency waves). Measurements of the first five minutes of each experiment are not included in the analyses, this period is regarded as spin-up time.

The experiments considered in this section are described Chapter 6. For convenience, essential characteristics of these experiments are repeated in Table 7.1. All experiments are with long crested Jonswap wave conditions with a direction perpendicular to the wave board.

Table 7.1 - Characteristics of analysed experiments

Test	Layout	Hs [m]	Tp [s]	h [m]	Kh [-]	H/L [-]	a/h [-]	Ursell number [-]
T076	3	0.052	1.49	0.44	1.0	0.02	0.06	4.4
T079	3	0.106	1.49	0.44	1.0	0.04	0.12	9.0
T080	3	0.159	1.49	0.44	1.0	0.06	0.18	13.4
T081	3	0.214	1.49	0.44	1.0	0.08	0.24	18.1
T084	3	0.106	1.04	0.44	1.7	0.07	0.12	3.1
T085	3	0.101	2.24	0.44	0.6	0.02	0.11	22.7

7.1.1 Wave breaking

The wave conditions regarded here comprise a variety of non-linearity, see the last three columns of Table 7.1. In the tests with the more severe wave conditions, T081 in particular, quite some breaking was observed. Since the highest waves in the wave field break the most, this breaking affects the shape of the wave height probability density function.

Theoretically, wave heights are Rayleigh distributed if no breaking is present. It is thus interesting to see how much the distribution of the measured wave heights deviate from the Rayleigh distribution, as this deviation can be regarded as a measure for the amount of wave breaking.

The wave height distribution calculated from measured surface elevations at wave gauge 1 (bottom left, see Figure 5.1) are therefore graphed together with their corresponding Rayleigh distribution in Figure 7.1. The location of wave gauge 1 is chosen because waves at this location are not so much affected by wave reflections. The computed Rayleigh distributions are based on the average wave height of the 1/3 highest waves (i.e. the significant wave height from a time domain analysis), which are provided in Table 7.2. The Rayleigh distributions are given by (Holthuijsen 2007):

$$P\{\underline{H} < H\} = 1 - \exp\left(-2\left(\frac{H}{H_{1/3}}\right)^2\right) \quad (37)$$

Table 7.2 - Significant wave heights ($H_{1/3}$) at wave gauge 1

	T076	T079	T080	T081	T084	T085
$H_{1/3}$ [m]	0.054	0.108	0.149	0.176	0.096	0.089

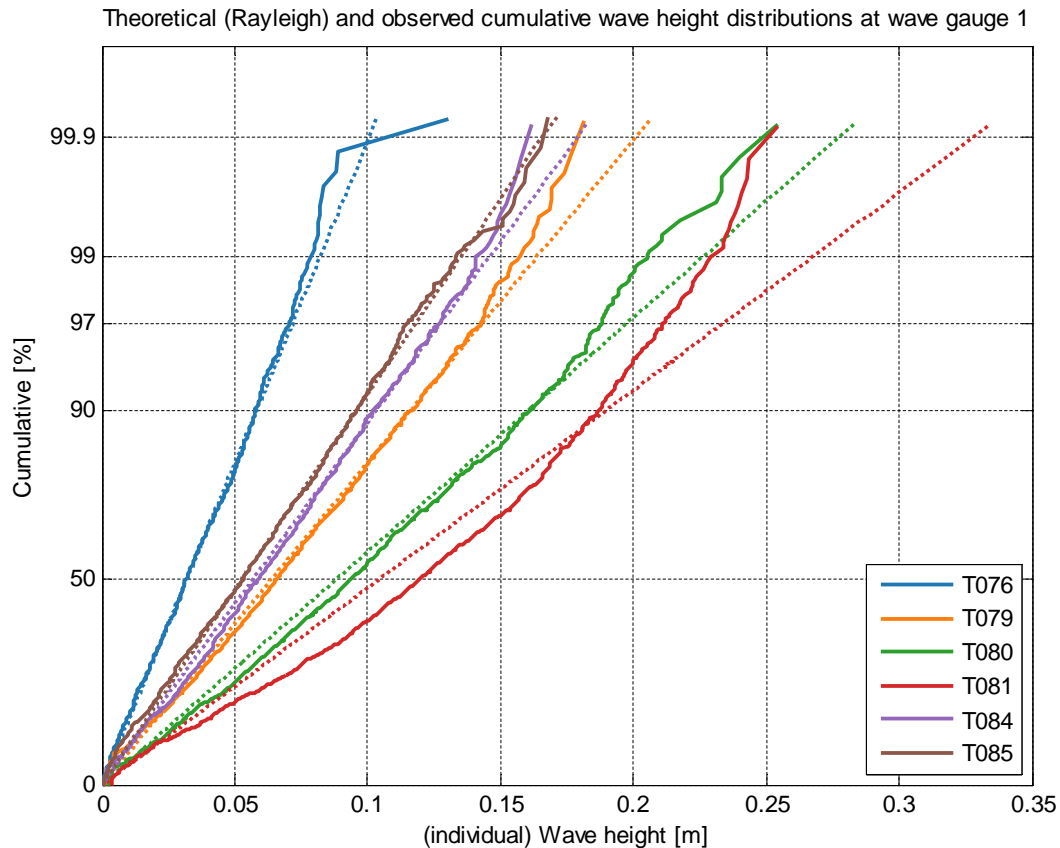


Figure 7.1 – Cumulative distributions of wave heights, plotted with Rayleigh scales. Solid lines correspond to measured waves, dotted lines represent Rayleigh distributions. The non-dimensional wave heights, wave periods and wave steepnesses corresponding to the wave conditions in this figure are included in Table 7.1.

Figure 7.1 shows that the cumulative distribution of wave heights for test T081 deviates significantly from the theoretical Rayleigh distribution. As expected, the highest waves are underrepresented in comparison with the Rayleigh distribution. Notable is also that the highest wave measured in test T081 has approximately the same height as the highest wave measured in test T080. This indicates that the maximum possible wave height in the basin is limited, and that this limit has been reached.

Amplitude dispersion causes the front of a wave to steepen until it eventually breaks. The amount of amplitude dispersion depends on the ratio between the wave height and water depth. The difference between the observed and theoretical wave height distribution (see Figure 7.1) shows a strong correlation with this ratio as well. This difference clearly increases when higher waves are generated.

It appears that a correlation with wave period or steepness of the imposed waves does not exist for tests that are considered here. The graphs for T079, T084 and T085 are for instance quite similar, while the wave periods and imposed wave steepnesses vary significantly for these tests. Also note that these three tests use of course different wave spectra, while the tests T076, T079, T080 and T081 have the same realisation of the imposed Jonswap spectrum (scaled to fit the required significant wave height). It can thus be concluded that the breaking is induced by the limited water depth.

7.1.2 Wave heights

All measured significant wave heights are visualised in Figure 7.2. At each measurement location, the six wave heights belonging to the experiments listed in Table 7.1 are depicted in the form of a cross. Within this cross, the imposed wave height increases from left to right while the dimensionless water depth kh of the imposed waves increases from bottom to top (with decreasing wave period).

For each experiment, the set of wave heights are normalised with the wave height measured at wave gauge 1 (most left in Figure 7.2). This gives a clear picture of the distribution of measured wave heights throughout the domain. More importantly, dependencies of the normalised wave heights on absolute wave height and wave period can be recognised as well.

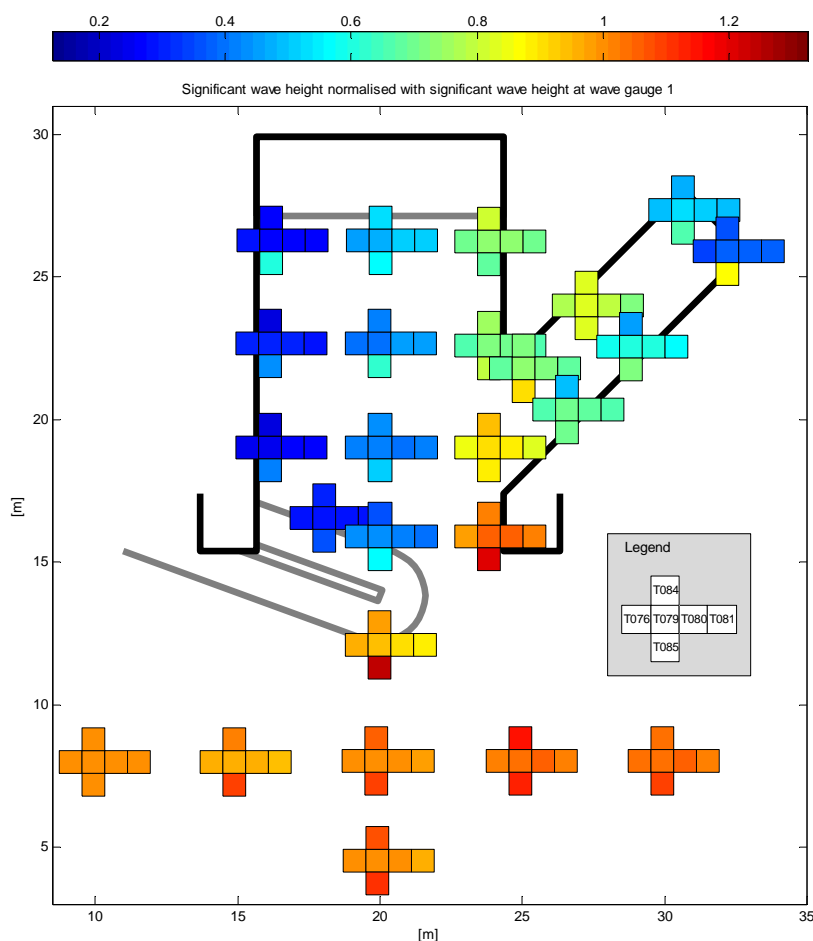


Figure 7.2 - Significant wave height, at measurement locations presented in Figure 5.1

The normalised significant wave heights in front of the harbour are on average slightly higher on the right side compared to the left side, see Figure 7.2. This is probably caused by waves reflecting on the concrete wall located at $x=24-26$ m, $y=15$ m.

In the shadow zone of the breakwater, wave heights are approximately a third of the wave heights in front of the harbour. Figure 7.2 also shows that the normalised wave heights increase with increasing wavelength in this area (compare T084, T079 and T085). This trend is caused by the fact that long waves diffract more than short waves. The same trend can be recognized in the side basin, where wave energy also enters by means of diffraction.

It can also be noticed from Figure 7.2 how measured wave heights decrease towards the back of the harbour, along measurement locations 13, 14, 15 and 16 (the ray at $x=24$ m). This looks similar to geometrical damping (energy per unit surface area decreases as energy spreads over a larger area). Wave energy that enters the harbour near location 13 diffuses, resulting in less wave energy in the back of the harbour.

The tests T076, T079, T080 and T081 have the same realisation of the imposed Jonswap spectrum; only the wave heights are different. The interference patterns in the wave basin are therefore similar for these tests. This explains why the normalised measured wave heights vary much more with the peak period of the imposed wave spectrum than with wave height of the imposed spectrum.

7.1.3 Wave periods

A mean wave period based on the minus first and zeroth order moments of the wave spectrum, indicated with $T_{m-1,0}$ hereafter, is computed for all measurements. These wave periods are presented in Figure 7.3, in the same format as the significant wave heights were presented in Figure 7.2. Wave periods are again normalised with the values corresponding to wave gauge 1.

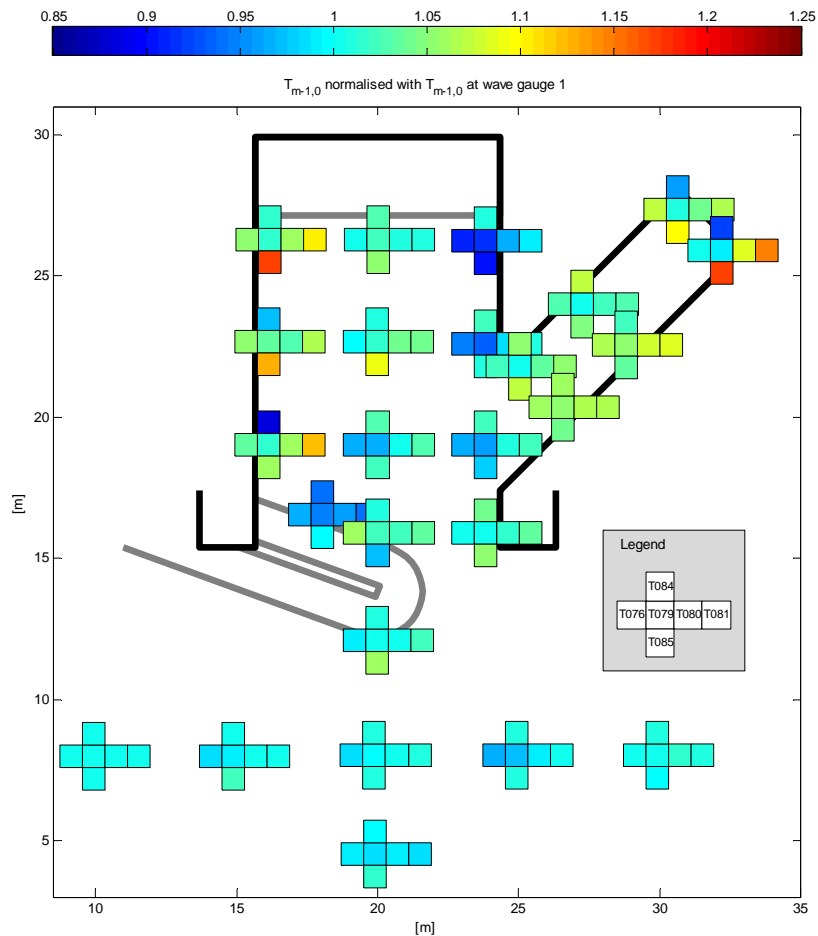


Figure 7.3 - Mean wave periods based on m_{-1} and m_0 of wave spectrum, at measurement locations presented in Figure 5.1

In front of the harbour the normalised mean wave periods are approximately equal and show no clear correlation with location or wave parameters.

Inside the harbour a similar pattern can be observed as with the wave heights. In the shadow zone of the breakwater and in the side basin, mean wave periods are longer than in front of the harbour, while the mean wave periods are shorter at the ray $x=24\text{m}$. The shifting of the mean wave period along the ray at $x=24\text{m}$ indicates that short wave energy propagates straight towards the back of the main basin while longer waves diffract stronger (towards the side basin and the shadow zone of the breakwater).

The mean wave periods at location 6 (close to the breakwater, at the lee side, see Figure 5.1) are relatively short. It should be noted that wave heights at this location are quite small as well. The relatively high amount of high frequency wave energy at this location could be generated through nonlinear processes around the breakwater and refracted towards location 6.

7.2 Low frequency waves and harbour oscillations

In this section, harbour oscillations in a selection of experiments described in Chapter 6 are analysed. Characteristics of these experiments are repeated in Table 7.3. All experiments use long crested Jonswap wave conditions with a direction perpendicular to the wave board. Note that tests T035 and T079 use exactly the same wave conditions.

Table 7.3 – Analysed experiments

Test	Layout	Hs [m]	Tp [s]	h [m]	kh [-]	H/L [-]	a/h [-]	Ursell number [-]
T014	1	0.032	1.49	0.44	1.0	0.01	0.04	2.7
T035	2	0.106	1.49	0.44	1.0	0.04	0.12	9.0
T079	3	0.106	1.49	0.44	1.0	0.04	0.12	9.0

7.2.1 Low frequency wave energy

Isolating the energy belonging to low frequency waves is done by integrating the computed wave spectra up to a certain frequency. The wave spectra generally show a clear distinction between low frequency wave energy and primary wave energy – very little wave energy is present at frequencies in the range 0.25 – 0.35 Hz. Waves with frequencies up to 0.3 Hz are therefore considered low frequency waves throughout this section. This corresponds to wave periods of 22 seconds and more on prototype scale, which are known to cause hinder for port operations.

The total amount of low frequency wave energy measured at each wave gauge for the three selected tests is presented in Figure 7.4. The significant low frequency wave heights in tests T035 and T079 are about 10 times those of test T014, while the total significant wave heights differs a factor 3.3. This is due to the nonlinear nature of low frequency waves. It is also interesting to see that the breakwater in test T079 appears to reduce the amount of low frequency wave energy inside the harbour.

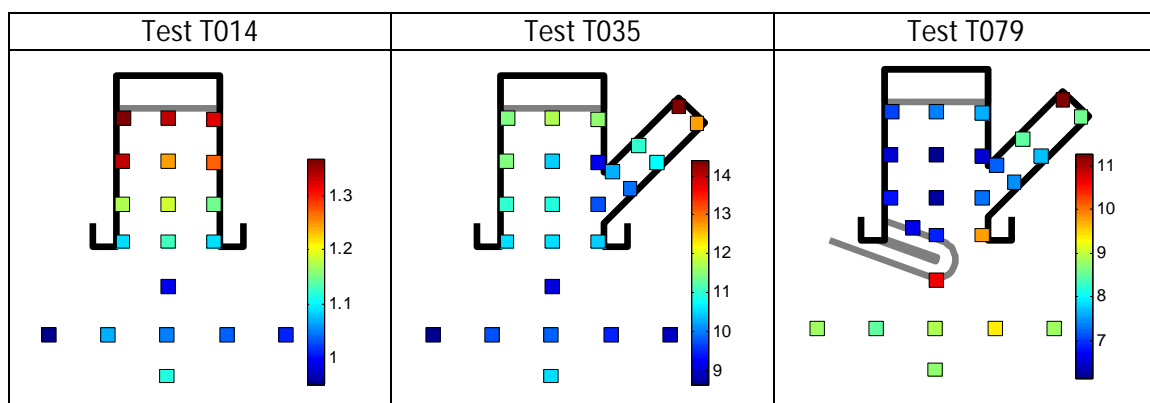


Figure 7.4 – Significant wave heights of low frequency waves [mm]

7.2.2 Harbour oscillations

A closer look at the low frequency wave spectrum reveals the different resonant modes that are excited in the harbour. The measurements are however also contaminated with modes that are related to the wave basin itself and have nothing to do with the modelled port. A typical low frequency wave spectrum is shown in Figure 7.5.

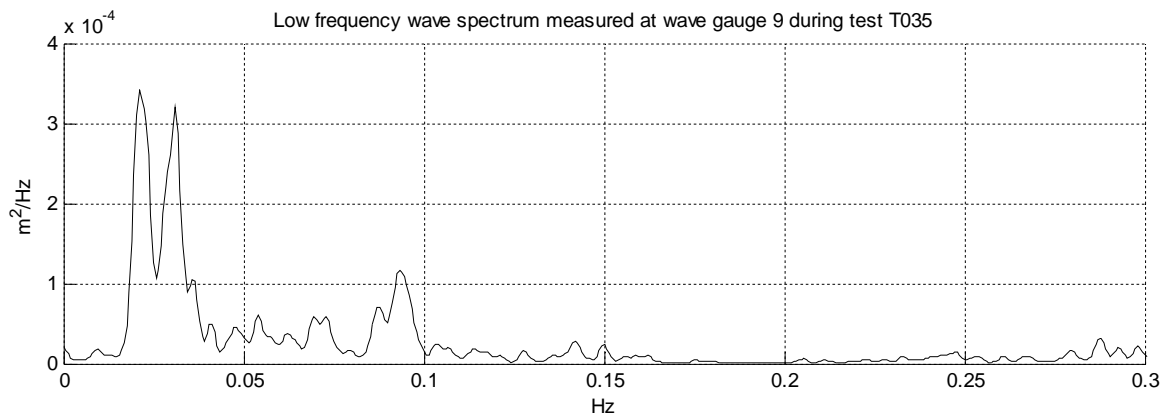


Figure 7.5 - Low frequency wave spectrum in main basin for test T035

Analysing harbour oscillations directly from spectra as shown in Figure 7.5 is not very convenient. Therefore a selection of harbour modes is made, which are studied in the spatial domain instead. These modes are visualised by computing and plotting the corresponding significant wave heights at all measurement locations. The significant wave heights are obtained through integration of narrow frequency ranges of the measured wave spectra. These narrow frequency ranges – which are specified in Figure 7.6 – encompass the frequency of the considered harbour oscillation.

The most energetic harbour oscillations found are those that correspond to a so called Helmholtz mode (also known as zeroth mode or pumping mode). These modes usually cause the most hindrance to port operations. For test T014, the first mode in the longitudinal direction of the port can also be recognized clearly (as a standing wave with a wavelength of approximately 4/3 the basin length). An overview of these modes is presented in Figure 7.6.

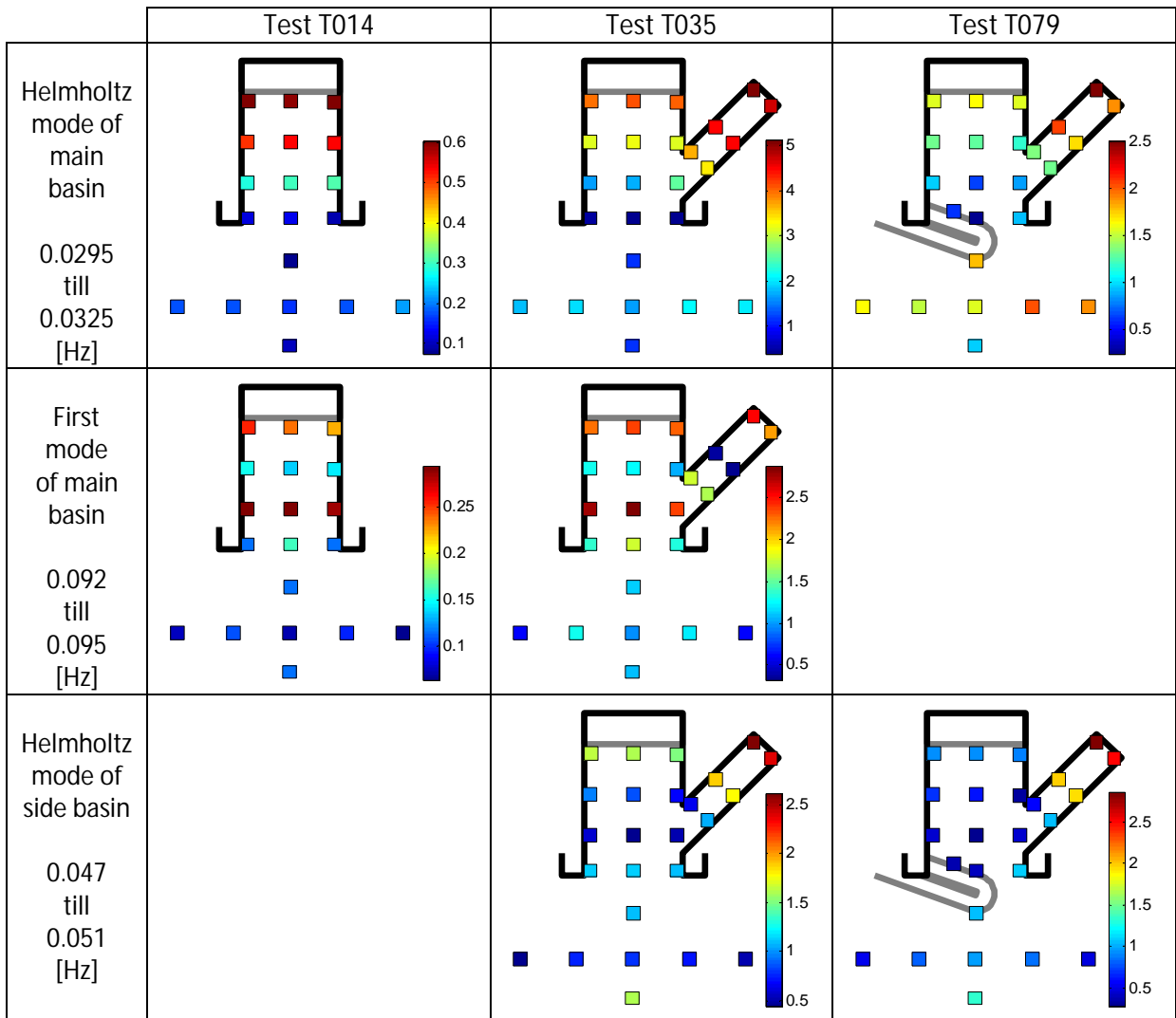


Figure 7.6 – Measured low frequency wave energy and harbour oscillations (significant wave heights in millimetres)

Figure 7.6 shows that the Helmholtz modes contain more energy than the higher modes. It is also evident that the oscillations in the main basin are attenuated by the breakwater. The effect of the breakwater on the oscillations in the side basin is much less.

The first mode in the main basin can hardly be recognized when the breakwater is present. Instead, a number of seiching modes arise. These modes can however not be clearly defined in terms of frequency. This is probably because the standing waves lie diagonal in the main basin, so their lengths are not very well defined either.

The wavelengths and basin lengths corresponding to the described harbour oscillations are provided in Table 7.4. It is interesting to note that a quarter of the wavelength corresponding to the Helmholtz mode of the main basin ($0.25 \cdot 67 = 16.75\text{m}$) is larger than the length of this basin (13.49m). The nodal line of this mode (i.e. the locations where the amplitude in surface elevation is zero and the amplitude in velocity is maximal) thus lies in front of the harbour entrance. This phenomenon is caused by wave energy radiating out of the harbour. It is most evident for basins with a large width to length ratio and a large width of mouth to basin width ratio (Rabinovich 2009).

Table 7.4 – Wavelengths corresponding to the harbour modes

Mode	Frequency [Hz]	Wavelength from dispersion relation [m]	Length of basin [m]
Helmholtz mode of main basin	0.031	67.00	13.49
First mode of main basin	0.093	22.28	13.49
Helmholtz mode of side basin	0.049	42.37	8.96 – 14.31 11.63

7.2.3 Time dependency

The amplitudes of the harbour oscillations vary significantly in time, as is illustrated in the lower panel of Figure 7.7. The oscillations can arise or damp out within a minute. The top panel of Figure 7.7 shows the primary wave energy at wave gauge 1 (which is located next to the harbour, close to the wave board). A correlation between the primary wave energy (top panel) and low frequency wave energy (lower panel) is visible. High amounts of low frequency wave energy are associated with peaks in the primary wave frequency band.

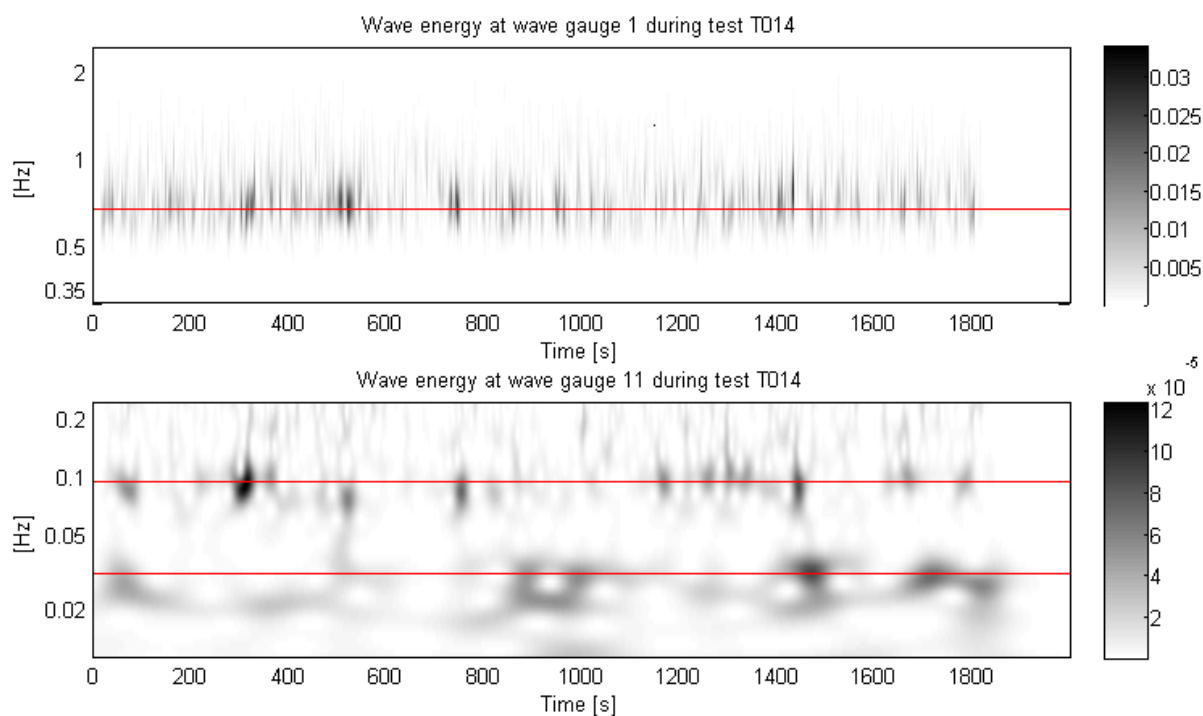


Figure 7.7 – Measured energy densities. The red lines indicate the peak frequency (0.67 Hz), the Helmholtz mode (0.031 Hz) and the first mode in the main basin (0.093 Hz).

Figure 7.7 also shows the presence of energy at frequencies lower than the frequency corresponding to the Helmholtz mode of the main basin. The length scales corresponding to these very low frequencies are too long to be related to the modelled harbour and are in fact related to the wave basin itself. The energy around 0.02 Hz is for instance clearly visible in test T035 as well, see Figure 7.5.

8 Comparisons between measurements and numerical simulation

The scale model tests have been simulated with the numerical wave models PHAROS, TRITON and SWASH. Basic information regarding the setup of the numerical simulations is provided below, details can be found in Appendix A. In this chapter the results from the numerical simulations are compared to the scale model results. First the primary waves are treated, followed by the low frequency waves and harbour oscillations.

PHAROS settings

- Grid resolution: at least 12 nodes per wavelength
- All boundaries are located at the still water line, and the following reflection coefficients are assigned:
 - Vertical concrete walls: 1
 - Breakwater: 0.3
 - Gravel slopes: 0.2
- Wave breaking is included
- No bottom friction is included

TRITON settings

- Grid resolution: 7 cm (or 38 cells per wavelength corresponding to 1.49s peak period)
- All boundaries are located at the still water line, and the following reflection coefficients are assigned:
 - Vertical concrete walls: 1
 - Breakwater: 0.3
 - Gravel slopes: 0.2
- No bottom friction is included

SWASH settings

- Grid resolution: 7 cm (or 38 cells per wavelength corresponding to 1.49s peak period)
- Number of vertical layers: 2
- Concrete walls are modelled as porous structures with a porosity of 0.1% and a stone size of 0.1 mm. Gravel slopes and the breakwater are modelled as porous structures with a porosity of 40% and a stone diameters according to Table 5.4
- No bottom friction is included

8.1 Primary waves

In this section, primary waves modelled by PHAROS, TRITON and SWASH are analysed and compared to the measured primary waves in the scale model. The same methods are used as in Section 7.1, e.g. all wave energy corresponding to a frequency of 0.2 Hz or lower is discarded. Information about the modelled wave conditions can be found in the previous chapter as well.

First, the model results are presented in a similar manner as the results from the scale model tests in Section 7.1, see Section 8.1.1. The accuracy of the model predictions is assessed and analysed in Section 8.1.2.

8.1.1 Results from numerical simulations

PHAROS

Wave heights at the measurement locations are in the case of PHAROS simulations obtained by computing the root mean square of all wave heights within 10cm of the measurement location (applying formula (23)). Increasing the area over which the representative wave height is computed has little influence on the deviations from the measurements (around 1 percentage point).

The results from the PHAROS simulations are presented in Figure 8.1. The most striking is the relatively high normalised wave heights in the shadow zone of the breakwater. Normalised wave heights in this area are about 50% larger compared to the measurements (cf. Figure 7.2).

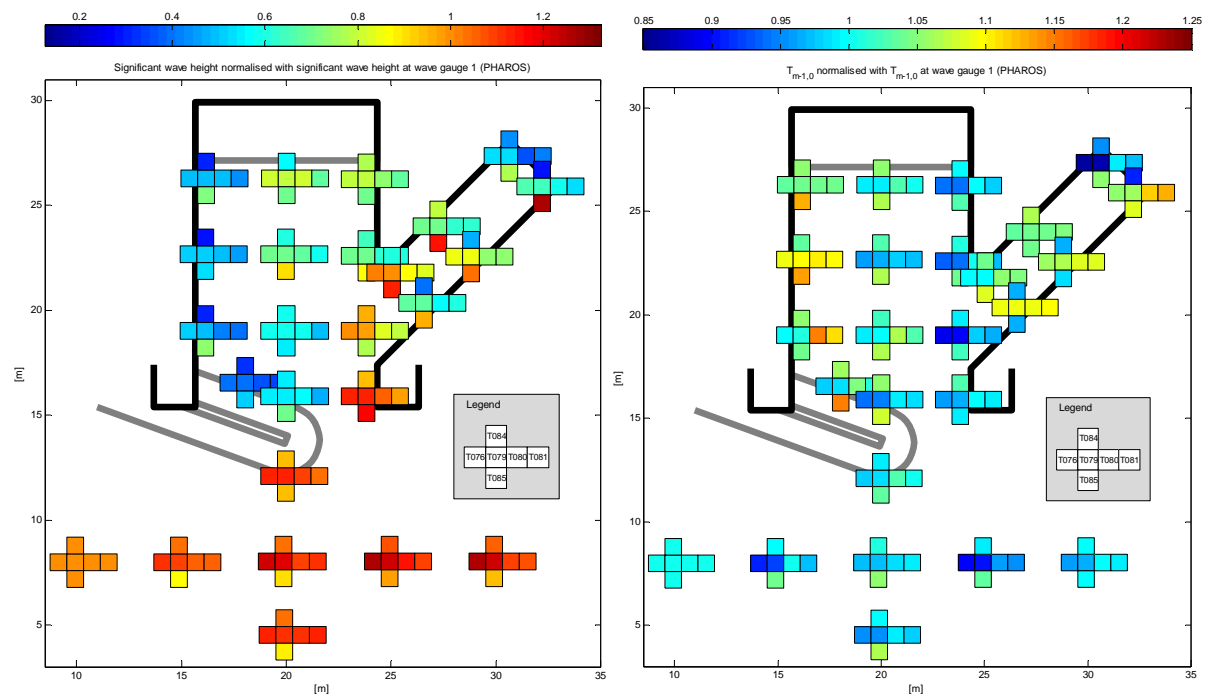


Figure 8.1 - PHAROS modelling results. Left: significant wave heights. Right: mean wave periods ($T_{m,1,0}$)

The trends that are observed in the measurements and described in section 7.1 can be summed up as follows:

- Wave heights in front of the harbour are slightly higher on the right side compared to the left side.
- Long waves diffract more towards the shadow zone of the breakwater and towards the side basin than short waves do.
- Wave heights decrease towards the back of the harbour along the ray at $x=24\text{m}$.
- Mean wave periods are relatively low at the ray at $x=24\text{m}$ and relatively high in the shadow zone of the breakwater and in the side basin, due to diffraction.

These trends can be recognized in the PHAROS results as well.

TRITON

The results from the TRITON simulations are presented in Figure 8.2. Due to numerical instabilities, it was not possible to simulate tests T080 and T081 (which have the most extreme wave conditions in

terms of a/h). The computed wave heights and wave periods of the other tests resemble the measurements fairly well.

The most notable difference is that the computed wave periods in the harbour are all equal to or larger than the computed wave periods in front of the harbour. This was not the case for the measured wave periods, see Figure 7.2. A closer look at the spectra reveals that this is mainly caused by a lack of high frequency wave energy.

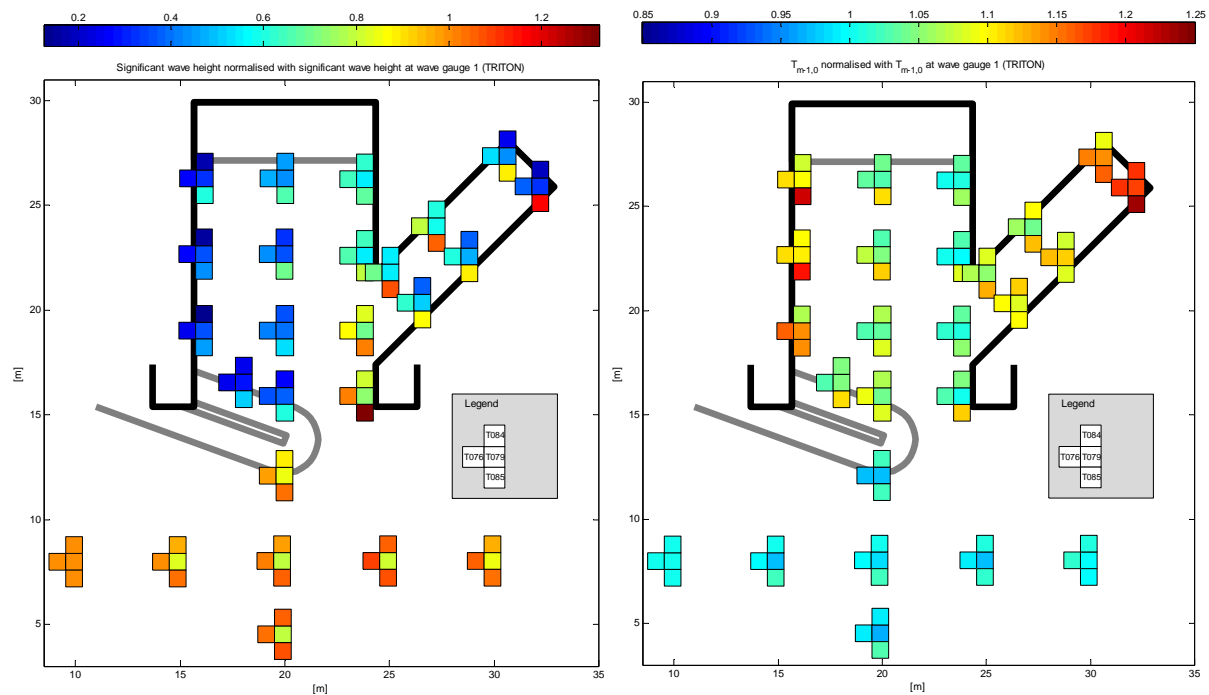


Figure 8.2 – TRITON modelling results. Left: significant wave heights. Right: mean wave periods ($T_{m-1,0}$)

SWASH

The results from the SWASH simulations are presented in Figure 8.3. The normalised wave heights inside the harbour look very similar to the normalised measured wave heights. The same trends can be recognised. In front of the harbour at $x=20\text{m}$ on the other hand, the computed wave heights are remarkable low, especially for the wave conditions with shorter waves.

As with TRITON, the lowest mean wave periods are found in front of the harbour. Although the difference between the lowest normalised computed mean wave periods inside the harbour and in front of the harbour is a little less in this case.

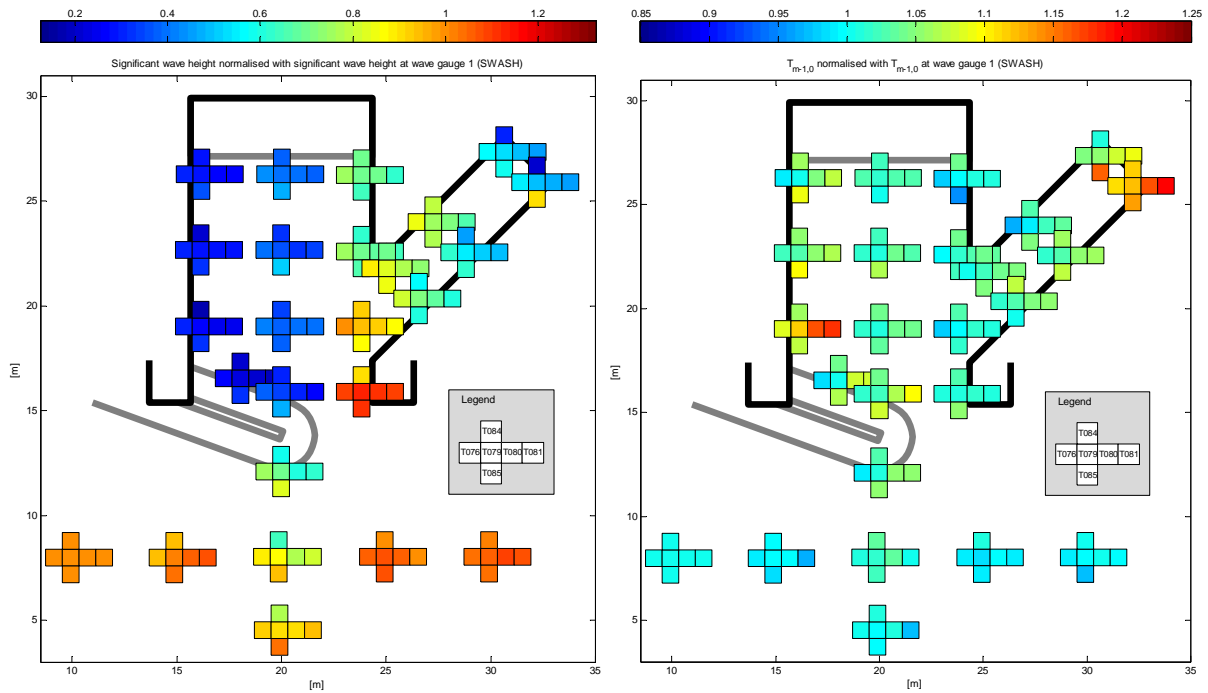


Figure 8.3 – SWASH modelling results. Left: significant wave heights. Right: mean wave periods ($T_{m-1,0}$)

8.1.2 Accuracy of the results from numerical simulations

PHAROS

Measured wave heights and wave periods are plotted against predicted wave heights and wave periods in Figure 8.4. While the mean wave periods show a good correlation, the significant wave heights are less accurate, especially when they are overestimated by PHAROS.

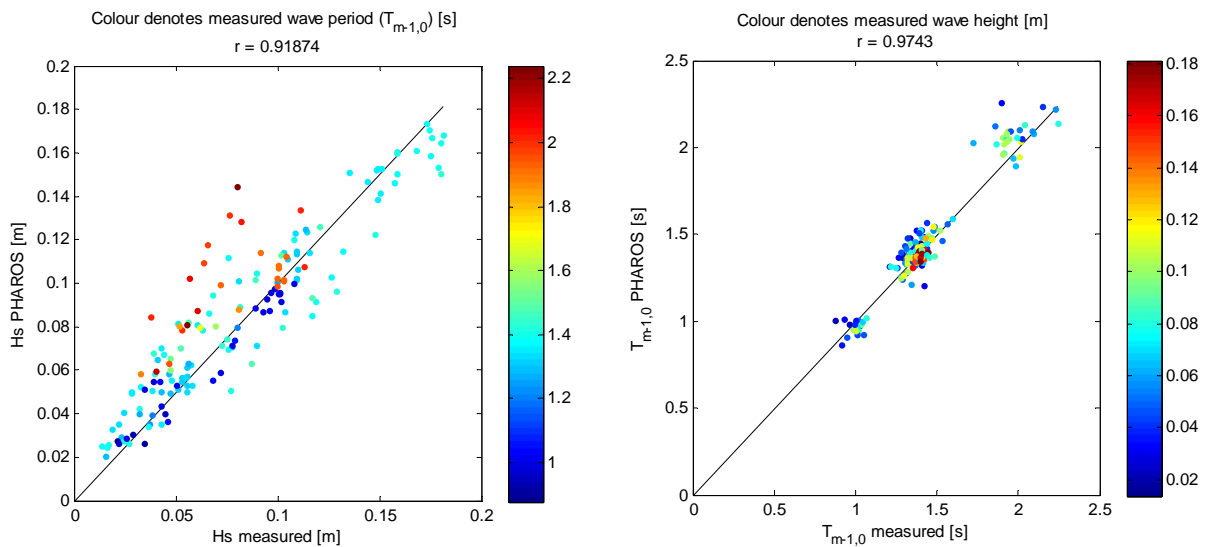


Figure 8.4 - Accuracy of PHAROS model results. Left: significant wave heights. Right: mean wave periods ($T_{m-1,0}$)

The left plot of Figure 8.4 also provides interesting information on the influence of wave height and wave period on the accuracy of the predicted wave height. The highest wave heights appear to be predicted most accurately. The colours in the left plot of Figure 8.4 indicate the mean wave period

corresponding to each wave height measurement. These show that long period waves are overestimated and short period waves are predicted most accurately.

The breaking criteria in PHAROS are based on maximum allowable values for wave steepness and for the wave height over depth ratio. This explains why high and steep waves are overestimated less than lower and less steep waves. The wave heights in the scale model were sometimes limited by wave breaking (see Section 7.1.1), and PHAROS is able to replicate this with reasonable accuracy.

The overestimation of non-breaking waves indicates that there was more energy dissipation in the physical model compared to the numerical model, for instance at the gravel slopes or concrete walls.

To get insight in how accurate the different areas of the harbour are modelled, the errors in percentages are shown in Figure 8.5. The wave heights in the shadow zone are obviously the least accurate, since wave heights are minimal there. The above mentioned correlations with wave height and wavelength are visible as well.

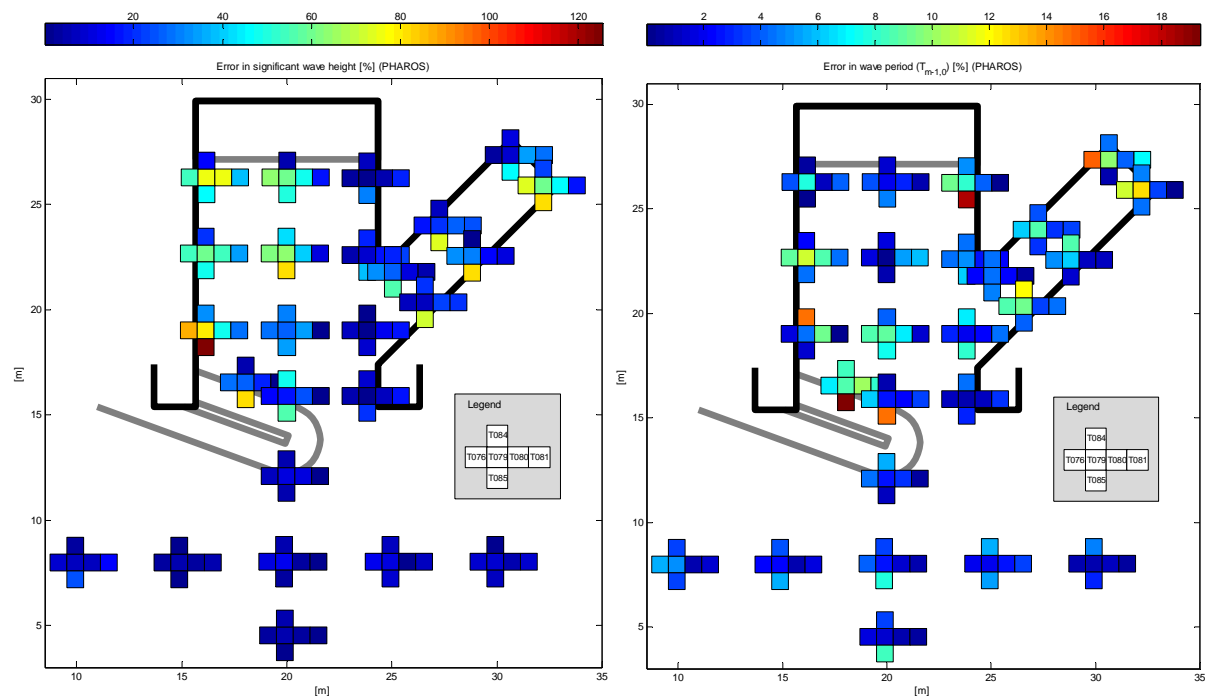


Figure 8.5 - Distribution of errors in PHAROS model results. Left: significant wave heights. Right: mean wave periods ($T_{m-1,0}$)

TRITON

Measured wave heights and wave periods are plotted against predicted wave heights and wave periods in Figure 8.6. Both the significant wave height and the mean wave periods show a good correlation with the measurements. Note however that tests T080 and T081 are not included in this comparison, as the simulation of these tests could not be completed due to numerical instabilities.

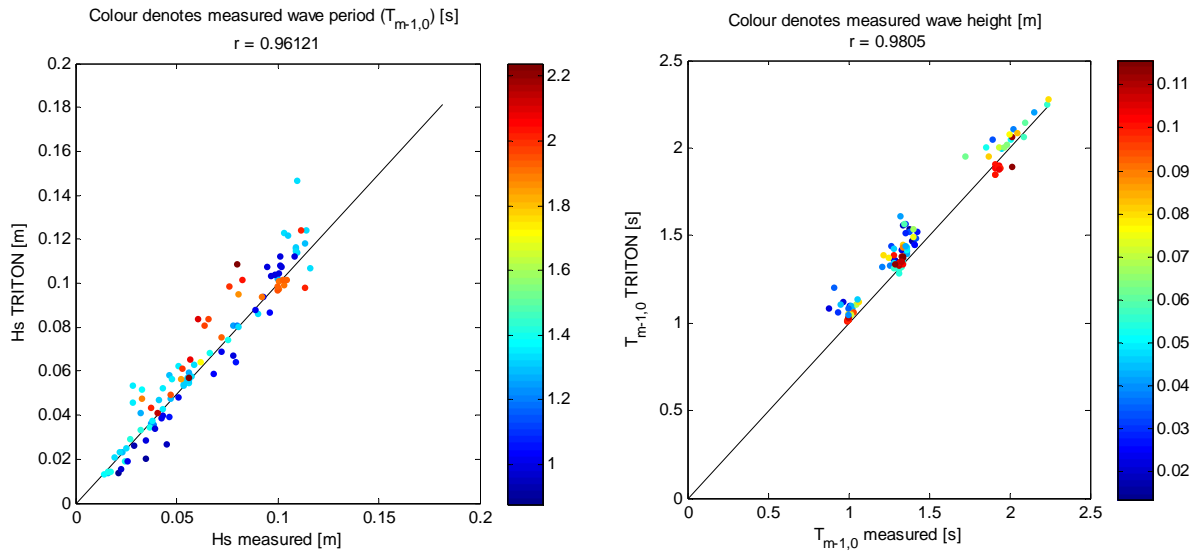


Figure 8.6 - Accuracy of TRITON model results. Left: significant wave heights. Right: mean wave periods ($T_{m-1,0}$)

The accuracy of the predicted wave heights shows little correlation with wave height or wave period. The mean wave periods are quite consistently overestimated. For larger wave heights the accuracy of the mean wave period seems to be better. This makes sense since these larger wave heights are measured in front of the port, and processes such as diffraction have little influence here.

The overestimation of mean wave periods increases as the mean wave period decreases. This indicates that short wave energy is lacking in the numerical model, probably because the computational grid is chosen too coarse. To illustrate this, wave spectra obtained from measurements of tests T084, T079 and T085 (tests with the shortest, medium, and longest waves respectively) at wave gauge 1 are provided in Figure 8.7. The coloured areas indicate the wave energy that is modelled with 20 grid cells per wavelength or less. This resolution is considered sufficient to accurately model wave celerity (expected numerical error is around 1.5%, depending on the applied numerical scheme). Red areas indicate waves which are modelled with less than 10 grid cells per wavelength.

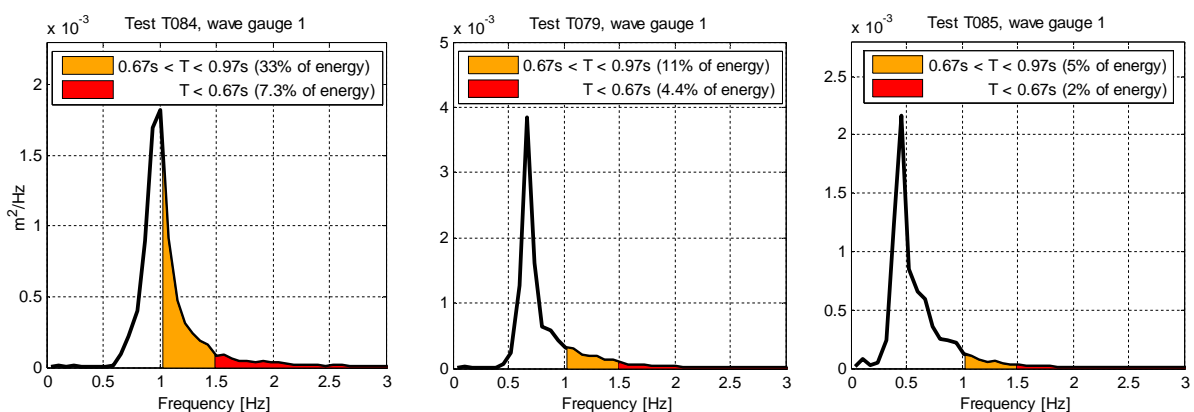


Figure 8.7 - High frequency energy in measured wave spectra.

Figure 8.7 shows that in the case of test T084 a large part of the wave spectrum is not modelled properly due to a lack of grid resolution. It is however interesting to see that the predicted wave heights for test T084 are about as accurate as the predicted wave heights for test T085, see Figure

8.6 (where the purple dots belong to T084 and the red dots indicate T085). The choice for this grid resolution was, besides accuracy, related to the fact that computational time – simulations with this grid already took over a week – increases with the third power of grid size.

An overview of relative errors in wave height and wave period is given in Figure 8.8. It shows the relative errors are largest in the shadow area of the breakwater and in the side basin, i.e. the areas where wave heights are rather small.

One should keep in mind that expressing errors in terms of percentages can be a bit misleading as overestimation of very small wave heights results in large percentage errors, even though the absolute error might be small.

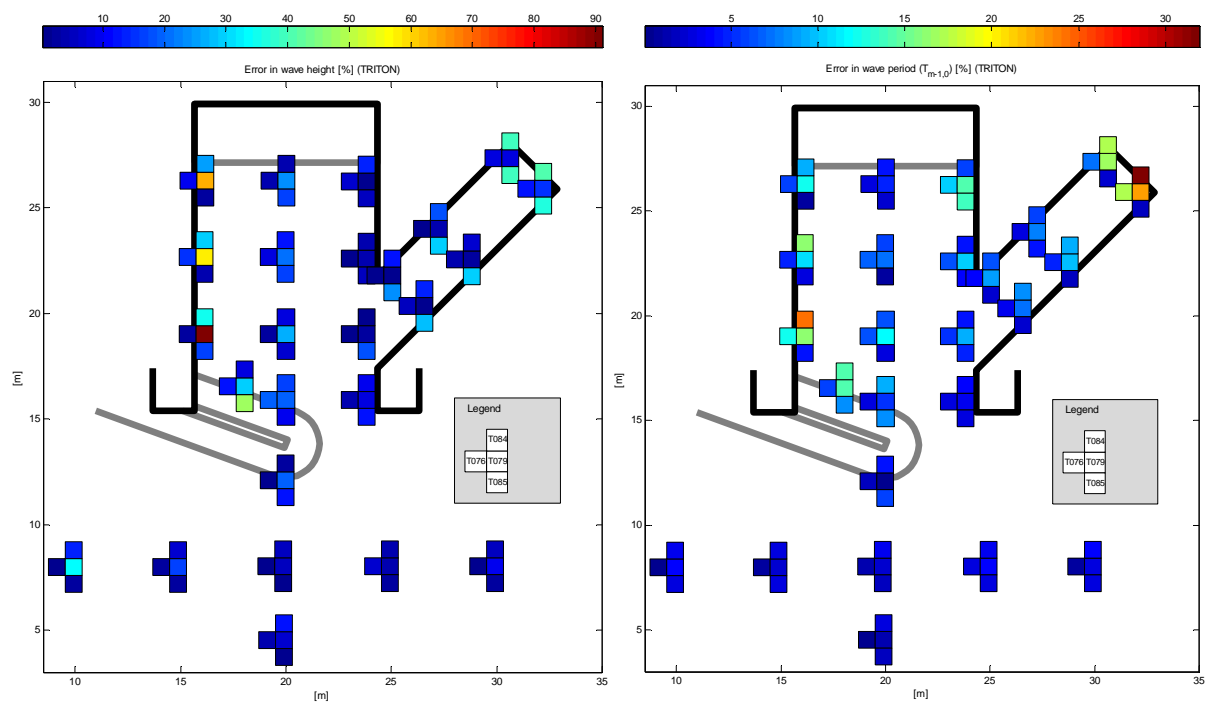


Figure 8.8 - Distribution of errors in TRITON model results. Left: significant wave heights. Right: mean wave periods ($T_{m-1,0}$)

Figure 8.8 also shows that the predicted wave heights for test T076 are very accurate. The average of the absolute error, at all 27 wave gauges, is only 5% in this case. For comparison, this error is on average 15% for the tests where higher waves are simulated. Another difference between the simulation of test T076 and the simulations of tests with higher waves is that only for the simulation of test T076 the bathymetry of the breakwater could be included, see Appendix A.

SWASH

Measured wave heights and wave periods are plotted against predicted wave heights and wave periods in Figure 8.9, showing good correlations.

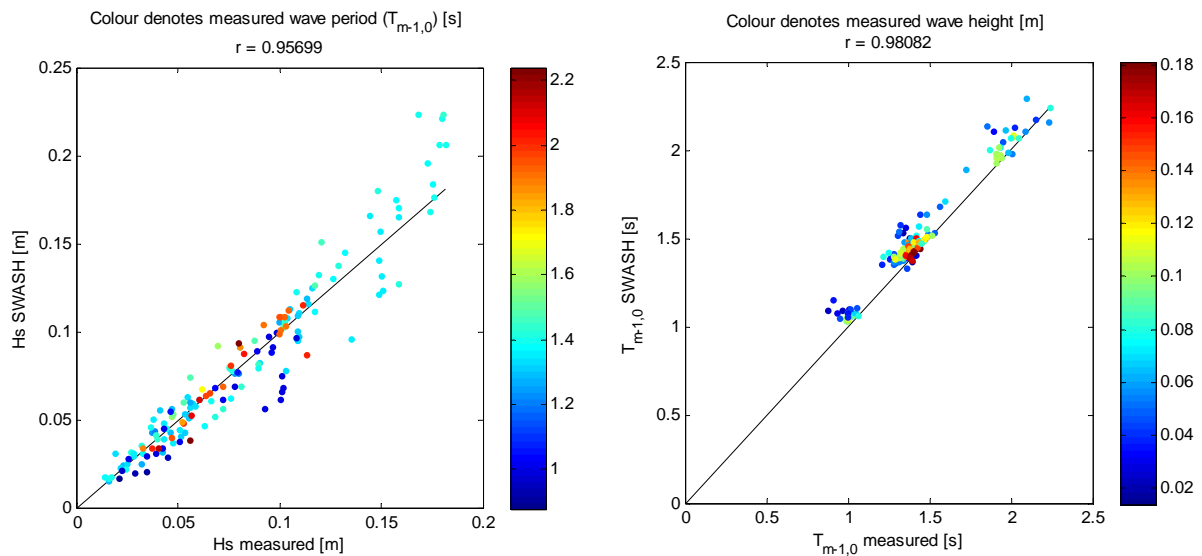


Figure 8.9 – Accuracy of SWASH model results. Left: significant wave heights. Right: mean wave periods ($T_{m-1,0}$)

The accuracy of the predicted wave heights seems to be related to mean wave period. The wave heights with large corresponding mean wave periods (i.e. those from test T085) are predicted most accurately. This shows the benefit of a higher grid resolution when nonlinear waves are modelled.

The simulations with SWASH are performed with the same horizontal grid resolution as the TRITON simulations. The vertical resolution of 2 layers is high enough to be of little influence compared to the horizontal resolution. Figure 8.7 and the discussion of it therefore apply here as well. This explains why, just as with TRITON, the mean wave periods are overestimated. It also explains why the wave heights with the smallest corresponding mean wave periods (i.e. those from test T084) are on average underestimated. Contrary to TRITON, a correlation is found between the number of grid cells per wave length and the accuracy of the simulation, see Table 8.1. Based on Table 8.1, a resolution of at least 40 grid cells per peak wave length appears to be sufficient.

Table 8.1 - Grid resolution and accuracy

	T084	T079	T085
Hs [m]	0.106	0.106	0.101
Tp	1.04	1.49	2.24
Cells per Wavelength	23	38	63
Average error [%]	17.5	9.8	8.6

Figure 8.10 shows how the errors in wave height and mean wave period vary throughout the domain. Most notable is that the errors in wave height in front of the harbour are sometimes quite large, relative to the errors in wave height inside the harbour.

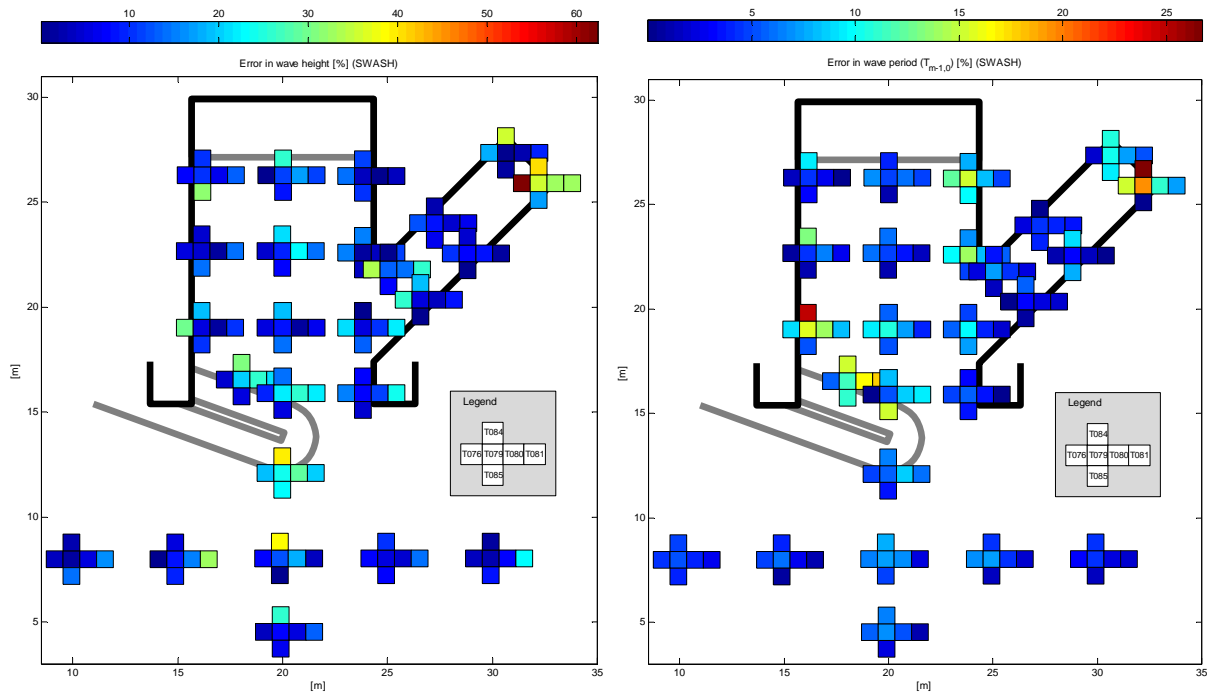


Figure 8.10 – Distribution of errors in SWASH model results. Left: significant wave heights. Right: mean wave periods ($T_{m-1,0}$)

8.1.3 Sensitivity of results from numerical simulations

The largest sensitivity in the PHAROS and TRITON simulations is expected to be in the choice of reflection coefficients. SWASH does not require these reflection coefficients since it works with so called porous structures, for which a porosity and stone diameter must be prescribed.

To obtain insight in the sensitivity towards reflection coefficients, some additional PHAROS simulations are carried out. In these simulations the reflection coefficients of the vertical concrete walls are changed from 100% to 80%. The results of these additional simulations are presented in the right panel of Figure 8.11. The left panel of Figure 8.11 contains the results from the original simulations.

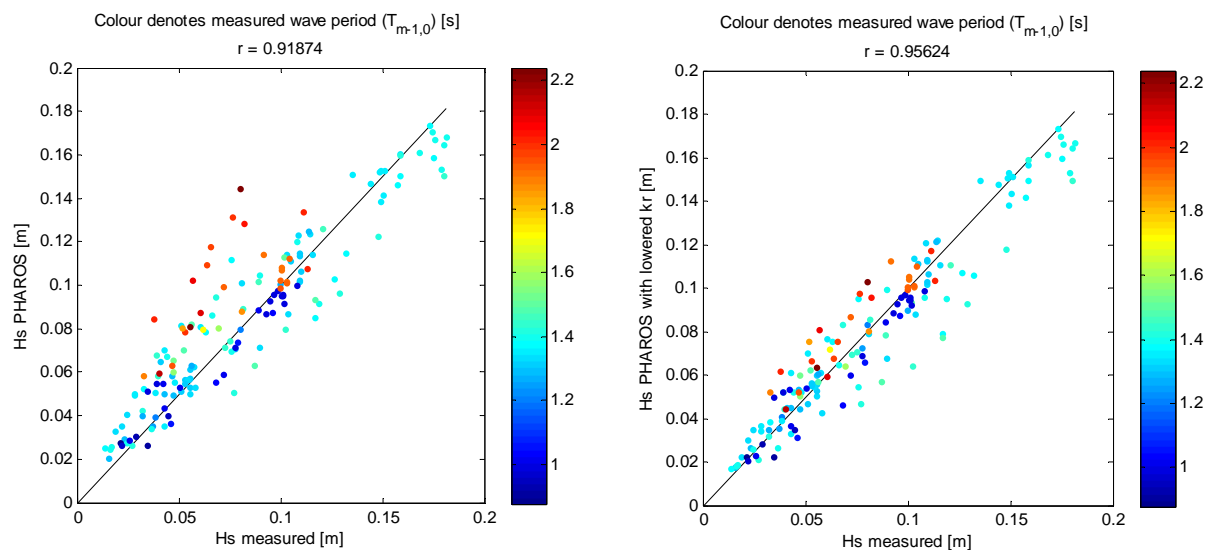


Figure 8.11 – 100% reflection (left) versus 80% reflection (right) at the walls

Figure 8.11 shows that the amount of overestimation has reduced considerably due to the lowering of the reflection coefficient of the concrete wall, especially for the longer period waves. It seems that while the breakwater is preventing most of the incoming wave energy to penetrate into the harbour, the wave energy that does enter the harbour reflects multiple times on the vertical walls. This “sloshing” could amplify the (standing) wave heights in the areas behind the breakwater, explaining the sensitivity of the reflection coefficient. Similar behaviour, although less pronounced, can be expected for the TRITON simulations. This is not verified in view of time.

The concrete walls in SWASH are schematised as a “porous structure” with a porosity of 0.1% and a stone diameter of one millimetre. Based on experience it is not expected that the simulations are sensitive to small variations in porosity of stone diameter. When the porosity and stone diameter would be increased with two orders of magnitude the simulations will of course be different, but these values would no longer be representative for concrete.

8.1.4 Conclusion

Results from computations with PHAROS are a bit conservative for non-breaking waves. The more nonlinear wave conditions are simulated more accurately with this linear model, in this specific case. This behaviour is ascribed to wave breaking and the handling of it by PHAROS. A sensitivity analysis shows that the model results can be quite sensitive to the reflection coefficients that are assigned to the vertical concrete walls that border the areas sheltered from direct wave attack. Lowering these reflection coefficients reduces the computed wave heights inside the port, improving simulation results for waves with low height and steepness.

The TRITON simulations resemble the scale model tests fairly well. The largest deviations are found in the high frequency part of the spectrum, but this is shown to be related to an insufficient resolution of a computational grid. However, modelling large waves with TRITON proved to be problematic. These simulations kept crashing, despite several attempts to prevent this by adjusting model settings and schematisations.

The significant wave heights and mean wave periods predicted by SWASH correspond pretty well with the measurements, for all considered wave conditions. Since the SWASH simulations were carried out with the same grid resolution as the TRITON simulations, similar issues with the simulation of test T084 could be expected and were observed.

8.2 Low frequency waves and harbour oscillations

In this section, harbour oscillations modelled by PHAROS, TRITON and SWASH are analysed and compared to the measured harbour oscillations in the scale model. The same methods are used as in the analysis of the scale model results in Section 7.2. Information about the modelled wave conditions can be found in the previous chapter as well.

First, the model results are presented. The accuracy of the model predictions is treated in the subsequent section.

8.2.1 Results from numerical simulations

PHAROS

The so called “seiching module” of PHAROS is used to compute the response of the harbour to long crested waves with frequencies in the range 0.007 – 0.3 Hz. Within the same frequency ranges that are used in describing the harbour oscillations in the scale model, the maximum amplitude response factor is selected. The obtained amplitude response factor is then multiplied with the significant wave height of the imposed water level time series in the considered frequency range. The predicted amplitudes of the harbour oscillations that are obtained in this manner are provided in Figure 8.12.

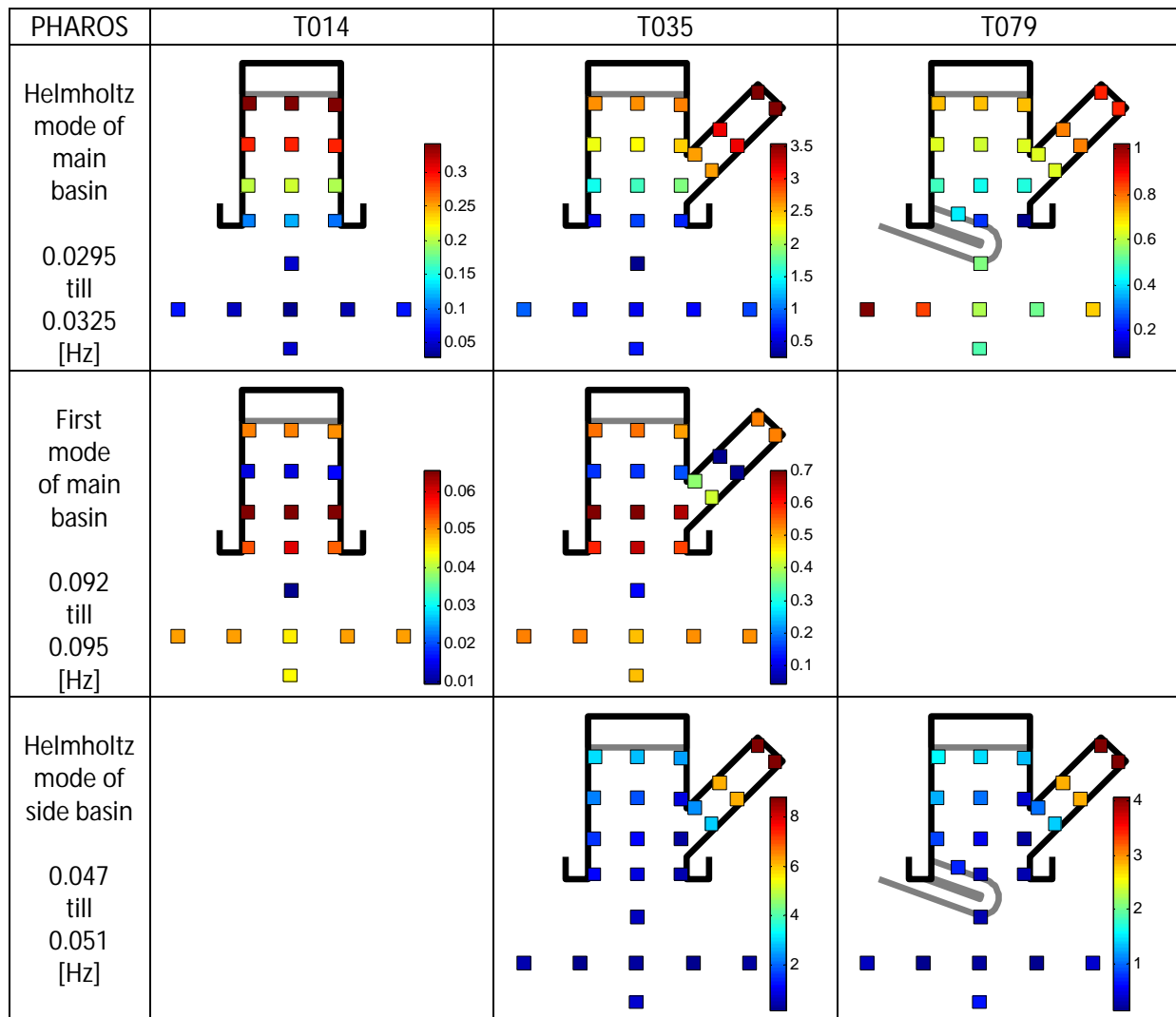


Figure 8.12 – Harbour oscillations computed with PHAROS (significant wave heights in millimetres)

Qualitatively the harbour oscillations match very well, the same modes are found. The computed amplitudes are however not very accurate. The oscillations in the main basin are underestimated while the Helmholtz mode (also known as zeroth mode or pumping mode) of the side basin is overestimated.

TRITON

The total low frequency wave energy and the harbour oscillations as obtained from the TRITON simulations are presented in Figure 8.13. The total amount of low frequency wave energy in tests T035 and T079 is predicted quite accurately, while for T014 it is overestimated with 50%. The amplitudes of the harbour oscillations are however underestimated in the majority of cases.

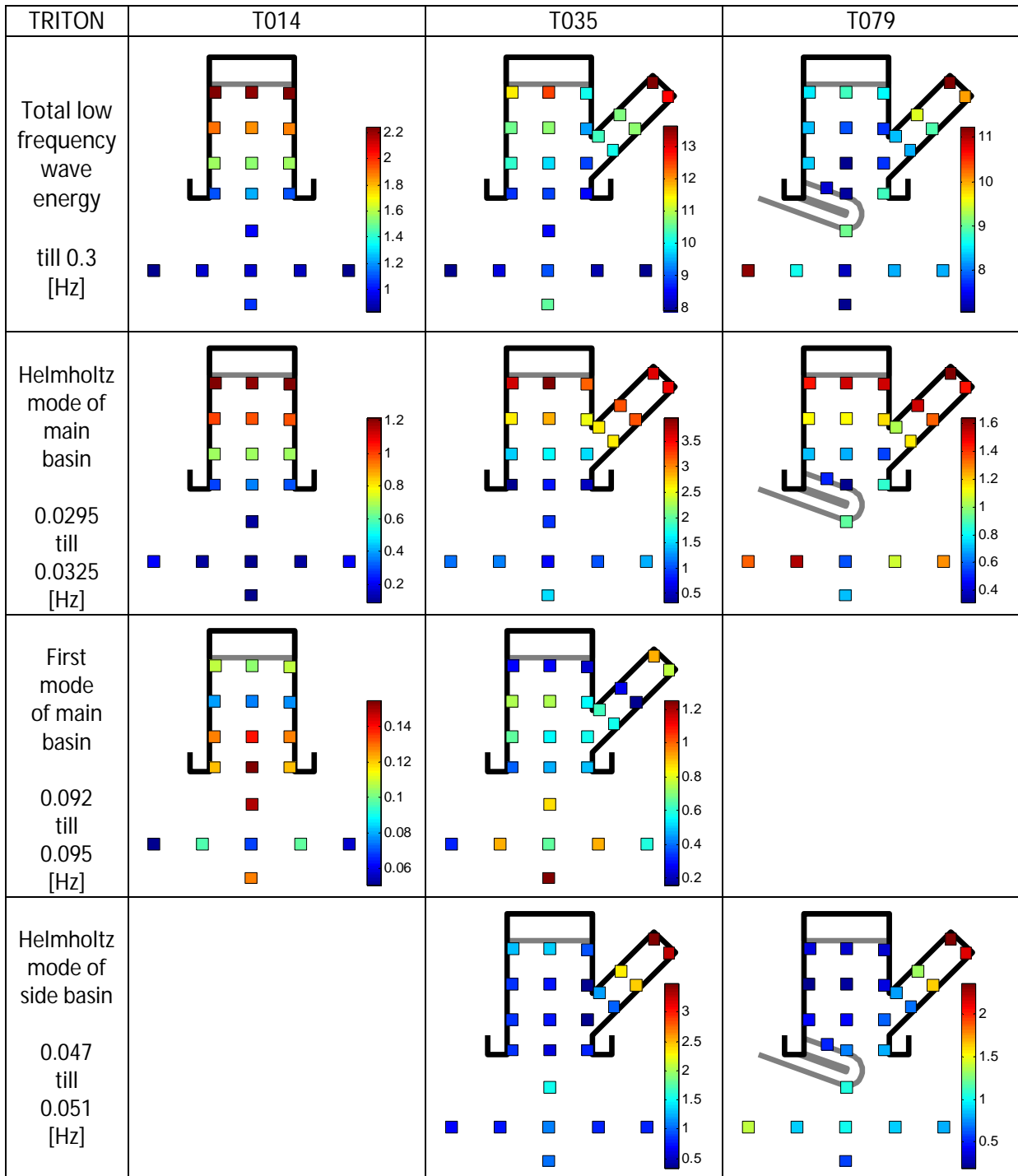


Figure 8.13 – Harbour oscillations computed with TRITON (significant wave heights in millimetres)

SWASH

The total low frequency wave energy and the harbour oscillations as obtained from the SWASH simulations are presented in Figure 8.14. The total low frequency wave energy appears to be overestimated somewhat. Most of the harbour oscillations are reproduced reasonably accurate nonetheless.

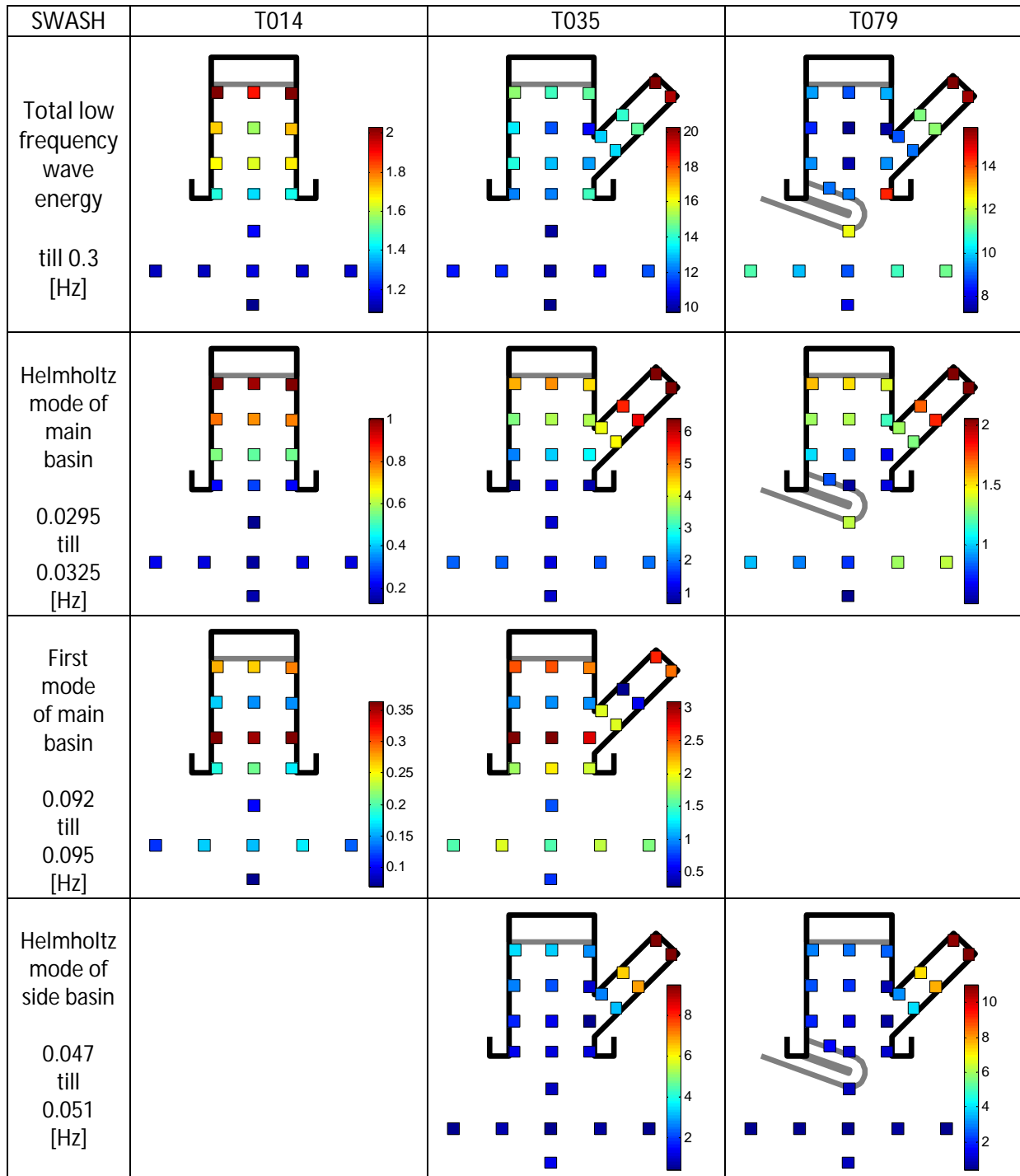


Figure 8.14 – Harbour oscillations computed with SWASH (significant wave heights in millimetres)

The Helmholtz mode of the side basin really stands out however. The amplitude of this oscillation is overestimated by a factor of about 4.

8.2.2 Accuracy of the numerical simulations

The total low frequency wave energy is modelled quite accurately by TRITON, as is shown in the left graph of Figure 8.15. SWASH overestimates the total low frequency wave energy with approximately 20%, see the right graph of Figure 8.15.

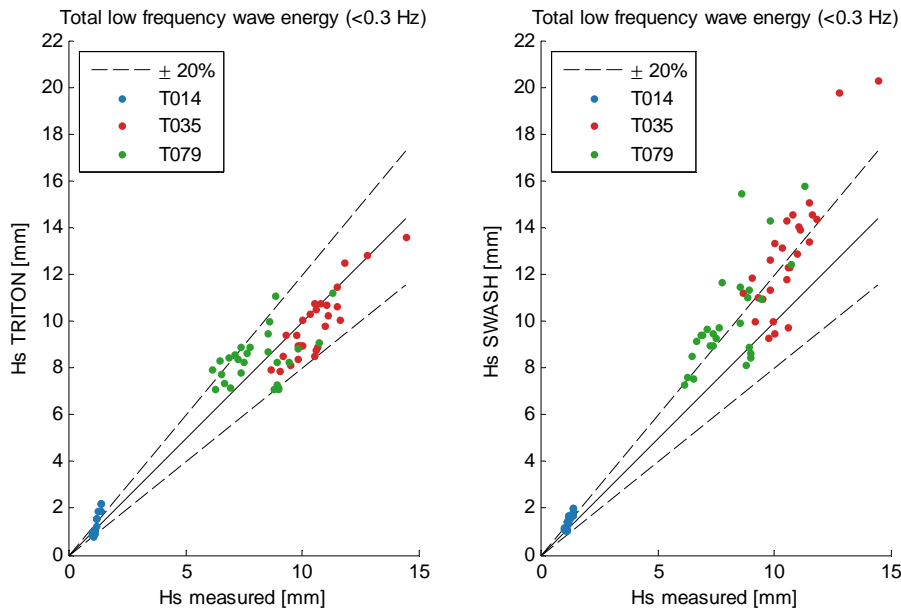


Figure 8.15 – Total low frequency wave energy

In Figure 8.16 the computed harbour oscillation amplitudes are plotted against the measured harbour oscillations amplitudes. Colours are used to distinguish the different harbour modes. This shows that all models compute the Helmholtz mode in the main basin with reasonable accuracy.

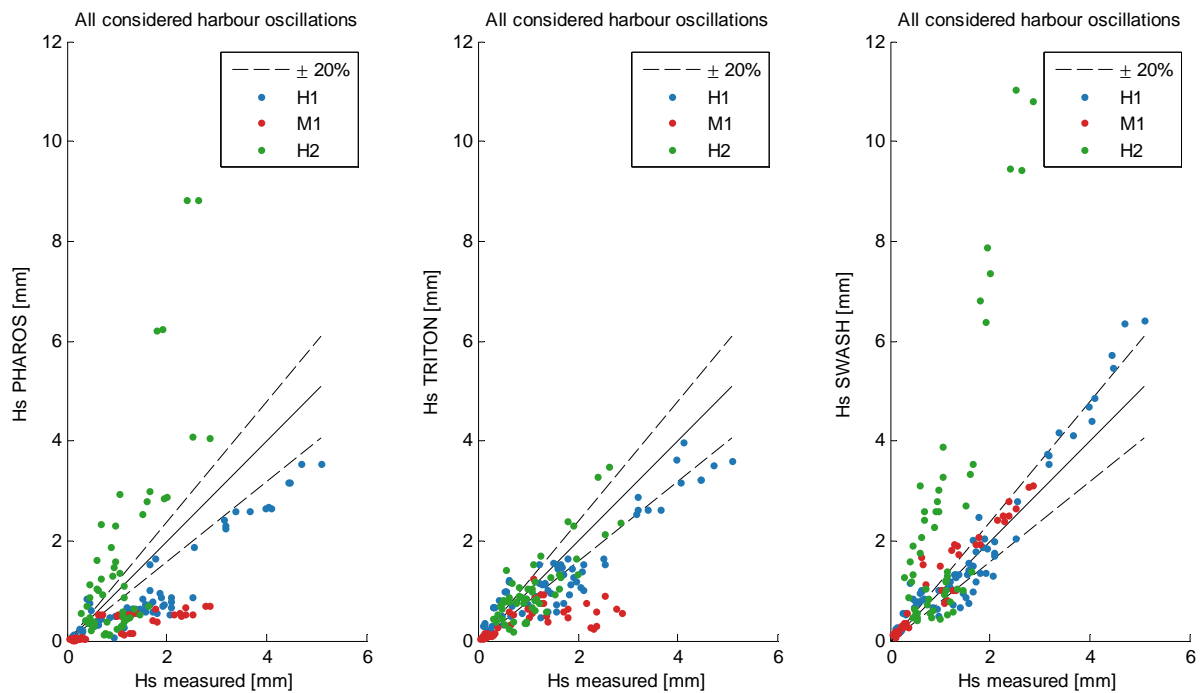


Figure 8.16 - Amplitudes of harbour oscillations (H1=Helmholtz mode in main basin, M1=first mode in main basin and H2=Helmholtz mode in side basin)

The first mode in the main basin is however only computed accurately by SWASH. PHAROS and TRITON underestimate the amplitude of this mode with a factor of about 3.

The Helmholtz mode of the side basin is on the other hand only predicted correctly by TRITON. PHAROS and SWASH overestimate this mode with a factor of approximately 4.

The underestimation by PHAROS cannot be caused by reflection coefficients or bottom friction, since all boundaries are modelled as 100% reflective and no bottom friction is included. The amplitude of the harbour oscillations from PHAROS are based on the low frequency energy of the imposed waves. The generation of additional low frequency wave energy inside the model domain is therefore not taken into account (PHAROS is a linear model).

Bottom friction is added to SWASH models to investigate the effect of extra energy dissipation mechanisms on the (over)estimation of Helmholtz mode in the side basin. With a Manning coefficient of 0.019 the amplitude of this mode in test T079 decreases with 20%. Adding bottom roughness with a Manning coefficient of 0.06 halves the amplitude in test T035. This shows that only a high amount of bottom friction significantly decreases the amplitude of the Helmholtz mode in the side basin. The overestimation of the Helmholtz mode in the side basin is thus not caused by a lack of bottom friction in the numerical model. This is in line with the expectation that the amount of energy radiating out of the harbour is larger than the amount of energy being dissipated through bottom friction.

8.2.3 Conclusion

Qualitatively all considered harbour oscillations are modelled correctly by all models. The quantitative predictions are accurate in about half of the considered cases. One case for which the amplitudes are computed quite accurately (mean errors of about 20%) by all models is the case of a Helmholtz mode in a basin with a gravel slope.

The differences between the measured and the computed harbour oscillation amplitudes in the other cases can be quite large, up to a factor 4. If no damping is included in the basin at all, one can expect numerical models to overestimate the amplitude of a Helmholtz mode. TRITON however appears to be less sensitive to this, still yielding reasonable results in these cases. The amplitudes corresponding to higher modes are generally underestimated. SWASH appears to be an exception to this, as it remained quite accurate.

9 Conclusions and recommendations

9.1 Conclusions

The objectives of this thesis are:

- To compare numerical models for the use of wave propagation in harbours.
- To produce a dataset, through physical modelling, from which wave propagation in harbours can be studied and numerical models can be benchmarked.
- To determine application boundaries of operational numerical wave models for wave penetration in harbours.

A study on wave processes in harbours shows that reflection, diffraction, shoaling and harbour oscillations are most relevant for wave propagation in harbours. A numerical wave model should thus be able to compute these processes accurately and efficiently to be useful in harbour contexts. From an investigation of existing wave models it is concluded that mild-slope models, Boussinesq-type models and non-hydrostatic models are therefore the most suitable for modelling wave penetration in harbours.

PHAROS (a mild-slope model), TRITON (a Boussinesq-type model) and SWASH (a non-hydrostatic model) are studied in more detail. It is demonstrated that these models are all capable of accurately reproducing analytical solutions for linear shoaling and diffraction.

To be able to study the performance of operational numerical wave models in scenarios that are more realistic than analytical benchmark test cases, a physical modelling approach is taken. The physical model:

- Is designed to represent a typical seaport.
- Includes three different layouts with varying complexity.
- Includes reflection, diffraction, refraction, transmission and harbour oscillations.
- Is subjected to a large variety of wave conditions.

A selection of physical model tests is simulated with PHAROS, TRITON and SWASH. The following conclusions are drawn from a comparison between numerical model results and scale model measurements.

Regarding primary waves

- Wave fields with significant wave breaking are modelled remarkably well by PHAROS (being a linear model). Errors in wave height are on average below 15%.
- Wave heights predicted by PHAROS, in areas which are sheltered from direct wave attack by obstacles such as breakwaters and are enclosed by highly reflective boundaries, can be very conservative and sensitive towards assigned reflection coefficients. Overestimations in excess of 50% are possible, while errors are on average about 25%.
- TRITON and SWASH are more accurate than PHAROS in these situations. The found errors in wave height are on average less than 15%, for all considered wave conditions. These models are therefore considered capable of modelling the penetration of primary waves in harbours.

- SWASH has practically no application boundary in terms of maximal wave height. Even waves with a height of half the water depth, which is considered a very extreme scenario for ports, are still modelled within an average accuracy of 15%.
- The area of application of TRITON is limited to waves with a significant wave height of up to a quarter of the water depth. Numerical instabilities are encountered for larger ratios of wave height over water depth.

Regarding harbour oscillations

- The total amount of low frequency wave energy modelled by TRITON and SWASH corresponds pretty well with measurements from the physical model. For PHAROS this comparison is not made.
- PHAROS, TRITON and SWASH are all able to reproduce seven harbour modes (standing wave patterns) that are selected from observations in the physical model.
- In half of the cases, the amplitudes of harbour oscillations are predicted within an accuracy of about 20%.
- In the other cases however, large deviations are found between measured and computed amplitudes. SWASH overestimates the Helmholtz mode of a certain basin with a factor 3-4 while TRITON underestimates the first mode of another basin with a factor 3. PHAROS shows both these discrepancies.

The following conclusions are drawn about the choice of wave model for simulating wave penetration in ports for engineering purposes.

- Its computational efficiency and robustness makes PHAROS the most appropriate tool for obtaining a quick estimate of wave heights in ports. Analysing the sensitivity of reflection coefficients is indispensable though for obtaining reliable results.
- When more accurate predictions (errors < 15%) are required, more confidence is placed in TRITON and SWASH. SWASH is strongly preferred over TRITON, because of stability problems encountered with the latter model. Moreover, the schematisation of structures commonly found in ports (e.g. breakwaters) is more straightforward using SWASH and computational times are significantly lower.

9.2 Recommendations

Further research on the modelling of harbour oscillations with TRITON and SWASH is recommended.

- Investigate the modelling of bound long waves and the possible occurrence of spurious free waves at the model boundaries. Scale model tests with bichromatic wave conditions are available for this.
- Investigate the possibilities for obtaining more insight in the influence of porous structures on the amplitudes of harbour oscillations in SWASH.

For future studies regarding the performance of numerical wave models in harbours using physical model tests, it is recommended to investigate the possibilities of including a bathymetry (e.g. a foreshore) in the physical model. The effects of shoaling and refraction on wave penetration in harbours, and the numerical simulation thereof, could then be included as well.

10 References

- Battjes, J.A. "Surf similarity." *Proc. 14th Conf. on Coastal Eng.* Copenhagen: ASCE, New York, 1974. 466-480.
- Berkhoff, J.C.W. "Computation of combined refraction-diffraction." *Proc. 13th Int. Conf. Coastal Engineering*, 1972: 471 - 490.
- Berkhoff, J.C.W. *Mathematical Models for Simple Harmonic Linear Water Waves*. Phd Thesis, Delft: Delft University of Technology, 1976.
- Berkhoff, J.C.W., N. Booij, and A.C. Radder. "Verification of numerical wave propagation models for simple harmonic linear water waves." *Coastal Engineering* 6, no. 3 (1982): 255-279.
- Biesel, F. "Les appareils générateurs de houle en laboratoire." *La houille blanche*, 1951.
- Boeyinga, J. *Boussinesq-type wave modelling in port applications*. MSc Thesis, Delft University of Technology, 2010.
- Booij, N. "A note on the accuracy of the mild-slope equation." *Coastal Engineering* 7, no. 3 (1983): 191-203.
- Booij, N., R.C. Ris, and L.H. Holthuijsen. "A third-generation wave model for coastal regions, Part I, Model description and validation." *Journal of Geophysical Research: Oceans* 104, no. C4 (1999): 7649-7666.
- Borsboom, M.J.A. *A Boussinesq-type wave model with improved linear and nonlinear behaviour (Report H3203.51/X0231.40)*. Delft: WL | Delft Hydraulics, 1998.
- Borsboom, M.J.A., J. Groeneweg, N. Doorn, and M.R.A. Van Gent. *Boundary conditions for a 2D Boussinesq-type wave model (Ref: H3581)*. Delft: WL | Delft Hydraulics, 2000.
- Borsboom, M.J.A., J. Groeneweg, N. Doorn, and M.R.A. Van Gent. "Flexible boundary conditions for a Boussinesq-type wave model." *Int. Symp. Waves 2001*. San Francisco: ASCE, 2001. 884-893.
- Borsboom, M.J.A., N Doorn, J Groeneweg, and M.R.A. Van Gent. "A Boussinesq-type wave model that conserves both mass and momentum." Sydney: ASCE, proceedings of the 27th ICCE Conference, 2000.
- Borsboom, M.J.A., N. Doorn, J. Groeneweg, and M.R.A. Van Gent. "Nearshore wave simulations with a Boussinesq-type model including breaking." Lund, Sweden: Proc. Coastal Dynamics, ASCE, 2001. 759-768.
- Boshek, M.R. *Reflection and Diffraction Around Breakwaters*. MSc Thesis, Delft: Delft University of Technology, 2009.
- Caires, S. *Investigation of the influence of a low-tide terrace on wave loads using TRITON (ref: H5121)*. Delft: Deltares, 2009.
- Casulli, V., and G.S. Stelling. "Numerical simulation of 3D quasi-hydrostatic, free-surface flows." *Journal of Hydraulic Engineering* 124, no. 7 (1998): 678-686.

- De Bont, J.A.M. *Evaluation of a higher order extension of the Boussinesq-type model TRITON - Generation of bound low-frequency waves (Ref: 1202340-000-HYE-0001)*. Delft: Deltares, 2010.
- De Jong, M.P.C., and M.J.A. Borsboom. "A practical post-processing method to obtain wave parameters from phase-resolving wave model results." *International Journal of Ocean and Climate Systems* (Multi-Science Publishing) 3, no. 4 (2012): 203–216.
- De Jong, M.P.C., and M.J.A. Borsboom. *sHallow WAter Initiative (HAWAI), WP1: Nearshore wave modelling - Task A and B: Overview of numerical wave models in coastal engineering and their relevance to shallow water LNG activities (Project nr. H4643)*. Delft: WL | Delft Hydraulics, 2007.
- Dean, R.G. "Relative validities of water wave theories." *Journal of the Waterways, Harbors and Coastal Engineering Division* 96, no. 1 (1970): 105-119.
- Dean, R.G., and R.A. Dalrymple. *Water Wave Mechanics for Engineers and Scientists*. Singapore: World Scientific, 1984.
- Deltares. "Memo: 2nd Order Higdon-Boundary-Condition in PHAROS (Ref: 1202340-000-HYE-0003)." Delft: Deltares, 2010.
- Deltares. "Memo: Benchmark tests Harbour models, proposal update (Ref: 1209490-002-HYE-0001)." Delft: Deltares, 2014.
- Deltares. *PHAROS - User & Technical Manual - Version 9.11.19731 - 11 May 2013*. Delft: Deltares, 2013.
- Deltares. *r-DPRA tool - User & Technical Reference - Version: 1.01.00 - 3 September 2013*. Delft: Deltares, 2013.
- Deltares. *Triton 1.0 - User and technical manual version 1.0*. Delft: Deltares, 2008.
- Demirbilek, Z., A. Zundel, and V. Panchang. "Benchmark tests for harbor wave agitation models." *Building on the Past, Respecting the Future*. Ports 2010. 12th Triannual International Conference. Building on the Past, Respecting the Future, 2010.
- Demirbilek, Z., and V. Panchang. *CGWAVE: A Coastal Surface Water Wave Model of the Mild Slope Equation*. Vicksburg: U.S. Army Corps of Engineers Waterways Experiment Station, 1998.
- Dingemans, M.W. *Water wave propagation over uneven bottoms*. PhD Thesis, Delft: Delft University of Technology, 1994.
- Goda, Y., T. Takayama, and Y. Suzuki. "Diffraction diagrams for directional random waves." *Proc. 16th Conf. Coastal Engineering (ASCE)*, 1978: 628-650.
- Groeneweg, J., N. Doorn, M.J.A. Borsboom, and M.R.A. Van Gent. "Boussinesq-type modeling of measured wave breaking on a circular shoal." Cardiff, Wales: Proc. 28 th ICCE Conference, ASCE, 2002. 495-507.

- Holthuijsen, L.H. *Waves in Oceanic and Coastal Waters*. Cambridge University Press, 2007.
- Homma, S. "On the behavior of seismic sea waves around circular island." *Geophysical Magazine* 21, no. 3 (1950): 199-208.
- Kirby, J.T. "Boussinesq models and applications to nearshore wave propagation, surfzone processes and wave-induced currents." In *Advances in coastal modeling*, edited by V.C. Lakhan, 1-41. Elsevier, 2003.
- Kirby, J.T., G. Wei, Q. Chen, A.B. Kennedy, and R.A. Dalrymple. *Funwave 1.0, fully nonlinear boussinesq wave model documentation and user's manual*. Center for Applied Coastal Research, University of Delaware, 1998.
- Kleefsman, K.M.T., G. Fekken, A.E.P. Veldman, B. Iwanowski, and B. Buchner. "A volume-of-fluid based simulation method for wave impact problems." *Journal of Computational Physics* 206, no. 1 (2005): 363-393.
- Klein Breteler, M. *Nieuwe Deltagoot, criteria voor schot en diepte. Meetrapport metingen in Oosterscheldegoot. (ref: 120493-002-OA-0004)*. Delft: Deltares, 2010.
- Klopman, G., M.W. Dingemans, and E. Van Groesen. "A variational approach to Boussinesq modelling of fully nonlinear water waves." *Journal of Fluid Mechanics* 657 (2010): 36-63.
- Kostense, J.K., K.L. Meijer, M.W. Dingemans, A.E. Mynett, and P. van den Bosch. "Wave energy dissipation in arbitrarily shaped harbours of variable depth." Tapei: Coastal Engineering, 1986. 2002 - 2016.
- Losada, I.J., J.L. Lara, R. Guanche, and J.M. Gonzalez-Ondina. "Numerical analysis of wave overtopping of rubble mound breakwaters." *Coastal Engineering* 55, no. 1 (2008): 47-62.
- Ma, G., F. Shi, and J.T. Kirby. "Shock-capturing non-hydrostatic model for fully dispersive surface wave processes." *Ocean Modelling* 43-44 (2012): 22-35.
- Madsen, P.A., and H.A. Schäffer. "Higher-order Boussinesq-type equations for surface gravity waves: derivation and analysis." *Philosophical Transactions of the Royal Society of London. Series A: Mathematical, Physical and Engineering Sciences* 356.1749 (356, no. 1749 (1998): 3123-3181.
- Mellink, B. *Numerical and experimental research of wave interaction with a porous breakwater*. MSc Thesis, Delft: Delft University of Technology, 2012.
- Nwogu, O.G. "Alternative form of Boussinesq equations for nearshore wave propagation." *Journal of waterway, port, coastal, and ocean engineering* 119, no. 6 (1993): 618-638.
- Nwogu, O.G. "Numerical prediction of breaking waves and currents with a Boussinesq model." Orlando: Proc. 25th Int.Conf. on Coastal Engineering, ASCE, 1996. 4807-4820.
- Nwogu, O.G., and Z. Demirbilek. *BOUSS-2D: A Boussinesq wave model for coastal regions and harbors - Report 1: Theoretical Background and User's Manual*. ERDC. CHL TR-01-25. Vicksburg, MS: US Army Engineer Research and Development Center, 2001.

- Peregrine, D.H. "Long waves on a beach." *Journal of fluid mechanics* 27, no. 04 (1967): 815-827.
- Rabinovich, A.B. "Seiches and harbour oscillations." In *Handbook of coastal and ocean engineering*, edited by Y.C. Kim, 193-236. Singapore: World Scientific, 2009.
- Reijmerink, S.P. *Golfrandvoorwaarden in havens: Bruikbaarheidsgrenzen voor (numerieke) modellen*. MSc Thesis, Delft: Delft University of Technology, 2012.
- Roelvink, D., A.J.H.M. Reniers, A. van Dongeren, J. Van Thiel de Vries, J. Lescinski, and R. McCall. *XBeach model description and manual*. Unesco-IHE Institute for Water Education, Deltares and Delft University of Technology, 2010.
- Schäffer, H.A., P.A. Madsen, and R. Deigaard. "A Boussinesq model for waves breaking in shallow water." *Coastal Engineering* 20, no. 3 (1993): 185-202.
- Smit, P.B., M. Zijlema, and G.S. Stelling. "Depth-induced wave breaking in a non-hydrostatic, near-shore wave model." *Coastal Engineering* 76 (2013): 1-16.
- Sommerfeld, A. "Mathematische theorie der diffraction." *Mathematische Annalen* 47, no. 2 (1896): 317-374.
- Sonneveld, P. "CGS, a fast Lanczos-type solver for nonsymmetric linear systems." *SIAM Journal on Scientific and Statistical Computing* 10, no. 1 (1989): 36-52.
- Stansby, P.K., and J.G. Zhou. "Shallow-water flow solver with non-hydrostatic pressure: 2D vertical plane problems." *International Journal for Numerical Methods in Fluids* 28, no. 3 (1998): 541-563.
- Stelling, G.S., and M. Zijlema. "An accurate and efficient finite-difference algorithm for non-hydrostatic free-surface flow with application to wave propagation." *International Journal for Numerical Methods in Fluids* 43, no. 1 (2003): 1-23.
- Stelling, G.S., and S.P.A. Duinmeijer. "A staggered conservative scheme for every Froude number in rapidly varied shallow water flows." *International Journal for Numerical Methods in Fluids* 43, no. 12 (2003): 1329-1354.
- The SWAN Team (Delft University of Technology). *SWAN User Manual - SWAN Cycle III version 40.91ABC*. 2007. <http://swanmodel.sourceforge.net> (accessed 2014).
- The SWASH Team (Delft University of Technology). *SWASH User Manual - SWASH version 2.0*. 2014. <http://swash.sourceforge.net> (accessed 2014).
- Tolman, H.L. *User manual and system documentation of WAVEWATCH III TM version 3.14*. Camp Springs: National Oceanic and Atmospheric Administration, 2009.
- Van der Hout, A., B. Wijdeven, and J. Schouten. *Overview of a PHAROS/TRITON/SWAN validation case study (Ref: 1200477-003-HYE-0001)*. Delft: Deltares, 2009.

- Van der Ven, P.P.D. *The use of numerical models to determine the response of moored vessels to waves in a complex harbour geometry*. MSc Thesis, Delft: Delft University of Technology, 2012.
- Van der Wel, M. *The behaviour of a moored oil tanker in the port of Leixões, Portugal*. MSc Thesis, Delft: Delft University of Technology, 2011.
- Van Dongeren, A., G. Klopman, A. Reniers, and H. Petit. "High-quality laboratory wave generation for flumes and basins." *Proc. of Waves*. San Francisco, California: ASCE, 2001. 1190-1199.
- Van Os, J. *R&D Harbours and ships 2009 - Validation of Pharos spectral, summation of components and other issues (Ref: 1200477-003-HYE-0002)*. Delft: Deltares, 2009.
- Wellens, P. *Higher-order non-linear extension of TRITON - Implementation and application to CoMibbs cases (ref: 1001770-000-HYE-0001)*. Delft: Deltares, 2010.
- Wenneker, I. "Stroke, velocity and acceleration requirements for piston-type wave generators." Gent, Belgium: Proceedings on the Fourth International Conference on the Application of Physical Modelling to Port and Coastal Protection (Coastlab), 2012.
- WL | Delft Hydraulics. *Version 6.1 - PHAROS - Wave disturbance in harbours - Examples of application - March 1991*. Delft: WL | Delft Hydraulics, 1991.
- Xu, B., V. Panchang, and Z. Demirbilek. "Exterior reflections in elliptic harbor wave models." *Journal of waterway, port, coastal, and ocean engineering* 122, no. 3 (1996): 118-126.
- Zanuttigh, B., and J.W. Van der Meer. "Wave reflection from coastal structures." *Int. Conf. Coast. Eng.* San Diego, USA: ASCE, 2006. 4337-4349.
- Zijlema, M., and G.S. Stelling. "Efficient computation of surf zone waves using the nonlinear shallow water equations with non-hydrostatic pressure." *Coastal Engineering* 55, no. 10 (2008): 780-790.
- Zijlema, M., and G.S. Stelling. "Further experiences with computing non-hydrostatic free-surface flows involving water waves." *International journal for numerical methods in fluids* 48, no. 2 (2005): 169-197.
- Zijlema, M., G.S. Stelling, and P.B. Smit. "SWASH: An operational public domain code for simulating wave fields and rapidly varied flows in coastal waters." *Coastal Engineering* 58, no. 10 (2011): 992-1012.

Appendix A Numerical model set-ups

A.1 Introduction

The scale model tests are simulated with the numerical wave models PHAROS, TRITON and SWASH. Whenever possible, the same choices are made for model parameters and schematisations with these three different models.

Two versions of the breakwater are included in the numerical simulation. Version one resembles the original breakwater, while the second version resembles the deformed breakwater (deformed after wave attack, occurring mainly during test T081). The difference between these two versions is shown in Figure A.1. The underwater slope of the deformed breakwater is flatter while the part above the water surface has become steeper. At the head of the breakwater some material was displaced, creating a kind of hockey stick shape. Tests T076, T079 and T081 are simulated with breakwater version one while tests T080, T084 and T085 are simulated with version two.

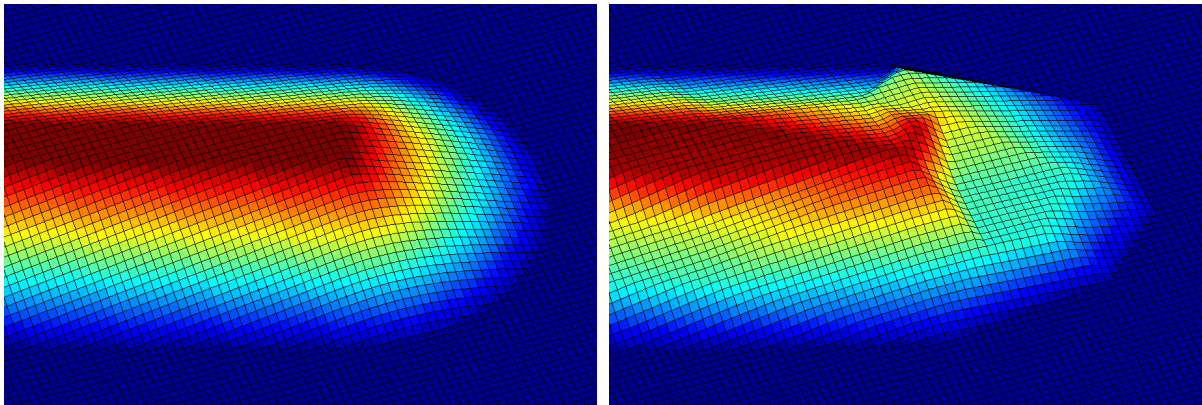


Figure A.1 - Original breakwater (left) and deformed breakwater (right). Camera viewpoint is outside the port, all scales are the same.

A.2 PHAROS model set-up

A.2.1 Spectral computations

Scale

Scaling the physical model appeared to be necessary for stability reasons. A scale of 1:45 has been adopted, meaning that all dimensions in the numerical model are 45 times larger than in the physical model. Froude scaling is applied to scale the wave periods.

Model layout

The model layout is shown in Figure A.2. The model boundaries are located at the still water line.

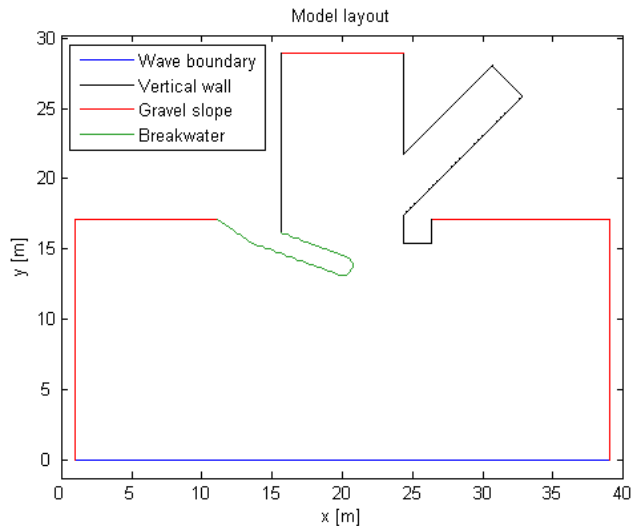


Figure A.2 – Model layout

Bathymetry

Only the bathymetry of the breakwater is included in the models, because only here diffraction and refraction takes place. A minimal water depth of 9 cm (on model scale) is maintained.

Wave excitation

Jonswap spectra are imposed at the wave boundary. The spectra are approximated using 11 wave periods, each one representing approximately 10% of the energy in the spectrum. The wave periods are listed in Table A.1. The peak periods are a factor $\sqrt{45}$ larger than the peak periods in the physical model, due to scaling.

Table A.1 – Imposed wave conditions

	T076	T079	T080	T081	T084	T085
H_s [m]	2.3445	4.7556	7.1388	9.6168	4.7882	4.5539
T_p [s]	9.9952	9.9952	9.9952	9.9952	6.9765	15.0264
Wave periods [s]	5	5	5	5	3.5	8
	6	6	6	6	4.2	9.1
	7	7	7	7	5	11
	8.3	8.3	8.3	8.3	5.8	12.5
	9	9	9	9	6.2	13.5
	9.5	9.5	9.5	9.5	6.6	14.2
	9.8	9.8	9.8	9.8	6.8	14.7
	10	10	10	10	7	15
	10.5	10.5	10.5	10.5	7.3	15.8
	11.2	11.2	11.2	11.2	7.8	16.9
	12	12	12	12	8.1	18

Boundaries

The determination of reflection coefficients is treated in Appendix C. The following reflection coefficients are assigned to the boundaries shown in Figure A.2:

Vertical concrete walls: 100%

Gravel slopes: 20%
Breakwater: 30%

Wave breaking

Wave breaking is included in all simulations. The default values have been used for the model parameters that control wave breaking ($\gamma_d=0.14$, $\alpha=1$ and $\gamma_s=0.8$).

Bottom friction

No bottom friction is included.

Grid resolution

The shortest wave period to be modelled is determining the choice of grid resolution. Triangular grids containing 12 nodes per wavelength (for this shortest wave) are applied.

A.2.2 Seiching computations

These simulations only differ in bathymetry, boundary conditions and grid resolution.

Bathymetry

No bathymetry is included for the seiching computations.

Boundaries

For the seiching computations, all boundaries are modelled as fully reflective (except for the wave boundary of course).

Grid resolution

The CGS solver is not available for seiching computations in PHAROS, so the direct solver must be used. This means the total amount of grid cells is limited to approximately 20,000. The grids for the seiching computations have a resolution of 15 – 20 cm (model scale).

A.3 TRITON model set-up

Scale

All simulations are carried out on the same scale as the physical model, to avoid scale effects.

Model layout

The model layout is the same as the model layout in PHAROS, see Figure A.2. All boundaries are again located at the still water line.

Bathymetry

Unfortunately, bathymetry could not always be included due to issues with numerical stability. Table A.2 provides an overview of which part of the bathymetry is included in which simulation. Slope schematisation C from Figure 4.1 is applied, the minimal water depth in the domain is limited to 14cm.

Table A.2 - Bathymetry included in each simulation

Test	Breakwater bathymetry included?	Gravel slope bathymetry included?
T014	-	Yes
T035	-	No
T076	Yes	Yes
T079	No	No
T084	No	No
T085	No	No

Wave excitation

Time series of surface elevations are imposed at the wave boundary. These time series are computed from the motions of the wave board, to make sure the numerical model has the same realisation of the Jonswap spectrum as the physical model and second order steering is accounted for. An elaboration on the generation of these time series can be found in Appendix B.

Boundaries

The determination of reflection coefficients is treated in Appendix C. The following reflection coefficients are assigned to the boundaries shown in Figure A.2:

Vertical concrete walls:	100%
Gravel slopes:	20%
Breakwater:	30%

Wave breaking

No wave breaking is included.

Bottom friction

No bottom friction is included (Chezy roughness is set to 1000).

Grid resolution

A rectangular grid with a resolution of 7 cm is used for all simulations, resulting in 38 cells per peak wavelength for simulations with a 1.49 second peak period. This resolution was chosen as a compromise between accuracy and computational time. Computations took approximately a week on a 64-bit Windows computer with an Intel i7-2600 CPU at 3.4GHz and 16 GB RAM.

Time step

A time step of 0.035 seconds is chosen for all simulations. The number of time steps per peak wave period is thus 29.7 for test T084, 64 for test T085 and 42.6 for all other tests. The Courant number satisfies TRITON's stability criterion:

$$Cr = \left(\frac{|u|+c}{\Delta x} + \frac{|v|+c}{\Delta y} \right) \Delta t = 2 * \frac{2.08}{0.07} * 0.035 = 2.08 \leq 2\sqrt{2}$$

Other modelling parameters

Other modelling parameters can be found in the TRITON input files, which are included in Appendix E.

A.4 SWASH model set-up

Scale

All simulations are carried out on the same scale as the physical model, to avoid scale effects.

Model layout

The layout of the physical model, as presented in Figure 5.4, is carefully reconstructed. All slopes in bathymetry have the correct steepness. The stone diameters for the gravel slopes and breakwater are taken from Table 5.4 and the porosity was taken equal to 0.4. The vertical walls are modelled as porous structures with a stone diameter of 1 millimetre and a porosity of 0.001.

Bathymetry

The complete bathymetry of the physical model is included using porous layers.

Wave excitation

Time series of surface elevations are imposed at the wave boundary. These time series are computed from the motions of the wave board, to make sure the numerical model has the same realisation of the Jonswap spectrum as the physical model and second order steering is accounted for. An elaboration on the generation of these time series can be found in Appendix B.

Boundaries

No internal boundaries are specified since these follow from the bathymetry. The outer boundaries (located at the edges of the grid) are modelled as closed. These boundaries represent the borders of the wave basin (which consist of concrete walls).

Bottom friction

No bottom friction is included.

Grid resolution

A rectangular grid with a horizontal resolution of 7 cm and two vertical layers are used for all simulations. This results in 38 horizontal cells per peak wavelength for simulations with a 1.49 second peak period. This resolution was chosen as a compromise between accuracy and computational time. Each computation took approximately 2 days on a 64-bit Windows computer with an Intel Xeon E5-2670 0 CPU @ 2.6GHz and 32 GB RAM.

Time step

A maximum Courant number of 0.5 was specified for accuracy and stability reasons because high waves are simulated. This results in a time step of 0.01 or 0.005 seconds, depending on the wave conditions.

Other modelling parameters

A momentum conservative scheme is applied to mimic the effects of wave breaking. Further details and other modelling parameters can be found in the SWASH command file, which is included in Appendix F.

Appendix B Generation of surface elevation time series from wave board motions

The waves in the physical model are generated based on a prescribed wave spectrum, using second order wave board steering. This second order steering is required for accuracy reasons since the generated waves are in some cases highly nonlinear. Second order steering prevents or significantly reduces the occurrence of spurious wave components, by including bound low frequency waves and super harmonics in the wave board motion.

Numerical wave models usually require the specification of water surface elevation at the wave boundary. For accurate representation of the physical model, the same realisation of the imposed wave spectrum must be imposed, including the second order corrections. Unfortunately, the software used at the test facility, which computes the wave board motions from a prescribed wave spectrum, does not provide a time series of surface elevations that are generated.

Time series of wave board displacement can be obtained however. This signal is created before the experiment starts, so it does not include the displacements due to active reflection compensation. These time series are used to derive water surface elevation time series from, that can be imposed on the numerical models.

A piston-type wave board has been used to generate the waves in the scale model. An analytical solution for the relation between the motions of such a wave board and water surface elevations can be derived based on linear wave theory. This solution, the so called Biésel transfer function, is given by Biésel (1951):

$$\frac{H}{S_0} = \frac{2 \sinh^2(kh)}{\sinh(kh) \cosh(kh) + kh} \quad (38)$$

with H far field wave height
 S_0 stroke of wave paddle
 k wavenumber
 h water depth

The transfer between wave board displacements and water surface elevations is illustrated in Figure B.3. The spectrum of the surface elevation time series does contain energy at the sub harmonics, but contrary to the spectrum of wave board displacements, it is hardly visible. This is due to the Biésel transfer function, wave heights approach zero for very long waves (substitute $kh = 0$ in equation (38)).

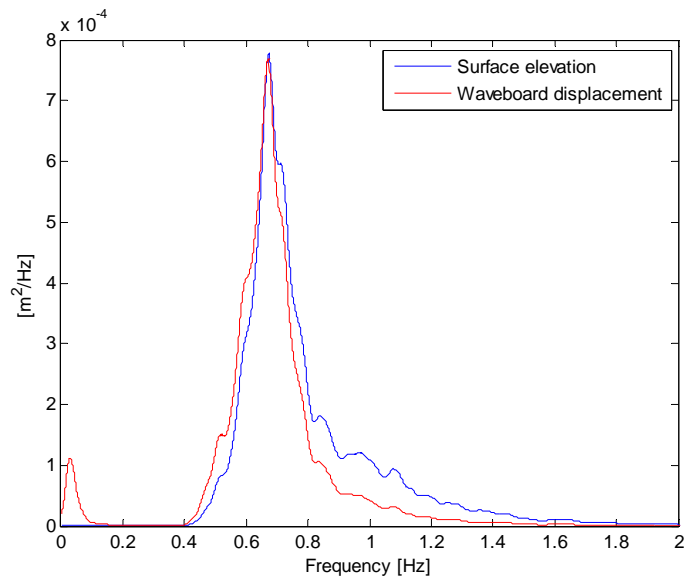


Figure B.3 – Biésel transfer for time series of test T076

The applied Biésel transfer function (38) is linear, so the transformation of wave board displacement to water surface elevation is of first order. The wave board displacements however already include second order effects. These second order effects are therefore also included in the computed water surface elevations.

Appendix C Determination of reflection coefficients

The reflection coefficients of the gravel slopes in the models are required for simulations with PHAROS and TRITON. In this section these coefficients will be determined with the following methods:

- Estimation based on scale model results
- Estimation based on empirical relations
- Calibration with PHAROS

It is assumed that the reflection coefficient of the gravel slopes is approximately the same for all tests, so just one value will be determined. The analysis focuses on the reflection coefficient of gravel slope 1 (located in the back of the main port basin).

C.1 Estimation based on scale model results

A rough estimation of the reflection coefficient of the gravel slope can be made based on the tests with perpendicular monochromatic waves in layout 1. The scale model is then essentially considered as a flume with a standing wave in it. The reflection coefficient can then be estimated by dividing the difference between the highest measured wave and the imposed wave by the imposed wave height. This yields results in the order of 0.3.

This approach is of course only valid if the highest measured wave height is equal to the actual maximum wave height in the domain, which is unlikely. Since 12 wave gauges have been installed in the main harbour basin of layout 1, it is however likely that one of them was placed reasonably close to an anti-node.

C.2 Estimation based on empirical relations

The dataset presented by Zanuttigh and Van der Meer (2006) (see section 2.1.4) can be used to estimate reflection coefficients from surf similarity parameters and structure properties. The surf similarity parameters of the tests considered here are in the range 1.0 – 2.2. From Figure 2.1 it follows that the reflection coefficients are then in the range 0.13 – 0.3, which is still a rather wide range.

C.3 Calibration with PHAROS

Three tests of monochromatic waves in layout 1 are simulated with PHAROS. This layout is chosen because it is the most simple and the wave patterns are therefore not so much influenced by processes such as diffraction. The reflection coefficient of the gravel slopes is varied in steps of 0.1. The differences between computed and measured wave heights are evaluated to find an optimal reflection coefficient.

The results of this procedure are presented in Table C.3. The mean absolute error and the root mean square error are based on calculated versus measured wave heights at all measurement locations. The RMS error is presented as a percentage of the incoming wave height.

Table C.3 - Calibration of reflection coefficients

Test	Type	Wave height [cm]	Wave period [s]	Wave angle [°]	Reflection coefficient	Mean abs error [%]	RMS error [%]
T001	Mono-chromatic	2.2	1.12	90	0.0	10	13
					0.1	9	12
					0.2	11	15
					0.3	16	21
					0.4	22	27
T003	Mono-chromatic	5.35	2.53	90	0.1	14	17
					0.2	12	17
					0.3	15	20
					0.4	21	26
T005	Mono-chromatic	3.08	1.49	110	0.1	9	12
					0.2	9	9
					0.3	13	14
					0.4	16	19

The results presented in Table C.3 show how the differences between the simulated and measured wave heights are more or less constant for reflection coefficients of 0.2 or less and rapidly increase for 0.3 and higher. For tests T003 and T005, a reflection coefficient of 0.2 appears to be optimal. For test T001 the smallest errors are found when a reflection coefficient of 0.1 is applied.

The height of the standing waves in the numerical model increases with increasing reflection coefficients. This means that if the nodes and anti-nodes are not precisely at the right location, the differences between the measured and modelled wave heights will on average also increase with increasing reflection coefficients. This effect should be taken into consideration when interpreting the results in Table C.3.

C.4 Conclusion

Three methods of determining the reflection coefficient of gravel slope 1 have been discussed. The first two are rather crude but give insight in the range of possible values. From the last analysis an optimal value of 0.2 is derived.

This value of 0.2 is considered applicable to all gravel slopes in the scale model (except for the breakwater). Gravel slopes 3 have a higher steepness than the gravel slope for which the analyses in this chapter are carried out. On the other hand, the gravel used for these slopes is a bit coarser. These differences are assumed to compensate each other.

The breakwater however is both steeper than gravel slope 1 and consists of stones with a finer gradation. Its reflection coefficient should thus be higher. A value of 0.3 is estimated for this structure.

Appendix D List of all wave conditions

Test	Layout	Type	H [m]	T [sec]	Depth [m]	Angle [°]	Directional spreading [°]	Duration [s]
T001	1	Mono-chromatic	0,018	1,12	0,44	90	0	524
T002	1	Mono-chromatic	0,027	1,49	0,44	90	0	598
T003	1	Mono-chromatic	0,050	2,53	0,44	90	0	807
T004	1	Mono-chromatic	0,018	1,12	0,44	110	0	524
T005	1	Mono-chromatic	0,027	1,49	0,44	110	0	598
T006	1	Bichromatic	0,027	1,23	0,44	90	0	792
			0,027	1,75	0,44	90	0	
T007	1	Bichromatic	0,027	1,35	0,44	90	0	840
			0,027	1,63	0,44	90	0	
T008	1	Bichromatic	0,022	1,60	0,44	105	0	938
			0,022	1,40	0,44	75	0	
T009	1	Bichromatic	0,022	1,60	0,44	95	0	938
			0,022	1,40	0,44	75	0	
T010	1	Mono-chromatic	0,056	0,75	0,44	90	0	449
T011	1	Mono-chromatic	0,056	1,34	0,44	90	0	568

Test	Layout	Type	H [m]	T [sec]	Depth [m]	Angle [°]	Directional spreading [°]	Duration [s]
T012	1	Mono-chromatic	0,056	2,24	0,44	90	0	747
T013	1	Mono-chromatic	0,035	0,67	0,44	90	0	434
T014	1	JONSWAP	0,027	1,49	0,44	90	0	1791
T015	1	Bichromatic	0,050	1,50	0,44	90	0	1240
			0,050	2,35	0,44	90	0	
T016	1	Bichromatic	0,050	1,50	0,44	90	0	1020
			0,050	1,80	0,44	90	0	
T021	2	Mono-chromatic	0,018	1,12	0,44	90	0	524
T022	2	Mono-chromatic	0,027	1,49	0,44	90	0	598
T023	2	Mono-chromatic	0,050	2,53	0,44	90	0	807
T025	2	Mono-chromatic	0,027	1,49	0,44	110	0	598
T026	2	Mono-chromatic	0,027	1,49	0,44	70	0	598
T027	2	Mono-chromatic	0,056	0,75	0,44	90	0	449
T028	2	Mono-chromatic	0,056	1,34	0,44	90	0	568
T030	2	Mono-chromatic	0,035	0,67	0,44	90	0	434

Test	Layout	Type	H [m]	T [sec]	Depth [m]	Angle [°]	Directional spreading [°]	Duration [s]
T031	2	Bichromatic	0.050	2.35	0.44	90	0	1240
			0.050	1.50		90		
T032	2	Bichromatic	0.050	1.80	0.44	90	0	1020
			0.050	1.50		90		
T035	2	JONSWAP	0.089	1.49	0.44	90	0	1791
T036	2	JONSWAP	0.133	1.49	0.44	90	0	1791
T038	2	JONSWAP	0,044	1,49	0,44	90	15	1791
T039	2	JONSWAP	0,044	1,49	0,44	70	0	1791
T040	2	JONSWAP	0,044	1,49	0,44	110	0	1791
T051	3	Mono-chromatic	0.018	1.12	0.44	90	0	524
T052	3	Mono-chromatic	0.027	1.49	0.44	90	0	598
T053	3	Mono-chromatic	0.050	2.53	0.44	90	0	807
T055	3	Mono-chromatic	0.027	1.49	0.44	110	0	598
T056	3	Mono-chromatic	0.027	1.49	0.44	70	0	598
T057	3	Mono-chromatic	0.056	0.75	0.44	90	0	449
T058	3	Mono-chromatic	0.111	1.34	0.44	90	0	568
T059	3	Mono-chromatic	0.133	2.24	0.44	90	0	747

Test	Layout	Type	H [m]	T [sec]	Depth [m]	Angle [°]	Directional spreading [°]	Duration [s]
T060	3	Mono-chromatic	0.035	0.67	0.44	90	0	434
T061	3	Bichromatic	0.050	2.35	0.44	90	0	1240
			0.050	1.50		90		
T062	3	Bichromatic	0.050	1.80	0.44	90	0	1020
			0.050	1.50		90		
T063	3	SEA+ SWELL	0.011	1.79	0.44	70	0	926
			0.044	1.04		110		
T064	3	SEA+ SWELL	0.011	1.79	0.44	70	0	1343
			0.089	1.04		110		
T068	3	JONSWAP	0.044	1.49	0.44	90	cos ² s s = 4	1791
T069	3	JONSWAP	0.044	1.49	0.44	70	0	1791
T070	3	JONSWAP	0.044	1.49	0.44	110	0	1791
T076	3	JONSWAP	0.044	1.49	0.44	90	0	1791
T078	3	JONSWAP	0.089	1.49	0.44	90	42	1791
T079	3	JONSWAP	0.089	1.49	0.44	90	0	1791
T080	3	JONSWAP	0.133	1.49	0.44	90	0	1791
T081	3	JONSWAP	0.178	1.49	0.44	90	0	1791
T083	3	Mono-chromatic	0.089	0.75	0.44	90	0	449
T084	3	JONSWAP	0.089	1.04	0.44	90	0	1343

Test	Layout	Type	H [m]	T [sec]	Depth [m]	Angle [°]	Directional spreading [°]	Duration [s]
T085	3	JONSWAP	0.089	2.24	0.44	90	0	2536
T086	3	SEA+ SWELL	0.033 0.089	2.24 1.04	0.44	70 110	0	1343

Appendix E Examples of TRITON input files

E.1 Input file

```
*****RUN INFO*****
T076* [runid]
*
* 2BB1          * [comment]
*
*****GRID PARAMETERS*****
empty.grd      * Gridfile
0              * [xpc] origin x
0              * [ypc] origin y
0              * [angle_grid] angle grid
39.97          * [ilenc] length in x-direction
29.96          * [jlenc] length in y-direction
571            * [imax] number of grid cells in x-direction
428            * [jmax] number of grid cells in y-direction
*
*
*****NUMERICAL PARAMETERS*****
0.035         * [dt] timestep
1791          * [TcompEnd] Final time computation
1791          * [TwaveEnd] Final time wave generation
200           * [itermax] Maximum number of iterations for BiCGSTAB
1.e-8         * [tolerance] Tolerance in convergence criterion BiCGSTAB
0             * [diss_lin] linear dissipation coefficient
0.5           * [diss_nl] nonlinear dissipation coefficient
*
*
*****DISPERSION RELATED PARAMETERS*****
0.3850        * [alpha] dispersion parameter
0.3600        * [beta] shoaling parameter
*
*
*****PHYSICAL PARAMETERS*****
0.0           * [level] uniform water level
1000.0        * Chezy coefficient for physical bottom friction
-999.0        * representative value for wave period (if <0,
              * then value from bnd file is taken)
.false.       * xdir implicit
.false.       * [breakyes] breaking included
20.0          * [phi_ini] initial breaking angle (in degrees) [default:
20]
10.0          * [phi_ter] terminal breaking angle (in degrees) [default:
10]
10.0          * [fp] scale parameters in breaker model [default:
10]
20.0          * [t_half] fraction of time scale parameter [default:
20]
*
*
*****MODEL INPUT FILES*****
2BB1.bnd      * boundary info file
triton_2BB1.bot* depth info file
*
*
*****RESTART OPTIONS*****
.false.       * WRITE DATA TO RESTART FILE
25.000        * TIMESTEP OF WRITING DATA TO RESTART FILE
```

```

1          * INDICATING STARTING NUMBER OF FIRST RESTART DATA FILE
.fal se.   * RETRI EVING DATA FROM RESTART FILE
restart001 * NAME OF FILE FROM WHICH RESTART DATA IS RETRI EVED
          * (WI THOUT EXTENSION)

```

E.2 Experts.mst file

```

0.001     * [rel_out]      relaxation parameter in determination of wave
celerity and propagation angle of outgoing wave
2d        * [sol type]    problem dimension (for solution procedure of
dispersion relation)
2         * [c_out]       parameter for regime wave boundary (1: long
wave assumption, 2: incoming wave, 3: dynamical)
0.1       * [delta]      coefficient for determination cBousmin and
thetamin limit cases
15        * [omegaTdamp]  constant in damping function
0.8       * [delta1]     constant in boundary condition of dispersion
relation
0.3       * [delta2]     constant in boundary condition of dispersion
relation
0.138    * [phasecorr]   constant for phasecorrection in dispersion
relation
.fal se.  * [periodic]   logical indicating whether all boundaries are
periodic
1         * [alpha_opt]  apply equation 322
.true.    * [eq322]      apply equation 322
.fal se.  * [eq323]      apply equation 323
.true.    * [tpnorm]     thetaplus for outgoing info, set to boundary
element normal (.true.) in wave direction (.fal se.)
.true.    * [extrapol]   extrapolation at lower right and upper left
corner
.true.    * [IDispersion] dispersion is present (.true.) or absent
(.fal se.)
1         * [sw_visc]    switch to include (1) or exclude (0) vorticity
part in viscosity term
3         * [bndtype]    Apply (1) Robins boundary condition for H~; (2)
Dirichlet; (3) or old condition from version 113
.true.    * [CorrectoincludesVelocity]
           *             If .true., then correction of the velocity at
the boundary is included
           *             If .fal se., then correction of the velocity at
the boundary is excluded
0         * [hoe]       higher order disabled

```

Appendix F Example of SWASH command file

```

$*****HEADING*****
$
PROJ 'T076' '1'
$
$*****MODEL INPUT*****
$
CGRID REG 0.015 0 0 39.97 30.94 571 442
$
VERT 2
$
INPGRID BOTTOM REG 0.015 0 0 571 442 0.07 0.07 $ EXC -99
READINP BOTTOM 1. '2BB1v4_bot_grid.bot' 1 0 FREE
$
INPGRID POROSITY REG 0.015 0 0 571 442 0.07 0.07
READINP POROSITY 1. '2BB1v4_por_grid.por' 1 0 FREE
$
INPGRID PSIZE REG 0.015 0 0 571 442 0.07 0.07
READINP PSIZE 1. '2BB1v4_psi_z_grid.psi_z' 1 0 FREE
$
INPGRID HSTRUCTURE REG 0.015 0 0 571 442 0.07 0.07
READINP HSTRUCTURE 1. '2BB1v4_hstr_grid.hstr' 1 0 FREE
$
INITIAL ZERO
$
BOUND SEGMENT XY 0.015 0 1 0 BTYPE VEL UNIFORM FOURIER 0 0 0 0
BOUND SEGMENT XY 1 0 39 0 BTYPE WEAK SMOO 1 SEC UNIFORM SERIES 'T046_S5-
96.tms'
BOUND SEGMENT XY 39 0 39.985 0 BTYPE VEL UNIFORM FOURIER 0 0 0 0
$
BOUND SIDE E CCW BTYPE VEL UNIFORM FOURIER 0 0 0 0
BOUND SIDE W CCW BTYPE VEL UNIFORM FOURIER 0 0 0 0
$
SPON N 0.84
$
$FRIC CONST 0
$
NONHYDROSTATIC
$
DISCRET UPW MOM
$
DISCRET UPW WMOM
$
TIMEI 0.2 0.5
$
$***** OUTPUT REQUESTS *****
$
POINTS 'punt1'          9.93500000          7.98900000
POINTS 'punt2'          29.90300000          8.03900000
POINTS 'punt3'          19.92000000          6.83500000
POINTS 'punt4'          19.89900000          6.15700000
POINTS 'punt5'          19.99300000          12.08000000
POINTS 'punt6'          18.03300000          16.53200000
POINTS 'punt7'          16.14300000          19.02900000
POINTS 'punt8'          16.14800000          22.68100000
POINTS 'punt9'          16.18200000          26.29100000
POINTS 'punt10'         19.91500000          4.52700000
POINTS 'punt11'         20.00000000          19.03000000
POINTS 'punt12'         20.00800000          26.29500000
POINTS 'punt13'         23.83000000          15.90000000

```

POI NTS	' punt14'	23. 83000000	19. 03000000
POI NTS	' punt15'	23. 80700000	22. 60100000
POI NTS	' punt16'	23. 82400000	26. 25200000
POI NTS	' punt17'	25. 04700000	21. 79400000
POI NTS	' punt18'	27. 25300000	24. 01200000
POI NTS	' punt19'	30. 64000000	27. 34000000
POI NTS	' punt20'	26. 54900000	20. 33400000
POI NTS	' punt21'	28. 79100000	22. 53900000
POI NTS	' punt22'	32. 18800000	25. 91900000
POI NTS	' punt23'	14. 89700000	7. 99400000
POI NTS	' punt24'	19. 88500000	8. 02100000
POI NTS	' punt25'	24. 91500000	8. 01000000
POI NTS	' punt26'	20. 00000000	15. 90000000
POI NTS	' punt27'	19. 99500000	22. 67800000

\$

FRAME ' frame1' 0.015 0 0 39.97 30.94 571 442

FRAME ' frame2' 0.015 0 0 39.97 30.94 57 44

\$

QUANTITY XP ' Xp' ' Xp' 0 50

QUANTITY YP ' Yp' ' Yp' 0 50

QUANTITY WATLEV ' WATLEV' ' WATLEV' -0.9 0.9 0.999

QUANTITY HS ' HS' ' HS' 0 0.9 0.999 0 25 MIN

\$

TABLE ' punt1' HEAD ' T076_p1. tbl ' TSEC XP YP WATL VKSI VETA OUTPUT
000000.000 0.05 SEC

TABLE ' punt2' HEAD ' T076_p2. tbl ' TSEC XP YP WATL VKSI VETA OUTPUT
000000.000 0.05 SEC

TABLE ' punt3' HEAD ' T076_p3. tbl ' TSEC XP YP WATL VKSI VETA OUTPUT
000000.000 0.05 SEC

TABLE ' punt4' HEAD ' T076_p4. tbl ' TSEC XP YP WATL VKSI VETA OUTPUT
000000.000 0.05 SEC

TABLE ' punt5' HEAD ' T076_p5. tbl ' TSEC XP YP WATL VKSI VETA OUTPUT
000000.000 0.05 SEC

TABLE ' punt6' HEAD ' T076_p6. tbl ' TSEC XP YP WATL VKSI VETA OUTPUT
000000.000 0.05 SEC

TABLE ' punt7' HEAD ' T076_p7. tbl ' TSEC XP YP WATL VKSI VETA OUTPUT
000000.000 0.05 SEC

TABLE ' punt8' HEAD ' T076_p8. tbl ' TSEC XP YP WATL VKSI VETA OUTPUT
000000.000 0.05 SEC

TABLE ' punt9' HEAD ' T076_p9. tbl ' TSEC XP YP WATL VKSI VETA OUTPUT
000000.000 0.05 SEC

TABLE ' punt10' HEAD ' T076_p10. tbl ' TSEC XP YP WATL VKSI VETA OUTPUT
000000.000 0.05 SEC

TABLE ' punt11' HEAD ' T076_p11. tbl ' TSEC XP YP WATL VKSI VETA OUTPUT
000000.000 0.05 SEC

TABLE ' punt12' HEAD ' T076_p12. tbl ' TSEC XP YP WATL VKSI VETA OUTPUT
000000.000 0.05 SEC

TABLE ' punt13' HEAD ' T076_p13. tbl ' TSEC XP YP WATL VKSI VETA OUTPUT
000000.000 0.05 SEC

TABLE ' punt14' HEAD ' T076_p14. tbl ' TSEC XP YP WATL VKSI VETA OUTPUT
000000.000 0.05 SEC

TABLE ' punt15' HEAD ' T076_p15. tbl ' TSEC XP YP WATL VKSI VETA OUTPUT
000000.000 0.05 SEC

TABLE ' punt16' HEAD ' T076_p16. tbl ' TSEC XP YP WATL VKSI VETA OUTPUT
000000.000 0.05 SEC

TABLE ' punt17' HEAD ' T076_p17. tbl ' TSEC XP YP WATL VKSI VETA OUTPUT
000000.000 0.05 SEC

TABLE ' punt18' HEAD ' T076_p18. tbl ' TSEC XP YP WATL VKSI VETA OUTPUT
000000.000 0.05 SEC

```

TABLE 'punt19' HEAD 'T076_p19.tbl' TSEC XP YP WATL VKSI VETA OUTPUT
000000.000 0.05 SEC
TABLE 'punt20' HEAD 'T076_p20.tbl' TSEC XP YP WATL VKSI VETA OUTPUT
000000.000 0.05 SEC
TABLE 'punt21' HEAD 'T076_p21.tbl' TSEC XP YP WATL VKSI VETA OUTPUT
000000.000 0.05 SEC
TABLE 'punt22' HEAD 'T076_p22.tbl' TSEC XP YP WATL VKSI VETA OUTPUT
000000.000 0.05 SEC
TABLE 'punt23' HEAD 'T076_p23.tbl' TSEC XP YP WATL VKSI VETA OUTPUT
000000.000 0.05 SEC
TABLE 'punt24' HEAD 'T076_p24.tbl' TSEC XP YP WATL VKSI VETA OUTPUT
000000.000 0.05 SEC
TABLE 'punt25' HEAD 'T076_p25.tbl' TSEC XP YP WATL VKSI VETA OUTPUT
000000.000 0.05 SEC
TABLE 'punt26' HEAD 'T076_p26.tbl' TSEC XP YP WATL VKSI VETA OUTPUT
000000.000 0.05 SEC
TABLE 'punt27' HEAD 'T076_p27.tbl' TSEC XP YP WATL VKSI VETA OUTPUT
000000.000 0.05 SEC
$
TABLE 'frame1' HEAD 'T076_hs.fr' TSEC XP YP HS
TABLE 'frame1' HEAD 'T076_wl.fr' TSEC XP YP WATL VKSI VETA OUTPUT
002943.000 0.05 SEC
TABLE 'frame2' HEAD 'T076_lf.fr' TSEC XP YP WATL VKSI VETA OUTPUT
000000.000 0.5 SEC
$
COMPUTE 000000.000 0.01 SEC 002951.000
STOP

```